THESIS FOR THE DEGREE OF DOCTOR OF PHILOSOPHY

# Chip-based magnetic levitation of superconducting microparticles

Martí Gutiérrez Latorre


Department of Microtechnology and Nanoscience (MC2)
Chalmers University of Technology
Gothenburg, Sweden, 2023

**Chip-based magnetic levitation of superconducting microparticles**

Martí Gutiérrez Latorre
ISBN 978-91-7905-787-9



Technical Report No. 5253
ISSN 0346-718X
Department of Microtechnology and Nanoscience (MC2)

Under the supervision of:
Witlef Wieczorek, Docent [1]
Thilo Bauch, Docent [2]

Examined by:
Avgust Yurgens, Professor [2]

[1] Quantum Technology division, Department of Microtechnology and Nanoscience
[2] Quantum Devices division, Department of Microtechnology and Nanoscience

Chalmers University of Technology
SE-412 96 Gothenburg, Sweden
Phone: +46 (0)31 772 1000
www.chalmers.se

Printed by Chalmers Reproservice
Gothenburg, Sweden, January 2023

*To my friends and family, without whom I would not even have tried.*
*Als meus amics i família, sense els quals ni ho hagués intentat.*

# Abstract

Magnetically levitated superconductors are extremely isolated from the environment, their mechanical properties can be tuned magnetically, and can be coupled to quantum systems such as superconducting quantum circuits. As such, they are a promising experimental platform for the creation of massive spatial quantum states that would test quantum mechanics in a hitherto unexplored parameter regime. Furthermore, they could be used to build ultrasensitive detectors of accelerations and forces, which could find applications in seismology, navigation, geodesy, or dark matter detection.

This thesis is about the development and demonstration of a chip-based magnetic levitation platform for µm-sized superconducting particles. To this end, we have modeled, designed, and fabricated micrometer-scale superconducting particles as well as chip-based magnetic traps based on planar superconducting coils. We have detected the center-of-mass motion of the levitated particles magnetically, with integrated superconducting coils that transport the signal of the particle motion to a SQUID magnetometer. We demonstrated stable levitation of 50 µm diameter particles over several days at millikelvin temperatures. This high stability allowed us to thoroughly characterize the particle motion and show that our model of the magnetic trap and the detection scheme captures the nonlinear behavior of the center-of-mass motion. These nonlinearities are observed due to large motional amplitudes caused by the coupling between the particle motion and cryostat vibrations. We have devised a cryogenic vibration isolation system based on an elastic pendulum that mitigates this effect and has enabled ring-down measurements of the center-of-mass motion that give quality factors up to $10^5$. Furthermore, we have shown that the mechanical properties of the levitated particle can be controlled. We have tuned the trap frequencies from 30 Hz to 180 Hz by changing the current in the trap coils, and we have also demonstrated control over the motional amplitude of the particle motion via feedback using feedback coils in the chip to exert an additional magnetic force on the particle.

This thesis demonstrates magnetic levitation of superconducting microparticles on a chip as a novel platform for chip-based quantum experiments with µm-sized particles and ultrasensitive force and acceleration sensors.

**Keywords:** Magnetic levitation, superconductors, SQUID, optomechanics.

# List of Publications

This thesis is based on the following publications:

[A] **Martí Gutierrez Latorre**, Joachim Hofer, Matthias Rudolph, Witlef Wieczorek, "Chip-based superconducting traps for levitation of micrometer-sized particles in the Meissner state". Superconduting Science and Technology, **3**, 105002-105017 (2020).

[B] **Martí Gutierrez Latorre**, Achintya Paradkar, David Hambraeus, Gerard Higgins, Witlef Wieczorek, "A Chip-Based Superconducting Magnetic Trap for Levitating Superconducting Microparticles". IEEE Transactions on Applied Superconductivity, **32**, 4, 1800305 (2022).

[C] **Martí Gutierrez Latorre**, Gerard Higgins, Achintya Paradkar, Thilo Bauch, Witlef Wieczorek, "Superconducting microsphere magnetically levitated in an anharmonic potential". arXiv:2210.13451 (2022).

Other publications by the author, not included in this thesis, are:

[D] David Niepce, Jonathan J. Burnett, **Martí Gutierrez Latorre**, Jonas Bylander, "Geometric scaling of two-level-system loss in superconducting resonators". Supercond. Sci. Technol. **33**, 025013 (2020).

# Acknowledgments

First and foremost, I am extremely grateful to my supervisor, Witlef Wieczorek, for the great deal of time and effort you have invested. Your supervision has been stern and fair, and for that I am incomparably better now than I was when I started. When I applied for this PhD project, I absolutely felt like I was overreaching, and I can't thank you enough for deciding I was the right person for the job, whatever the reason.

I am too extremely grateful to David Niepce, who took me and other newly minted PhD students and had us follow him around to show us the ropes. I don't know if I would have gotten half as far as I got without your help. I am also very thankful to my co-supervisor, Thilo Bauch, and my examiner, Avgust Yurgens, and Alexei Kalaboukhov for always being available and willing to answer my calls for help and entertaining my not-so-standard ideas. I would also like to thank Matthias Rudolph and Gerard Higgins for teaching me how things are really done in a lab and for some great times in and outside the lab too.

Special thanks go to Lars Jönsson for invaluable help with his almost supernatural technician skills, and being a such a great person through and through. Special thanks also to Linda Bråvell, for going above and beyond helping people, I do not know what our department would do without you two. I am also very grateful to Susannah Carlsson, Maria Tremblay, Debora Perlheden and Annika Holtringer for helping and teaching me about administration.

I am very grateful to Henrik Fjelldstedt and Ulf Andersson for their excellent IT and technical support. It really showed in your work that you care.

Big thanks go to the Nanofabrication Lab at MC2. Thank you, Johan Andersson, Ulf Södervall, Mattias Fredriksson, Mats Hagberg, Henrik Frederiksen, Niclas Lindval, Marcus Rommel, Mahdad Sadeghi, Petra Johansson, Karin Hedsten, Ruggero Verre and Grigory Skoblin for entertaining my sometimes unreasonable ideas and dealing with my untimely working schedule in the cleanroom.

I would also like to thank the whole of the MagLev group, Achintya Parad-

kar, Fabian Resare, Lukas Deeg (if only for your short visit) and our master students Anton Söderqvist, and Avan Mirkhan for an amazing working environment. It has been great fun working with all of you. The project is in good hands.

I would also like to thank the rest of my group, Sushanth Kini, Hanlin Fang and Anastasiia Ciers. It has been a pleasure being your colleague and friend, having great scientific and mundane discussions alike. The same goes for all of my colleagues and friends in and out of my department, as well as everyone in the Austrian side of the Maglev project now too numerous to list in such a small space. Sorry for not writing all your names, but I have to fit a thesis here too.

Last but not least, I must thank my friends and family. Your support hasn't faltered, even when I have. Thank you for being my lifeline despite having almost completely disappeared from your lives for five years.

# Acronyms

| | |
|---|---|
| TCT: | Two-Chip Trap |
| COM: | Centre-of-Mass |
| SQUID: | Superconducting Quantum Interference Device |
| FLL: | Flux-locked Loop |
| JJ: | Josephson Junction |
| FPGA: | Field-Programmable Gate Array |

# Contents

# CHAPTER 1

# Introduction

Currently, we rely on two physical theories to describe how nature functions. On one side, quantum physics describes the behavior of the very small, and on the other side, general relativity describes the behavior of the very large. However, it is known that neither of these theories is compatible with the other.

We do not experience any quantum phenomena in our daily lives, and yet small objects such as atoms clearly do. This begs the question; where is the transition between the classical and the quantum, and why is there one?

Quantum mechanics was developed at the beginning of the 20th century because certain physical phenomena, such as blackbody radiation and light absorption and emission, didn't obey classical physics. Initially, only photons and subatomic particles were thought to behave quantum mechanically. This was supported by the fact that they were able to interfere with themselves

[1]–[3], which implied that they had to be described as waves with a wave function. Later on, in 1988, atoms [4], [5] were found to display the same behavior, and after that, molecules of increasingly large sizes with up to $10^4$ atomic mass units [6]–[8].

Indeed, there is nothing within the framework of quantum mechanics that sets a limit on how large or massive an object can be before it can no longer be considered a quantum object [9]. The key seems to be in the coherence of the quantum state of the object.

Put simply and briefly, the coherence of a quantum state is the capability of a quantum state to display interference. The quantum state describing an object perfectly isolated from the environment has an infinite coherence time, meaning that it remains quantum indefinitely. If the object is interacting with either a measurement apparatus or the environment, the quantum state describing it will lose its coherence and gain coherence with what it interacts with over time. Because we have no way of tracking the coherence of the quantum state describing the object with the environment or the measurement apparatus, this coherence is lost, and the quantum state decoheres.

Decoherence is the reason why large objects do not display quantum effects due to their large number of interactions with other objects, which causes them to decohere faster than they can be measured, which means that if sufficiently isolated, large objects should display quantum behavior.

Quantum states have also been hypothesized to decohere due to mechanisms beyond standard quantum mechanics. One among the many proposed mechanisms is known as continuous spontaneous localization (CSL). The CSL model hypothesizes that quantum states decohere due to intrinsic noise, introduced as a stochastic, nonlinear term in the Schrödinger equation that grows with the mass and the size of the quantum state [10]. Another proposed decoherence mechanism is related to gravity [11]. Since space-time is determined by the mass distribution in space, a massive object in a quantum superposition would generate a superposition of space-times. A superposition of space-times implies two different time coordinates, which is problematic in quantum mechanics because Schrödinger's equation requires a unique time dimension.

Gravitational interaction with quantum systems has been measured in experiments with neutrons and atom clouds [12]–[14]. This technology has been refined to the point that quantum gravimeters are commercially available [15]. However, the gravitational effect of neutrons and atom clouds on other masses is negligible, due to their minuscule masses.

More massive objects have been shown to display quantum behavior in experiments with crystal bulk resonators coupled to superconducting qubits at cryogenic temperatures. At millikelvin temperatures, the thermal energy of the environment is lower than the zero point energy of breathing modes of the bulk resonator. Thus, this mechanical mode can be considered to be in the quantum ground state [16], [17]. In these experiments, qubits were used to create quantum states of the mechanical modes of the bulk resonators with masses of $10^{19}$ atomic mass units [18]. However, the spatial extents of the quantum states of the mechanical modes are of the order of attometers, so the quantum state itself is not large at all [19]. Furthermore, the mechanical modes of bulk resonators have no center-of-mass motion; there is no way to make the spatial extent of the quantum state larger.

It must be said that truly macroscopic quantum states have been created with Cooper pair ensembles in a superconducting quantum interference device (SQUID) [20], diffraction of single neutrons [21], atom interferometry [14], [22], [23] and atom cloud experiments [24], [25] which have achieved quantum states that extended from 650 µm to 53 cm, lasting up to several seconds. These experiments have demonstrated the validity of quantum mechanics for the length and time scales we can experience in our daily lives. This begs the question: would quantum mechanics remain valid for similar systems if they had large masses?

The challenge is to find massive systems with which quantum states can be generated such that the quantum states can have sizes larger than the object used to create the quantum state. At the same time, they should have long enough coherence times so that quantum effects may be measured. Levitated microparticles are a well-suited experimental platform for such experiments. In particular, optical levitation of nanoparticles is currently the most mature levitation technology [26]–[29]. Focused lasers, commonly called optical tweezers, can levitate particles between tens of nanometers up to tens

of micrometers [30].

A 100 nm nanoparticle has a mass of approximately $10^9$ atomic mass units, so it is relatively massive compared to objects that display quantum properties by default. Recent experiments have shown that the center-of-mass (COM) modes of optically levitated silica nanoparticles can be brought to the ground state [28], [29], [31]–[33], which opens the possibility of quantum state generation with the COM modes. The size of a COM quantum state can be delocalized (enlarged) by tuning the potential landscape of the mode as much as decoherence allows [34], [35]. Because the COM modes of levitated particles in vacuum are extremely well isolated from the environment, with quality factors up to $10^8$ at sufficiently high vacuum [36], quantum states generated with COM modes have the potential for long coherence times.

The fundamental limitations in optically levitated systems when used as a platform for quantum experiments are that the mass (or size) of levitated objects is limited by light absorption of the object [30]. In addition to this, the shot noise of the laser used to levitate the particle, that is, the random fluctuations of the laser intensity cause random momentum fluctuations in the COM motion known as photon recoil [27]. This mechanism sets the bound to the achievable coherence times in any eventual quantum experiment.

Both of these limitations can be overcome using magnetic levitation instead. Magnetic levitation can be used to levitate objects of different shapes [37], [38] with masses ranging from picograms to tons [39], [40] and no light is required. It, too, offers extreme isolation from the environment (mechanical quality factors up to $10^7$ have been demonstrated) [34], [41]–[45] and allows for tunable potential landscapes using coils. Furthermore, they can be magnetically coupled to superconducting quantum circuits, which would allow for the creation of spatial quantum superposition states, large spatial delocalization of the position of the object or squeezed quantum states of motion [35], [46]–[48].

For these reasons, magnetic levitation as an experimental platform has been gaining interest in the field of levitodynamics [49]. Recent experimental developments in magnetically levitated systems include levitating micro-magnets on top of superconductors [42], [50]–[53], diamagnetic particles in strong mag-

netic fields [40], [43], [44], [54], [55], and superconducting microparticles in millimeter-scale superconducting magnetic traps [45], [56], [57]. Such levitated objects would be extremely sensitive to external forces or accelerations, with sensitivities of the order of $1 \times 10^{-23}\,\mathrm{N\,Hz^{-0.5}}$ and $1 \times 10^{-14}\,\mathrm{g\,Hz^{-0.5}}$ for measuring forces and accelerations, respectively [52], [58], compared to state-of-the-art with $1.2 \times 10^{-20}\,\mathrm{N\,Hz^{-0.5}}$ and $1 \times 10^{-12}\,\mathrm{g\,Hz^{-0.5}}$ [59]–[64]. This force sensitivity would allow one to measure the gravitational pull between two Vespa scooters separated by the average distance between the earth and the moon if one were to measure for a few seconds. Such sensors can find applications in geodesy, navigation, and dark matter detection [65]. Because such systems are extremely sensitive to external stimuli such as magnetic noise and mechanical vibrations, they will require extreme magnetic shielding and vibration isolation.

Magnetic levitation of superconductors with superconducting coils is the levitation scheme that promises the least intrinsic mechanical dissipation [34], [41]. Levitated superconductors in the Meissner state, unlike levitated magnets, do not suffer from intrinsic eddy current damping or intrinsic magnetic noise due to fluctuations in the magnetization drift, known as magnetic moment drift [42], [51]–[53], [66], and the magnetic trap can be made perfectly stable by using persistent currents even at milliKelvin temperatures [67], which is not possible in experiments using magnets to levitate diamagnetic particles due to magnetic moment drift [43], [53], [54], [68].

By using on-chip superconducting coils we can miniaturize the magnetic trap and focus the magnetic field in a very small volume [57], [69], [70] which enables high magnetic field gradients of the order of $100\,\mathrm{T\,m^{-1}}$ and trapping frequencies up to kHz [37]. Chip-based traps also have the potential to scale up to tens or hundreds of levitated particles within an area of a few square centimeters to either levitate multiple particles in as many independent traps or to multiplex one trap to levitate multiple particles within it.

Furthermore, the COM motion of the levitated superconductor can be measured by coupling inductively to superconducting loops that transport the magnetic flux signal generated by the particle motion to a SQUID magnetometer [56], [57], [71] or a flux-tunable SQUID resonator [72]–[76]. The COM motion can then be cooled using techniques such as feedback cooling [28], [29],

[32], [33], [71] and cavity cooling [31], [72]–[76]. If the particle displacement can be detected with a precision capable of resolving zero point fluctuations of the COM modes, the mechanical modes could be cooled to the ground state, just like in optical levitation experiments.

Coupling the COM modes of the levitated object to another quantum system, such as a superconducting flux qubit, would enable experiments to produce non-classical states of motion such as spatial superposition states or, matter-wave interferometry experiments [34], [41], [46]. This would open the possibility to perform experiments to test the principles of quantum mechanics in the interface between the quantum and the classical world, to measure gravitational interactions between microscopic objects, or even entangle the motion of two microscopic objects via gravity [77], [78].

This thesis describes the work done during the five years of this Ph.D. degree on experiments with magnetically levitated superconducting microparticles with chip-based magnetic traps. The work in this thesis focuses on the design, modeling, and fabrication of chip-based magnetic traps and superconducting microparticles, as well as the demonstration of magnetic levitation of superconducting microparticles using chip-based magnetic traps based on superconducting coils. Further, we used SQUID magnetometry to measure the COM motion of the levitated microparticles and demonstrated first steps towards controlling the motional amplitude using feedback in the form of magnetic forces exerted by integrated superconducting coils on the chip-traps.

## 1.1 Contribution to the field

To design chip-based magnetic traps of sizes similar to the size of the particle they are levitating, it is essential to use a model that accounts for the effects of complex geometries of the superconducting coils, such as narrow turns and openings, and for the demagnetization effects caused by the geometry of the particle. Only then will we be able to accurately describe the potential landscape of the particle in the magnetic trap. For this purpose, we implemented the Maxwell-London equations in the finite element method (FEM) software COMSOL Multiphysics, to simulate superconducting objects in the Meissner

state with extended volumes and arbitrary shapes. Our implementation also accounts for flux quantization within the superconducting objects, which allows us to model the effect that the trapped magnetic flux would have on a levitated particle. We used this model to design and characterize magnetic traps based on integrated superconducting coils that could stably levitate superconducting microparticles, with trap frequencies up to 10 kHz. The model has also been used to analyze the effect of the shape and size of the levitated particles on the trap properties, as well as the effect of flux quantization within the particles. These results have been published in Paper A [37].

Because this model computes the full electromagnetic field and the supercurrent distribution in the superconductors, it has also been used to accurately compute the filling factor of the electric field in superconducting co-planar waveguide (CPW) resonators ranging from nanometers to tenths of micrometers in size, which typical electrostatic simulations fail to describe [79].

We developed microfabrication processes to produce chip-based magnetic traps made of very thick niobium layers (1 µm) with critical current densities of $3 \times 10^{10}\,\mathrm{A\,m^{-2}}$, as well as free-standing flat micro-rings and disks made of niobium with the same thickness, and near-spherical particles made of lead.

We have demonstrated stable levitation of 50 µm diameter lead and tin-lead spheres in a chip-based trap at temperatures of 4 K and 50 mK with COM frequencies of 30-180 Hz, which are on par with other experiments with diamagnetically levitated particles [45], [51], [54], [68]. We used optical imaging to observe the center-of-mass (COM) motion of the particle within the cryostat. Using a tracking algorithm, we have shown that the mechanical dynamics of the levitated particle are well described by our model. These results allowed us to demonstrate chip-based levitation as a feasible route toward magnetic levitation of superconducting microparticles. These results have been published in Paper B [80].

After managing to reliably levitate microparticles on the chip traps, we worked on measuring and characterizing the COM motion of the levitated particles via magnetic means, which eliminates the need for optical access to the levitated particle. The COM motion of the particle was inductively coupled to superconducting coils inside the trap, which transport the signal

of the particle motion to a SQUID magnetometer. With no optical access to the sample, the particle levitates for several days and is expected to remain levitated indefinitely. We have shown that our model for the system is in good agreement with measured trap frequencies and their dependence on trap current and particle material (mass density). Moreover, we have shown that our model of the system properly describes the measured anharmonicity of the magnetic trap as well as the observed nonlinearities in the detection of the particle motion. We have shown these trap anharmonicities by measuring the nonlinear behavior of the COM motion, as well as mode coupling between the COM modes of the levitated particle. Nonlinear effects in the particle motion arise from the anharmonicity of the trap, as well as large motional amplitudes of the order of µm caused by mechanical vibrations in the cryostat driving the particle motion.

These measurements show that magnetically levitated superconducting microparticles levitated on a chip can stably levitate for very long times, that their motion can be measured via SQUID magnetometry without compromising the stability of the system, that the trap frequency can be tuned by simply changing the trap current, and that our model accurately describes the anharmonic nature of the magnetic chip traps which manifests at large motional amplitudes. All of these results have been published in Paper C [57].

We have shown that the effect of mechanical vibrations on the particle motion can be reduced using cryogenic vibration isolation of the experimental setup by hanging it from an elastic pendulum, which decouples the particle motion from the cryostat vibrations. Ringdown measurements show mechanical quality factors of up to $10^5$. This value is lower than quality factors reported in similar experiments ($10^7$) [45] and well below the largest possible value ($10^9$) [34], [41]. This discrepancy shows that the quality factor in our experiments can still improve by at least two orders of magnitude with further optimization of the experimental setup.

Furthermore, we have shown proof of principle of feedback control of the COM motion using a SQUID magnetometer, a Field-Programmable Gate Array (FPGA), and additional superconducting coils on the chip to exert a magnetic feedback force that has been used to both heat and cool the particle motion. The cooling was very limited compared to that achieved in similar

experiments due to the large magnetic noise and mechanical vibrations. However, technical improvements regarding the reduction of measurement noise and vibration isolation should allow for amplitude reductions of several orders of magnitude and, in principle, allow for cooling to the ground state of motion [43]–[45], [54], [55], [68].

## 1.2 Thesis structure

In Chapter 2, we introduce the theoretical background for the key concepts that are relevant to the experiments. These concepts include superconductivity and superconducting levitation, SQUID magnetometry, surface interactions, and the basics of linear and nonlinear mechanical resonators.

In Chapter 3 we explain how our magnetic traps have been modeled and fabricated. We describe the experimental setup and the physics behind instrumentation, such as cryostats, and components, such as magnetic shields and SQUID-based detection of levitated superconducting particles. We also explain the measurement techniques used in the experiments.

In Chapter 4 we give an overview of the results of the levitation experiments, the COM motion detection via optical detection, and then via DC-SQUID magnetometry. We describe the observed nonlinear behavior of the COM motion due to magnetic trap anharmonicities and nonlinear detection. We show preliminary results demonstrating the decoupling of the levitated particle from cryostat vibrations using cryogenic vibration isolation. We provide estimates for the damping caused by various dissipation mechanisms, and we study the prospects of bringing the motion of the levitated particle to the ground state using feedback cooling.

In Chapter 5 we summarize the results and give an outlook for the near future of the project.

Chapter 6 contains the appendix, with a detailed description of the fabrication recipes, as well as untested chip traps with multiple trap sites, and levitation experiments with superconducting microparticles and magnet traps,

that were successful but not pursued in this thesis due to lack of time and so did not fit in Chapter 4, but I think deserve mentioning.

Finally, Chapter 7 contains a brief summary of Papers A, B, and C, followed by the full papers appended after the summary.

# CHAPTER 2

# Theoretical background

In this chapter, we give an overview of different models of superconductivity that explain key concepts essential to this thesis and show how these concepts are relevant to the magnetic levitation of superconductors. Then we explain how flux-sensitive superconducting devices function and how they are used as magnetometers, which we used to measure the motion of magnetically levitated superconducting particles. Finally, we will introduce mechanical resonators, and their behavior in the linear, nonlinear, and coupled regime, which is required to understand the complex dynamics of levitated particles in our magnetic trap.

## 2.1 Superconductivity

In the following, we introduce the models of superconductivity required to understand the physics at play in the experiments of this thesis. Namely, the two-fluid model, the London model, and the Ginzburg-Landau model.

Superconductivity is the physical property displayed by materials that have no resistance to electrical current and expel the magnetic field from within their volume. The disappearance of electrical resistance was discovered by Heike Kamerlingh Onnes in 1911 when measuring the resistance of mercury at 4.2 K. After that, the disappearance of electrical resistance was observed in several other materials, such as niobium and lead [81]. It was not until 1931 that Meissner and Ochsenfeld discovered that superconducting materials expel magnetic fields from within their volume, and in 1935 Rjabinin and Shubnikov found that some superconductors have the capability of trapping magnetic flux within the superconducting volume, thus discovering type II superconductors [82], [83].

### Two-fluid model of superconductivity

The two-fluid model describes the electrical properties of a superconductor, assuming that a superconducting material has two different types of charge carriers. The first type of charge carriers are normal carriers that lose energy due to scattering with the ion lattice of the material, and the second type of charge carriers are super-carriers that do not. At temperatures larger than $T_c$ all charge carriers in the superconductor are normal carriers and the charge carrier density equals the normal carrier density $n = n_n$ $(T > T_c)$. However, at temperatures below $T_c$ the normal carriers start to become supercarriers, and the charge carrier density becomes the sum of the normal and the supercarrier densities $n = n_n + n_s$. The density of supercarriers $n_s$ at a temperature below $T_c$ is given by [84]

$$n_s = n\left(1 - \left(\frac{T}{T_c}\right)^4\right), \tag{2.1}$$

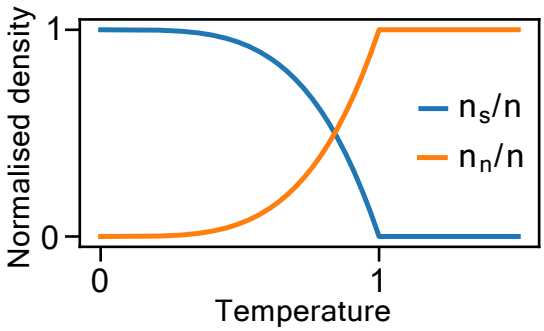


**Figure 2.1:** Two-fluid model: Temperature dependence of the supercarrier density $n_s$ and normal carrier density $n_n$.

and the distribution of $n_s$ and $n_n$ above and below $T_c$ is shown in Fig. 2.1.

According to Drude's model, the electrical conductivity of a normal conductor can be obtained from the equations of motion of the charge carriers [85], [86]. For an electron in a conductor, the equation of motion is

$$m_e \frac{d\vec{v}(t)}{dt} = -e\vec{E}(t) + m_e \frac{1}{\tau}\vec{v}(t), \tag{2.2}$$

where $e$ and $m_e$ are the electron charge and mass, respectively, and $\tau$ is the scattering time, which is the average time between collisions between an electron and the ion lattice. Assuming that we have an oscillating electric field $\vec{E} = \vec{E}_0 e^{-i\omega t}$, we can re-write Eq. (2.2) as

$$-i\omega m_e \vec{v} = -e\vec{E} + m_e \frac{1}{\tau}\vec{v}, \tag{2.3}$$

from which we obtain the velocity

$$\vec{v} = \frac{e\tau}{m_e}\frac{1}{1+i\omega\tau}\vec{E}. \tag{2.4}$$

Since the electrical current in a conducting material is defined as

$$\vec{J} = ne\vec{v} = \sigma\vec{E}, \tag{2.5}$$

we can use Eq. (2.4) to obtain the normal state conductivity $\sigma_n$ of a material by substitution

$$\vec{J} = \frac{ne^2\tau}{m_e}\frac{1}{1+i\omega\tau}\vec{E}(t) = \frac{ne^2\tau}{m_e}\vec{E}(t)\left(\frac{1}{1+(\omega\tau)^2} - i\frac{\omega\tau}{1+(\omega\tau)^2}\right), \tag{2.6}$$

and so the normal state conductivity is

$$\sigma_n = \frac{n_n e^2\tau}{m_e(1+\omega^2\tau^2)} - i\frac{n_n e^2\omega\tau^2}{m_e(1+\omega^2\tau^2)}. \tag{2.7}$$

Repeating the calculation for the supercarriers, with $\tau \to \infty$ we obtain a velocity

$$\vec{v}_s = \frac{e}{i\omega m_e}\vec{E} \tag{2.8}$$

and superconducting state conductivity

$$\sigma_s = -i\frac{n_s e^2}{m_e\omega}. \tag{2.9}$$

From this simple approach, it is already possible to see that (i) a superconductor will have no resistance to direct currents ($\sigma_s(\omega = 0) = \infty$), (ii) it will have a finite conductivity for alternating currents that will become larger at higher frequencies, and that (iii) for larger temperatures $\sigma_n$ and $\sigma_s$ will increase and decrease, respectively, due to the decreasing $n_s$ and increasing $n_n$ (see Eq. (2.1)).

In this work, we have used either direct current, or very low-frequency currents in the order of hundreds of Hz, and the experiments are performed at temperatures well below $T_c$. Therefore, no frequency or temperature-dependent superconducting phenomena will be discussed.

## Maxwell-London equations

The Maxwell-London equations are a phenomenological set of equations proposed by the London brothers that, in addition to Maxwell's equations, describe the supercurrent density $\vec{J_s}$ and the electric $\vec{E}$ and magnetic field distributions $\vec{B}$ inside a type I superconductor [87]. These equations are

$$\frac{\partial \vec{J_s}}{\partial t} = \frac{n_s e^2}{m_e}\vec{E} \tag{2.10}$$

$$\nabla \times \vec{J_s} = -\frac{n_s e^2}{m_e}\vec{B} \tag{2.11}$$

The first equation states that there are no electric fields inside the superconductor unless the supercurrent is changing over time, i.e., no electric fields in the steady state. The second equation states that the supercurrent in the superconductor generates a magnetic field equal to and opposite to the magnetic field applied to the superconductor. Applying Ampere's law ($\nabla \times \vec{B} = \mu_0 \vec{J}$) to equation 2.11 we obtain an equation for the magnetic field inside the superconductor

$$\nabla^2 \vec{B} = \frac{\mu_0 n_s e^2}{m_e}\vec{B} = \frac{1}{\lambda_{\mathrm{L}}^2}\vec{B}, \tag{2.12}$$

where $\nabla$ is the vector Laplacian operator, $\mu_0$ is the magnetic permeability of vacuum and $\lambda_{\mathrm{L}}$ is the London penetration depth, with

$$\lambda_{\mathrm{L}} = \sqrt{\frac{m_e}{\mu_0 n_s e^2}}. \tag{2.13}$$

This equation describes an exponential decay of the magnetic field within the superconductor, with a decay constant $\lambda_{\mathrm{L}}$. Effectively, the magnetic field is expelled from within the volume of the superconductor, which is said to be in the Meissner state. Note that because $\lambda_{\mathrm{L}}$ depends on $1/n_s \propto \frac{1}{1-T/T_c}$ the field will penetrate further inside the superconductor the closer the temperature

gets to $T_c$. For temperatures equal to and larger than $T_c$, there is no field expulsion.

## Ginzburg-Landau equations

The Ginzburg-Landau equations model a superconductor using a wave function that describes the order parameter in the superconductor [88]. This wave function is related to the supercarrier density ($\Psi = \sqrt{n_s}e^{i\theta}$).

The equations are [88]

$$\alpha\Psi + \beta\left|\Psi\right|^2\Psi + \frac{1}{2m_e}\left(-\hbar\nabla - 2e\vec{A}\right)^2\Psi = 0, \tag{2.14}$$

$$\vec{\nabla}\times\vec{B} = \mu_0\vec{J}_s \tag{2.15}$$

$$\vec{J}_s = -\frac{2e^2}{m_e}\vec{A}\Psi^*\Psi - i\frac{e\hbar}{2m_e}\left(\Psi^*\vec{\nabla}\Psi - \Psi\vec{\nabla}\Psi^*\right),$$

where $\hbar$ is the reduced Planck constant, and $\alpha$ and $\beta$ are material-dependent parameters related to the supercarrier density as $-\alpha/\beta = \left|\Psi\right|^2$.

The solutions to these equations are a scalar and a vector field for $\Psi$ and $\vec{A}$, respectively. These fields have a characteristic length. For $\vec{A}$ the characteristic length is the magnetic field penetration depth $\lambda_{\mathrm{GL}}$, the analog of $\lambda_{\mathrm{L}}$ in the London equations, which is defined as

$$\lambda_{\mathrm{GL}} = \sqrt{\frac{m_e\beta}{2\mu_0 e^2|\alpha|}}. \tag{2.16}$$

For $\Psi$ the characteristic length is the coherence length

$$\xi_{\mathrm{GL}} = \sqrt{\frac{\hbar^2}{2m_e|\alpha|}}, \tag{2.17}$$

i.e. the length within which $\Psi$ can no longer be considered homogeneous.

The ratio between these two length scales $\kappa = \lambda_{GL}/\xi_{\mathrm{GL}}$ is the Ginzburg-Landau parameter, which determines whether the material will manifest type I or type II superconductivity.

## Type I and Type II superconductivity

The values of $\lambda_{GL}$ and $\xi_{\mathrm{GL}}$ determine the surface energy of the interface between normal conducting and superconducting regions in a superconductor. This surface energy is positive for $\kappa < 1/\sqrt{2}$ and negative for $\kappa > 1/\sqrt{2}$, which suggests two different types of superconductors.

For type I superconductors, with $\kappa < 1/\sqrt{2}$, the interfaces between normal conducting and superconducting regions of the material are energetically unfavorable. To minimize the interfaces, the magnetic field from within the whole volume of a type I superconductor will be expelled if the temperature and the magnetic field are below the critical values $T_c$ and $B_c$. A superconductor with no normal conducting regions within its volume is said to be in the Meissner state, which is illustrated in Fig. 2.2(a) and (b).

For type II superconductors, with $\kappa > 1/\sqrt{2}$, the interfaces between normal conducting and superconducting regions of the material are energetically favorable above a certain magnetic field, known as the first critical field $\vec{B}_{\mathrm{c1}}$. Thus, the volume within a type II superconductor will be in the Meissner state, until the external magnetic field reaches $\vec{B}_{\mathrm{c1}}$. Above $\vec{B}_{\mathrm{c1}}$, the magnetic field starts to cross the volume of the superconductor through cylindrical columns of normal conducting material, through which a single magnetic flux quantum ($\phi_0 = h/2e$) flows. These are known as flux vortices or Abrikosov vortices, and they are a result of flux quantization, which will be discussed in the following section. As the field increases, more flux vortices form in the superconductor. Eventually, a value of the magnetic field is reached for which the flux vortices leave no room for any superconducting volume (see Fig. 2.2(c)). This magnetic field is known as the second critical field ($B_{\mathrm{c2}}$), above which the material becomes normal conducting.

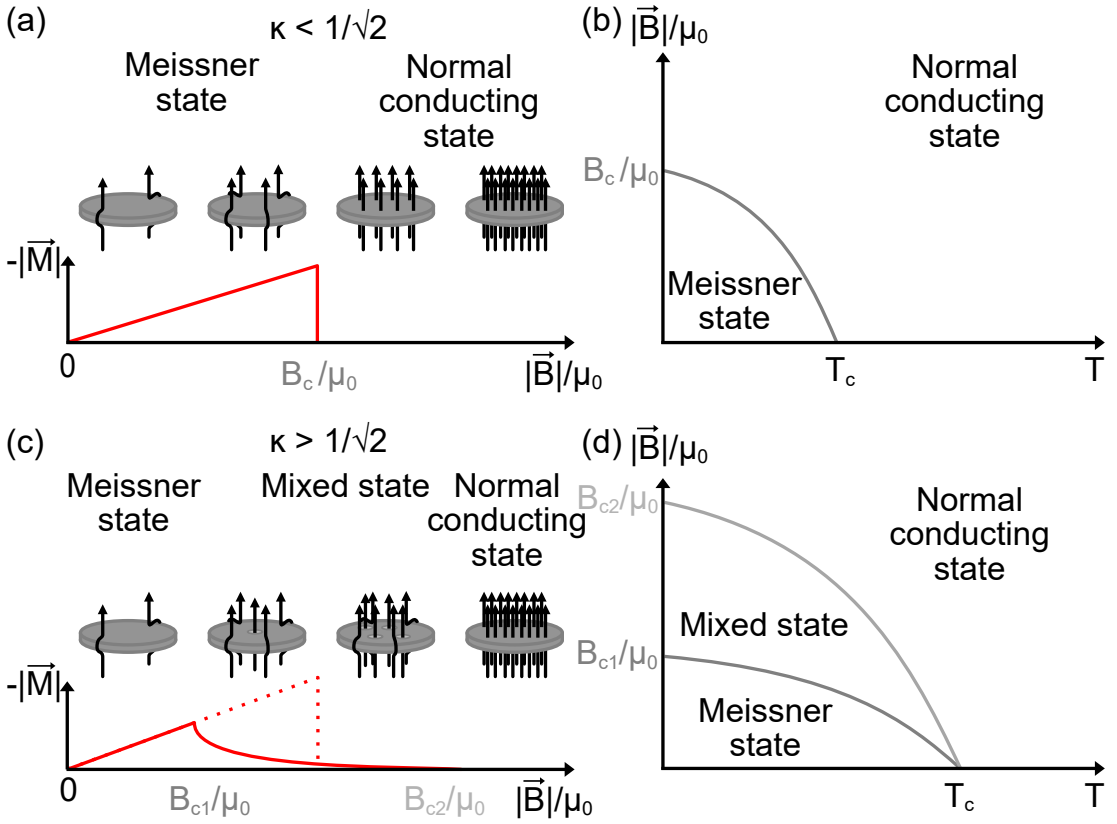


**Figure 2.2:** Type I and Type II superconductivity. (a)-(c) Magnetization curves and (b)-(d) phase diagrams of type I and type II superconductors, illustrating field expulsion, field penetration by flux vortices, and the temperature dependence of $B_c$, $B_{c1}$, and $B_{c2}$, respectively.

Note that all superconducting properties ultimately depend on the superconducting charge carrier concentration $n_s$. Due to the temperature dependence of $n_s$, the values for the critical fields will decrease for increasing temperatures and become zero at $T = T_c$, as shown in Fig. 2.2(b) and (d).

## Magnetic flux quantization

A direct consequence of the expression for the supercurrent density used in Eq. (2.15), is that within a superconducting loop, the magnetic flux threading the area within the loop is quantized.

In order to illustrate this, let us imagine a piece of superconducting material with a hole in a magnetic field $\vec{B}_a$. Assuming that $\Psi = \sqrt{n_s}e^{i\theta}$, the expression for the supercurrent in Eq. (2.15) becomes

$$\vec{J_s} = \frac{en_s\hbar}{2m_e}\left(\vec{\nabla}\theta - 2\frac{e}{\hbar}\vec{A}\right). \tag{2.18}$$

Well inside the superconductor, $\vec{J_s}$ is zero, which implies $\vec{\nabla}\theta = \frac{2e}{\hbar}\vec{A}$. Integrating both sides of the equation around the hole, we obtain

$$\frac{2e}{\hbar}\oint_l \vec{A}\cdot d\vec{l} = \oint \vec{\nabla}\theta \cdot d\vec{l}, \tag{2.19}$$

where $d\vec{l}$ is the differential length of the perimeter of the area over which we integrate.

Using the Stokes theorem ($\int_l \vec{F}\cdot d\vec{l} = \iint_S \nabla\times\vec{F}\cdot d\vec{S}$) and that $\nabla\times\vec{A} = \vec{B}$ we can rewrite Eq. (2.19) in terms of the magnetic field threading the surface of the hole in the superconductor

$$\frac{2e}{\hbar}\iint_S \vec{B}\cdot d\vec{S} = \oint \vec{\nabla}\theta\cdot d\vec{l}. \tag{2.20}$$

Because $\Psi$ is a continuous periodic function, the result of the integration is

$$\begin{aligned}\frac{2e}{\hbar}\phi &= 2\pi n \\ \phi &= 2\pi N\frac{\hbar}{2e} = N\phi_0,\end{aligned} \tag{2.21}$$

where $N$ is an integer number, which restricts the values of the magnetic flux through the hole to integer multiples of the magnetic flux quantum $\phi_0 = h/2e$.

### Fluxoid quantization

Fluxoid quantization is the same phenomenon as flux quantization, with one difference. Namely, that when integrating Eq. (2.18) the integral of the supercurrent cannot be neglected, either because the magnet field penetration is large or because the superconducting ring is very narrow.

The condition for the quantized flux threading the hole in the superconductor becomes

$$N\phi_0 = \phi + \Lambda \oint \vec{J_s} \cdot d\vec{l}, \tag{2.22}$$

where $\Lambda = \frac{m_e}{n_s e^2} = \mu_0 \lambda_{\mathrm{L}}^2$.

## 2.2 Superconducting levitation

Magnetic levitation of superconducting objects can be achieved in two fundamentally different ways. The physical mechanisms are described in the following sections. However, regardless of the mechanism employed to exert a trapping force on the object, the conditions for stable trapping are always the same. First, there must be a potential energy ($U$) minimum, i.e. balance of forces, in which the levitated object can rest. And second, at the levitation point, the potential energy must have positive curvature so that the levitation is stable, and the particle is confined to the levitation point. These conditions can be expressed as

$$\nabla U = 0, \tag{2.23}$$

$$\nabla^2 U > 0. \tag{2.24}$$

Earnshaw's theorem states that square law forces (such as electromag-

netism) cannot be used to hold objects in a stationary, stable equilibrium in a three-dimensional space [89]. However, this theorem does not apply to diamagnetic objects in a magnetic field because they only experience repulsive forces, unlike charges in an electric field, or paramagnets and ferromagnets in a magnetic field.

We will proceed to explain how these conditions can be fulfilled using Meissner state repulsion and magnetic flux pinning, respectively.

## Meissner-state repulsion

Meissner-state repulsion is a consequence of the null electric resistance in superconductors. When a magnetic field is applied to a superconductor, a supercurrent is induced that cancels out the applied magnetic field within the object, making the total magnetic field within its volume close to zero. This supercurrent has an energy cost, which means, that the most energetically favorable magnetic field strength for a superconductor is zero. Assuming a point-like superconducting particle, the energy is given by the potential energy of a diamagnet in a magnetic field and a gravitational field

$$U = -\frac{\chi}{1 + D\chi} \frac{B^2 V}{2\mu_0} + mgz, \tag{2.25}$$

where $\chi$ is the magnetic susceptibility of the superconductor, $B$ is the magnetic field strength, $V$ is the volume of the superconductor and $mgz$ is the gravitational potential, with $m$ being the mass, $g$ the gravitational field intensity and $z$ the height of the object. The factor $D$ is the demagnetizing factor of the superconductor [90]. This accounts for the effective reduction of the magnetic field around the superconductor, which can be seen as the back-action of the superconductor on the surrounding field due to the expulsion of the field from within the volume. In the following calculation, $D = 0$ because we assume the superconductor to be point-like, and thus, has no volume.

By applying the stability criterion to the potential energy, one obtains

$$\nabla^2 U = -\frac{\chi V}{2\mu_0}\nabla^2 B^2, \tag{2.26}$$

which is strictly positive for a diamagnetic material, due to $\chi < 0$. Therefore, diamagnetic objects, and especially superconductors ($\chi = -1$), can be stably levitated in the minimum of a magnetic field distribution. Note that stability of diamagnetically levitated objects requires either (i) the engineering of a three-dimensional magnetic field minimum with a sufficiently strong gradient to overcome gravity [Fig. 2.3(a)] or (ii) a two-dimensional magnetic field minimum within which the third dimension (vertical) is stabilized via a magnetic force that equals that of gravity. The second kind of trap is known as magneto-gravitational [54], [68], [91].

## Flux pinning

A property unique to type II superconductors is the ability to trap magnetic flux within the superconducting volume, see Section 2.1. This property can be used to provide stability to levitated type II superconductors.

To best illustrate this phenomenon, it is simplest to use the opposite case, of a magnet levitated on a superconductor. If a magnet that generates a nonuniform magnetic field $B$ with no translational symmetry ($\frac{d|B|}{dr}|_{r=x,y,z} \neq 0$), such as a dipole, is placed on top of a type II superconductor while undergoing the transition into superconductivity, an image of the magnetic moment of the magnet is frozen in the superconductor. At the same time, the superconductor will repel the magnet due to Meissner-state repulsion, and the magnet will be pushed upward, as most of the volume of a type II superconductor is in the Meissner state. If the superconductor were of type I, the magnet would be held up via Meissner state repulsion, but the system would be unstable in the directions parallel to the plane. However, due to the frozen flux in the superconductor, an attractive force toward the frozen image (see Fig. 2.3(b)) will act on the particle (as long as there is no translational symmetry), providing lateral and vertical confinement. In this way, the magnet is fully trapped by the type II superconductor alone.

Similarly, placing a superconducting object on a magnetized surface (again,

with no translational symmetry) leads to the superconductor stably levitating over the surface. The mechanism for this is much the same, as, during the superconducting transition, the superconductor will trap the magnetic flux flowing across it, freezing an image of the magnet inside it. At the same time, the Meissner-state repulsion will push it upward away from the magnet and the superconductor will be stably levitated above the magnet due to flux pinning.

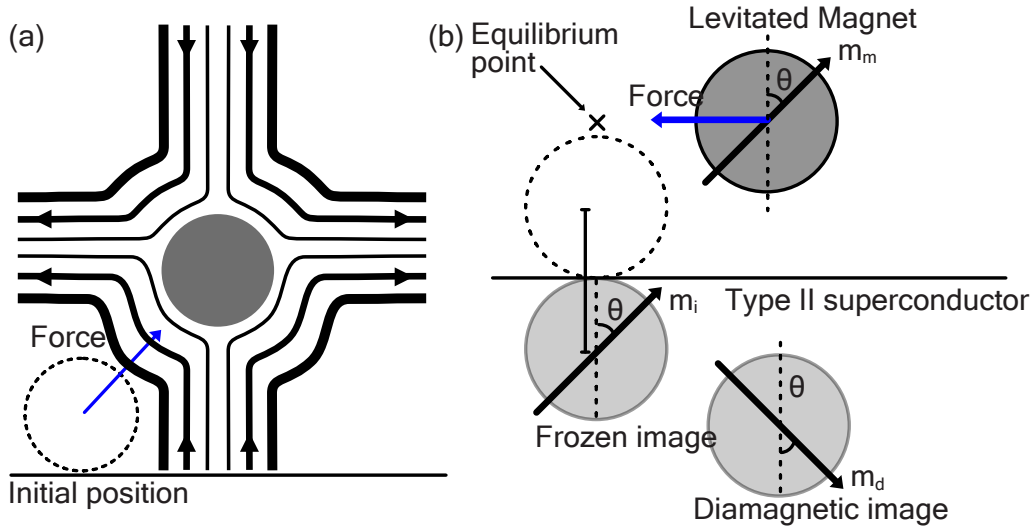


**Figure 2.3:** (a) A superconductor levitated with a quadrupole magnetic field using Meissner state repulsion. The superconductor is repelled by the high field regions (thicker lines) and is pushed into the center of the quadrupole field, where the magnetic field is minimum. Note that the particle is displaced downward from the quadrupole center due to the force of gravity. (b) Schematic of a magnet levitated on a type II superconductor. The superconductor produces two images of the levitated magnet. The frozen image is a consequence of flux trapping and the diamagnetic image is a consequence of Meissner state repulsion. The dashed line shows the initial resting position of the magnet.

## 2.3 Superconducting Quantum Interference Device (SQUID)

In this thesis, the SQUID plays a key role as a detector for the motion of the levitated particles. In the following, we will introduce the working principle of the SQUID, starting with its structural parts, i.e. Josephson Junctions (JJs), and the fundamental phenomenon they rely on, the Josephson effect. Then we describe the SQUID itself, and finally how it is used as a magnetometer.

### Josephson junctions

Josephson Junctions (JJs) are weak links in superconducting materials that weaken superconductivity at the linking region. A superconducting weak link can be achieved in several ways, such as having a nanometer-thin layer of oxide or metal between two superconductors or making a nanometer-thin constriction in a superconductor (Dayem bridge). The current and voltage across these weak links are described by the Josephson equations [92], which are commonly known as the DC and AC Josephson effects, respectively. The equations are

$$I = I_c \sin(\delta) \tag{2.27}$$

and

$$V = \frac{\hbar}{2e}\frac{d\delta}{dt} = \frac{\phi_0}{2\pi}\frac{d\delta}{dt}, \tag{2.28}$$

where $\phi_0$ is the magnetic flux quantum and $\delta = \theta_1 - \theta_2$ is the difference between the phase of the wave function of the superconductors at each side of the junction (see Fig. 2.4).

The DC Josephson effect states that if there is a phase difference across the junction, Cooper pairs will tunnel through it, causing a DC current to appear, which can take values between $+I_c$ and $-I_c$.

The AC Josephson effect states that the application of a voltage on the junction will cause the phase difference ($\delta$) to change linearly over time. Due to

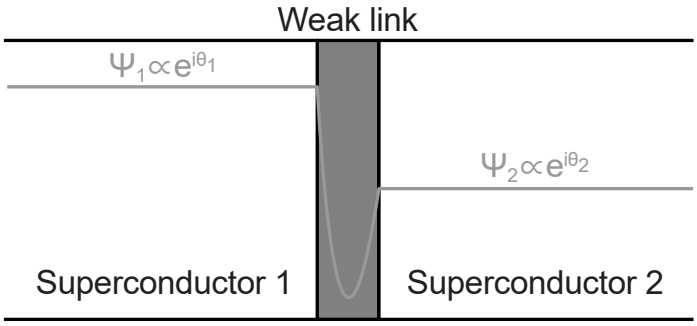


**Figure 2.4:** Schematic representation of a Josephson junction and the order parameter $\Psi$ across it.

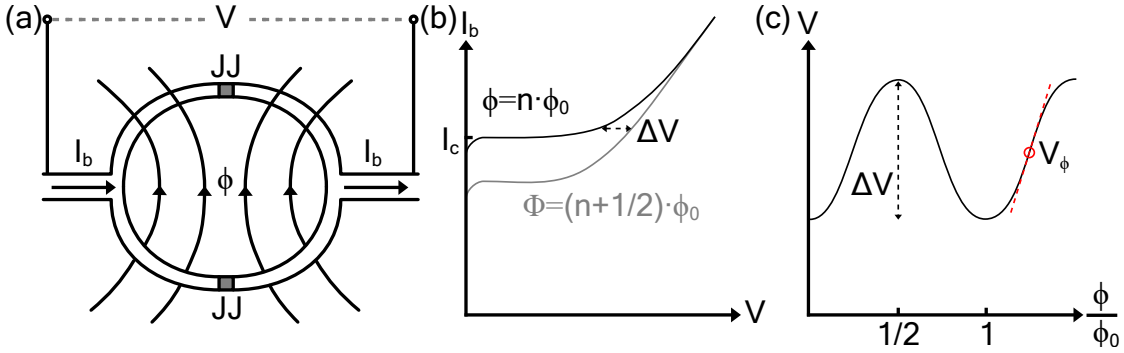


**Figure 2.5:** (a) Schematic representation of a DC-SQUID. (b) I-V curve of a DC-SQUID for one and half a magnetic flux quantum threading the loop. (c) V-$\phi$ curve of a DC-SQUID with a current bias above the critical current of the SQUID.

Eq. (2.27) an alternating current with amplitude $I_c$ will appear. The frequency of this DC current is given by the applied voltage $f = \frac{1}{2\pi}\frac{d\delta}{dt} = \frac{1}{\phi_0}V$.

## DC-SQUID

A SQUID is a type of Josephson device based on a superconducting loop interrupted by JJs. A superconducting loop with one JJ is known as an RF-SQUID and a loop with two JJs is known as a DC-SQUID, which we will focus on.

When a bias current $I_b$ runs through the SQUID, it is split into two currents,

one for each arm of the loop. In the absence of external flux, and in the case of identical junctions, the current in each arm is the same. If the external flux increases, a current is induced in the loop that increases the current in one arm and decreases it in the other. When the current in one of the arms overcomes the critical current of the junction at the arm, a voltage across the SQUID loop appears. This voltage is a function of both $I_b$ and the magnetic flux in the SQUID loop, as shown in Fig. 2.5(b).

If the DC-SQUID is biased with a current slightly above the critical current of the SQUID, the voltage across the SQUID will oscillate as a function of the magnetic flux in the SQUID loop with a period of $\phi_0$, as shown in Fig. 2.5(c).

This means that for magnetic flux changes of the order of $\phi_0/2$, the DC-SQUID can be used as a very sensitive magnetic flux to voltage converter, if operated at the point with the maximum slope in Fig. 2.5(c), called the operation point. The slope at the operation point has the maximum sensitivity to magnetic flux, called the transfer function ($V_\phi$). However, for magnetic flux changes larger than $\phi_0/2$, the voltage response of the DC-SQUID to flux can no longer be considered linear, as it becomes periodic and, thus, multi-valued.

The shortcomings of low dynamic range and nonlinear response can be overcome by operating the DC-SQUID in tandem with other electronics, which together make a DC-SQUID magnetometer.

## DC-SQUID magnetometer

Linearizing the voltage output of a DC-SQUID provides a very large dynamic range while keeping its sensitivity, which makes it an excellent magnetometer. To linearize the voltage output the SQUID is operated with Flux-Locked Loop (FLL) electronics, shown in Fig. 2.6. The SQUID is biased with a current and a voltage that will place it in its working point, and then the voltage of the SQUID is connected to a negative feedback loop, which will flux-bias the SQUID to preserve the voltage across it.

Whenever an external flux ($\phi_e$), changes the flux through the SQUID, the voltage across it changes too. This change in voltage is recorded by an inte-

grator and fed back as a flux ($\phi_\mathrm{f}$) through a current and a feedback coil that cancels out the external flux ($\phi_\mathrm{e} = -\phi_\mathrm{f}$), bringing the SQUID back to the working point.

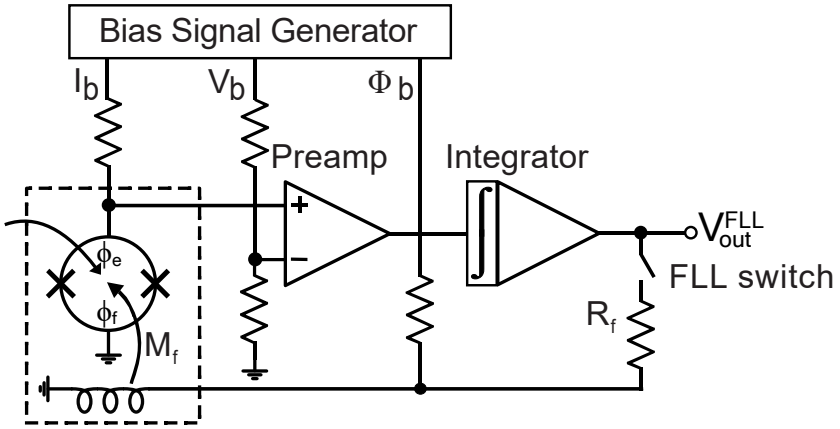


**Figure 2.6:** Circuit equivalent of the DC-SQUID control electronics, including the flux-locked loop (FLL) electronics. The elements inside the dashed line are cooled to cryogenic temperatures. Figure adapted from [93].

Thus, the output of the integrator ($V_\mathrm{out}^\mathrm{FLL}$) is proportional to $\phi_\mathrm{e}$, and is given by

$$V_\mathrm{out}^\mathrm{FLL} = \frac{R_\mathrm{f}}{M_\mathrm{f}}\phi_\mathrm{e}, \tag{2.29}$$

where $R_\mathrm{f}$ is the resistance of the feedback line and $M_\mathrm{f}$ is the mutual inductance between the feedback inductor and the SQUID (see the elements after the FLL switch in Fig. 2.6).

## 2.4 Surface interactions

An important matter to consider when working with micrometer-sized objects is the surface interaction between that object and the surface it stands on. As it turns out, the attractive force between a microscopic object and a flat surface is, in general, orders of magnitude stronger than the gravitational force it will experience. This adhesion force can be estimated for the case of a sphere standing on a flat surface, as [94]

$$F_{\mathrm{VdW}}^{\mathrm{sphere}} = -A_H \frac{R}{6d^2}, \tag{2.30}$$

and for any shape with a flat bottom surface (such as a cylinder) and a flat surface below, as [95]

$$F_{\mathrm{VdW}}^{\mathrm{flat}} = -A_{\mathrm{H}} \frac{S_c}{6\pi d^3}, \tag{2.31}$$

where $R$ is the radius of the sphere, $d$ is the distance between the flat object and the plane, $S_c$ is the surface of contact between the surface and the flat object, and $A_{\mathrm{H}}$ is the Hamaker constant, which describes the strength of the interaction between the materials of the object and the plane it stands on and has units of energy. The $A_{\mathrm{H}}$ values for the materials used as substrates in our work are shown in Table 2.1 [95].

| Material | $A_{\mathrm{H}}$ $(1 \times 10^{-20}\,\mathrm{J})$ |
|---|---|
| Silicon | 18.6 |
| Silicon oxide | 6.5 |

**Table 2.1:** Hamaker constants for the materials used as the flat substrates on which the particles lie.

Because the actual distance between a microparticle and a surface is hard to determine due to the objects and the surfaces having roughness, it is difficult to get good estimates of the adhesion force even if the Hamaker constant for the appropriate materials and the radius of the particle is known. Despite this, atomic force measurements have shown that the adhesion forces for particles with sizes of micrometers lie around 100 nN [95], [96]. These forces are much larger than the weight of particles of such sizes, which range from 0.1 pN to 10 pN.

To levitate microparticles, the adhesion force must be overcome either by the magnetic force generated by the trap or by some other means, like shaking the substrate the particle sits on with a piezoelectric actuator.

## 2.5 Levitated mechanical resonators

This section explains the physics describing the motion of a levitated superconducting particle in a magnetic chip trap. We start by describing how the frequencies of the COM motion of the levitated particles are calculated. Then, we describe the oscillatory motion and the effects of anharmonicity and mode coupling, which are necessary to understand the motion of the levitated particle within the magnetic chip trap.

### Calculation of trap frequencies

The COM motion of a rigid body can oscillate in different ways depending on its shape. A sphere is the simplest rigid body in terms of COM motion because it only has three oscillation modes, which are the translational oscillations in $x$, $y$, and $z$. However, objects with lower symmetry, such as discs and rings, have translational as well as librational oscillations. Librations are bound rotations, meaning that the object rotates back and forth instead of rotating freely.

The translational and librational frequencies of a levitated particle are obtained by calculating the force $F_i$ and the torque $\tau_i$ acting on the particle within the magnetic trap as a function of position and tilt, respectively, and are given by [97]

$$\omega_{\text{translation}} = \frac{1}{\sqrt{m}}\sqrt{-\frac{\delta F_i}{\delta r_i}}, \tag{2.32}$$

and

$$\omega_{\text{libration}} = \frac{1}{\sqrt{I}}\sqrt{-\frac{\delta \tau_i}{\delta \theta_i}}, \tag{2.33}$$

where $I$ is the momentum of inertia of the particle in the axis of rotation of the angle $\theta_i$.

The forces and torques can be obtained either analytically or numerically. When calculated analytically, one obtains formulas for the force and the torque, but when using numerical methods one obtains another variable with which to calculate them. In our case, these variables are the electric and magnetic fields. The electromagnetic forces and torques acting on an object subject to an electromagnetic field can be obtained with the Maxwell stress tensor $T$, whose components $T_{ij}$ are given by

$$\begin{aligned} T_{ij} = \epsilon_0 \left( E_i E_j - \frac{1}{2}\delta_{ij}|\vec{E}|^2 \right) \\ + \frac{1}{\mu_0} \left( B_i B_j - \frac{1}{2}\delta_{ij}|\vec{B}|^2 \right), \end{aligned} \tag{2.34}$$

where $\epsilon_0$ and $\mu_0$ are the electrical permittivity and magnetic permeability, respectively, $E_i$ and $B_i$ are the vector components of the electric and the magnetic field, and $\delta_{ij}$ is the Kronecker delta. The electromagnetic forces and torques can be calculated via surface integrals as [98]

$$\vec{F} = \oint_{\Omega} \vec{n} T dS, \tag{2.35}$$

and

$$\vec{\tau} = \oint_{\Omega} (\vec{r} - \vec{r}_0) \times (\vec{n} T) dS, \tag{2.36}$$

where $\vec{\tau}$ is the torque, $\vec{n}$ is the unit vector normal to the particle surface, $\Omega$ is the surface of the particle, and $\vec{r}$ and $\vec{r}_0$ are the application point of the torque and the center of mass of the particle, respectively.

## Harmonic oscillations

A harmonic oscillator is any physical system with a degree of freedom $x$ that has a restoring constant $k$ that minimizes its potential energy at an equilibrium point, and whose potential energy is given by $U = kx^2/2$. For a mechanical oscillation, i.e. an object moving back and forth, that does not interact with

the environment (i.e. the mechanical energy remains constant), the dynamics of the position of the object can be described by

$$m\ddot{x} + m\omega^2 x = 0, \tag{2.37}$$

where $m$ is the mass of the oscillating object, and $\omega$ is the angular frequency of the oscillation, which is related to the restoring constant $k$ by $\omega = \sqrt{k/m}$. The solution to such an equation is a simple sinusoidal function $x(t) = x_0 \sin(\omega t + \theta)$, where $\theta$ is a phase and $x_0$ is the amplitude.

The loss of energy to the environment due to viscous drag can be accounted for by adding a damping term to Eq. (2.37)

$$m\ddot{x} + m\gamma\dot{x} + m\omega^2 x = 0, \tag{2.38}$$

where $\gamma$ is the rate of energy loss from the oscillator to the environment, which we will refer to as damping. The ratio between the frequency of the oscillator $\omega$ and the damping $\gamma$ is the quality factor of the oscillator ($Q = \omega/\gamma$). Unless specified otherwise, we will work under the assumption that $\gamma \ll \omega$ (i.e. the underdamped regime), where the displacement of the oscillator can be written as

$$x(t) = A_0 e^{-2\gamma t} \sin(\omega t + \theta), \tag{2.39}$$

where $A_0$ is the amplitude of motion at $t = 0$ [99].

## Anharmonicity

An anharmonic oscillator is an oscillator whose expression for the potential energy has terms with orders larger than $x^2$, such as

$$U = \tfrac{1}{2} m\omega_0^2 x^2 + m\alpha x^3 + m\beta x^4. \tag{2.40}$$

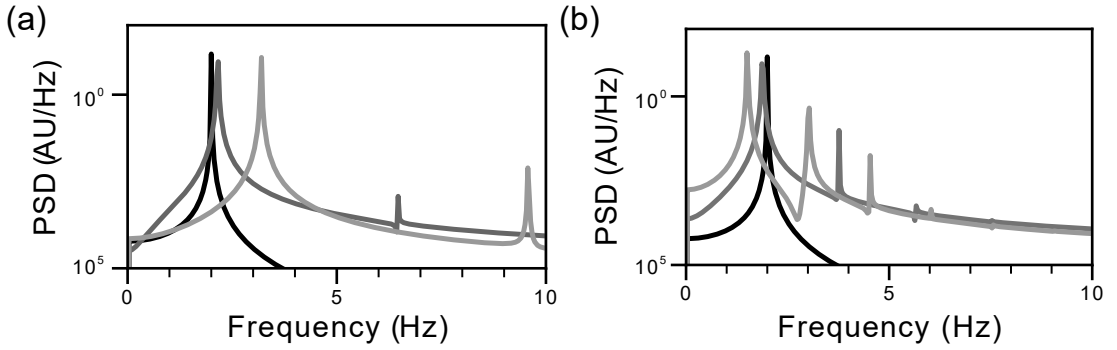


**Figure 2.7:** Power spectra of the displacement of a 2 Hz oscillator with (a) a quartic (Duffing) and (b) a cubic nonlinearity. Lighter lines indicate larger $\alpha$ and $\beta$. Note that the fundamental frequency is shifted due to frequency pulling (Eq. (2.44)).

Only even terms in the potential can generate restoring forces because only terms that depend on the displacement to an even power increase the energy of the system for both positive and negative displacements. Instead, cubic terms ($\alpha$), and odd terms in general, have the effect of shifting the equilibrium point and making the restoring force at the two sides of the equilibrium point different. The quartic terms ($\beta$) are known as Duffing or Kerr nonlinearities that either increase or decrease the restoring force depending on the sign of $\beta$.

Higher-order terms have two effects on the dynamics of the system. The first effect is that they cause the appearance of higher-order harmonics in the dynamics, as shown in Fig. 2.7. Cubic terms cause the $2\omega$ and all other harmonics of $\omega$ to appear, with decreasing amplitudes for higher harmonics. The quartic (Duffing) terms cause the $3\omega$ and all other odd multiples of $\omega$ to appear, also with decreasing amplitudes for higher harmonics.

This can be understood trigonometrically. In the equations of motion, the cubic and Duffing terms depend on $x^2$ and $x^3$, respectively. Since $x$ is a cosine function with amplitude $x_0$, the higher-order terms generate the following frequency components

$$\begin{aligned} x^2(t) &= x_0^2(\cos\omega t)^2 = \frac{x_0^2}{2}(\cos 2\omega t + 1) \\ x^3(t) &= x_0^3(\cos\omega t)^3 = \frac{x_0^3}{4}(\cos 3\omega t + 3\cos\omega t), \end{aligned} \tag{2.41}$$

whose amplitude decreases for higher orders, given that the energy in the harmonic is larger than the energy in the higher harmonics $\omega^2 x_0^2 \gg \alpha x_0^3, \beta x_0^4$.

The second effect is that they shift the frequency of the oscillator $\omega$ up or down, depending on the sign of $\alpha$ and $\beta$. This change in frequency, known as frequency pulling, is illustrated in Fig. 2.7 and can be calculated using the following naive approach. First, we calculate the resonance frequency as

$$\omega = \sqrt{\frac{k}{m}} = \sqrt{\frac{1}{m}\frac{d^2U}{dx^2}} = \sqrt{\omega_0^2 + 6\alpha x + 12\beta x^2}, \tag{2.42}$$

and then we calculate the Taylor expansion of the frequency for $x \to 0$ to the second order of $x$ and we obtain

$$\omega = \omega_0 + \frac{2\alpha}{\omega_0}x + \left(\frac{12\beta}{\omega_0} - \frac{9\alpha^2}{\omega_0^3}\right)x^2. \tag{2.43}$$

Thus, frequency pulling due to cubic and Duffing terms becomes

$$\begin{aligned} \Delta\omega_{\text{cubic}} &= \frac{2\alpha}{\omega_0}x - \frac{9\alpha^2}{\omega_0^3}x^2 \\ \Delta\omega_{\text{Duffing}} &= \frac{12\beta}{\omega_0}x^2. \end{aligned} \tag{2.44}$$

## Mode coupling

Just as an oscillator can interact with the environment, two oscillators can interact with one another. The potential energy of such a system must include the potential energies of the two interacting modes, plus an additional term

describing the strength of the interaction, which we will refer to as the coupling energy $E_c$. Modes can couple in many different ways depending on their coupling mechanism, but the general expression for a coupling term between two modes is

$$E_c = k_{xy} x^m y^n, \tag{2.45}$$

where the coefficient $k_{xy}$ determines the strength of the interaction between modes $x$ and $y$, and $m, n$ determine the order of the coupling. For $m = n = 1$ the coupling between the modes is linear and for $m, n > 1$ it is nonlinear. Because the resonance frequencies of the modes are

$$\omega_x = \sqrt{\frac{k_x}{m}} = \sqrt{\frac{1}{m}\frac{d^2U}{dx^2}} \tag{2.46}$$

and

$$\omega_y = \sqrt{\frac{k_y}{m}} = \sqrt{\frac{1}{m}\frac{d^2U}{dy^2}}, \tag{2.47}$$

only coupling terms with order 2 or larger in $m, n$ will affect the resonance frequency. To illustrate what the effect of mode coupling on $\omega_{x,y}$ would be, let us take $m = n = 2$. Then the potential energy is described as

$$\begin{aligned} U &= \tfrac{1}{2} m\omega_{x_0}^2 x^2 + \tfrac{1}{2} m\omega_{y_0}^2 y^2 + E_c \\ &= \tfrac{1}{2} m\omega_{x_0}^2 x^2 + \tfrac{1}{2} m\omega_{y_0}^2 y^2 + m k_{xy} x^2 y^2. \end{aligned} \tag{2.48}$$

The mode interaction causes the mechanical energy of the modes to flow from one to the other (see Fig. 2.8(a)). The interaction also causes the frequencies of the coupled modes to be pulled, and this frequency pull can be calculated using the same approach used to calculate Eq. (2.44). Calculating the resonance frequency of the $x$ mode, we obtain

$$\omega_x = \sqrt{\frac{k_x}{m}} = \sqrt{\frac{1}{m}\frac{d^2U}{dx^2}} = \sqrt{\omega_{x_0}^2 + 2\kappa_{xy} y^2}, \tag{2.49}$$

Then we calculate the Taylor expansion of $\omega_x$ to second order of $x$ under the assumptions of low amplitudes of the $y$ mode ($y_0 \to 0$) and assuming that the energy of the $x$ harmonic is larger than that in the $y$ harmonic and the mode coupling ($\omega_{x_0}^2 x_0^2 \gg \omega_{y_0}^2 y_0^2$ , $k_{xy} x_0^2 y_0^2$). Then $\omega_x$ becomes

$$\omega_x = \omega_{x_0} + \frac{k_{xy}}{\omega_{x_0}} y^2. \tag{2.50}$$

Similarly, for a Taylor expansion of $\omega_y$ to second order of $y$ under the assumption of low amplitudes of the $x$ mode ($x_0 \to 0$) and that the energy of the $y$ harmonic is larger than that stored in the $x$ harmonic and the mode coupling ($\omega_{y_0}^2 y_0^2 \gg \omega_{x_0}^2 x_0^2$ , $k_{xy} x_0^2 y_0^2$), we obtain

$$\omega_y = \omega_{y_0} + \frac{k_{xy}}{\omega_{y_0}} x^2. \tag{2.51}$$

Note that the assumptions made for the Taylor expansions of $\omega_x$ and $\omega_y$ cannot be fulfilled simultaneously. Thus, the frequency pulling due to mode coupling in the two modes becomes

$$\begin{aligned} \Delta\omega_x &= \frac{k_{xy}}{\omega_{x_0}} y^2 \\ \Delta\omega_y &= \frac{k_{xy}}{\omega_{y_0}} x^2. \end{aligned} \tag{2.52}$$

The mode coupling also causes the appearance of frequency mixing, that is, resonances with frequencies that are linear combinations of $\omega_x$ and $\omega_y$. This can also be understood trigonometrically from the coupling terms in the equations of motion. Assuming that both $x$ and $y$ oscillate in time as a cosine, the coupling terms will produce oscillations of the following form

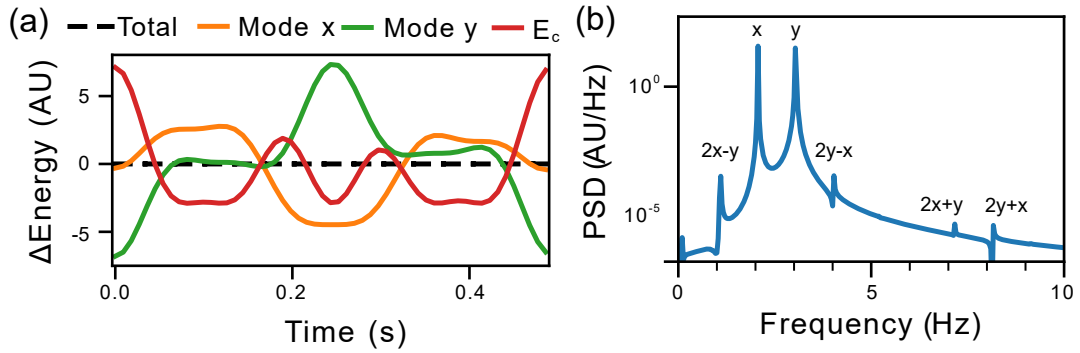


**Figure 2.8:** (a) Energies of a system with two coupled oscillators with frequencies of 2 Hz (x) and 3 Hz (y). The total energy, that is, the sum of the energy of the modes plus the coupling energy ($E_c$) remains constant, while the energies of the two modes and the energy of the mode coupling vary in time. (b) Power spectrum of the motion of the two oscillators showing a small shift from the uncoupled resonance frequencies (Eq. (2.52)) and additional peaks originating from frequency mixing, i.e. linear combinations of the frequencies of the two modes (Eq. (2.53)).

$$\begin{aligned} x^2(t)y(t) &= \frac{x_0^2 y_0}{4}\left(2\cos\omega_y + \cos\left(2\omega_x + \omega_y\right) + \cos\left(2\omega_x - \omega_y\right)\right) \\ x(t)y^2(t) &= \frac{x_0 y_0^2}{4}\left(2\cos\omega_x + \cos\left(2\omega_y + \omega_x\right) + \cos\left(2\omega_y - \omega_x\right)\right), \end{aligned} \tag{2.53}$$

the mixed frequencies are shown in Fig. 2.8(b).

In Paper C we find the nonlinear coefficients and the coupling coefficients of the $x$, $y$, and $z$ modes of the COM motion using our FEM model of the trap and the particle and show that they explain the measured frequency pulling.

# CHAPTER 3

# Methods

This chapter describes the methods used to model magnetic traps and magnetically levitated superconductors, as well as the fabrication processes used to make chip traps and microparticles. We will explain the basic operation of the cryostats where the experiments were performed, how the motion of the levitated particles is measured, and how it is controlled using feedback.

## 3.1 Modeling

In the following, we will introduce the methods used to model the magnetic traps.

First, we show analytical equations based on Maxwell's equations and on idealizations of the actual magnetic traps. They capture the physics well

enough to predict properties such as trap stiffness. However, they fail to capture effects from arbitrary shapes both of the superconducting particle and the magnetic field distribution. These effects must be taken into account because they change the trap properties and can make them unstable.

In order to account for such effects, we use numerical simulations based on the Maxwell-London equations and the actual geometry of both the magnetic trap and the particle. The numerical model provides a full picture of the magnetic field distribution of the trap and the particle, which contains the information needed to describe the full dynamics of the particle motion, i.e., trap frequencies, libration, and nonlinearities.

## Analytical model

As shown in Section 2.2, the energy of a superconductor in a magnetic field can be calculated analytically, provided that one can approximate the superconducting object as a point particle. Thus, an analytical formula for the potential energy of a magnetically levitated superconductor can be found, provided that there is also an analytical formula for the magnetic field distribution.

Fortunately, magnetic traps that consist of magnets and coils can be approximated to collections of one-dimensional current loops with varying radii, current, and orientation. The magnetic field distribution generated by a one-dimensional current can be calculated analytically using the Biot-Savart law

$$\vec{B}(\vec{r}) = \frac{\mu_0 I}{2\pi} \int \frac{d\vec{l} \times (\vec{r} - \vec{r}')}{|(\vec{r} - \vec{r}')|^3}, \tag{3.1}$$

where $I$ is the current in the loop, $\vec{r}'$ displacement of the current with respect to the origin, and $\vec{r}$ is the point at which the field is being calculated. In our case, to obtain the equation describing the magnetic field, we solve Eq. (3.1) for a circular current loop, where $\vec{l}$ is the differential line element of a circle.

The equations for the vector components magnetic field generated by a current loop of radius $a$ and current $I$, with the origin of the coordinate

system centered at the center of the loop, are [100]

$$B_x = \frac{Cxz}{2\alpha^2\beta\rho^2}\left[(a^2+r^2)E(k^2)-\alpha^2K(k^2)\right] \tag{3.2}$$

$$B_y = \frac{Cyz}{2\alpha^2\beta\rho^2}\left[(a^2+r^2)E(k^2)-\alpha^2K(k^2)\right] \tag{3.3}$$

$$B_z = \frac{C}{2\alpha^2\beta\rho^2}\left[(a^2+r^2)E(k^2)-\alpha^2K(k^2)\right] \tag{3.4}$$

where $C = \mu_0 I/\pi$, $\rho^2 = x^2+y^2$, $r^2 = x^2+y^2+z^2$, $K$ and $E$ are elliptical integrals of the first and second kind, respectively, $k^2 = 1-\alpha^2/\beta^2$, $\alpha^2 = a^2+r^2-2a\rho$ and $\beta^2 = a^2+r^2+2a\rho$. Because of the presence of elliptical integrals, these formulas can only be evaluated numerically. However, numerical evaluation of such integrals is perfectly feasible with current desktop computers and is much faster than finite element analysis.

These equations can be used to analytically calculate the magnetic field distribution of one current loop above another, with counter-propagating currents (Fig. 3.1(a)). This type of arrangement is known as an anti-Helmholtz coil, which generates an almost magnetic quadrupole field distribution between the coils, and is very similar to the magnetic field that our magnetic chip traps generate.

These equations can be used to estimate the properties of the magnetic traps, such as the potential energy landscape that the particle will experience in the trap and thus, magnetic forces, trap stiffness, and trap frequency (see Section 2.5).

These equations have been used to make fast and reasonably accurate estimates of the stability and properties of different magnetic trap architectures, which have been very useful in designing magnetic traps.

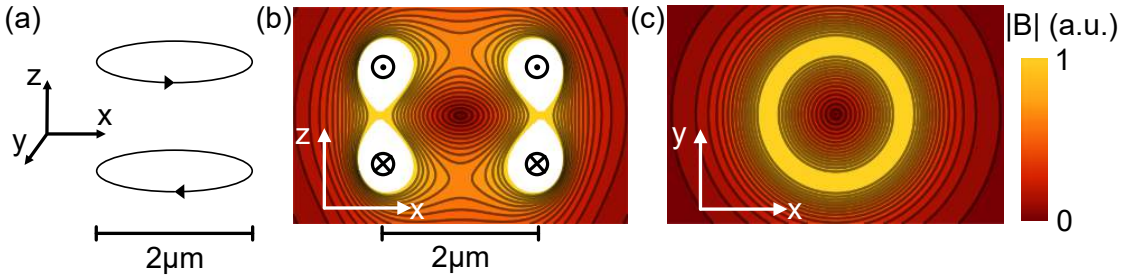


**Figure 3.1:** (a) Schematic representation of two current loops and (b,c) cut planes of their corresponding magnetic field distribution calculated with Eqs. (3.2) to (3.4).

## Image method

A magnetically levitated superconductor can also be modeled as a set of currents within the superconducting volume that mirror the magnetic field outside the superconductor. In order to calculate the currents within, the magnetic field normal to the surface of the superconductor is set to zero using the boundary condition

$$\vec{B}(\vec{r}) \cdot \vec{n}(\vec{r}) = 0, \tag{3.5}$$

where $\vec{B}(\vec{r})$ is the magnetic field and $\vec{n}$ is the surface vector that defines the surface of the superconductor.

Given an external magnetic field and the geometry of the levitated superconductor, the equations for the magnetic field and the supercurrent distributions inside the superconducting volume can be found [97], [101]. Analytical solutions for simple cases such as a spherical superconductor in a quadrupole field are available [102]. However, analytical solutions for complex shapes for the particle and the magnetic field distribution are very hard to find. We will not go into detail on the image method as this method has not been used for the design or the simulation of the devices, but it deserves mention as it is touched upon in Paper A.

## Finite element method

In this thesis, we have made extensive use of finite element method (FEM) simulations to study, design, and understand different types of magnetic traps. FEM is a necessary tool in order to account for asymmetries, extended volumes, and complex geometries of both chip-based traps and superconducting particles. Specifically, the openings of planar coils (Fig. 3.10), and the non-negligible size of the superconducting particles with respect to the magnetic trap (Fig. 3.6), lead to significant deviations from analytical models [37].

For this purpose, we developed a new FEM implementation of superconductivity based on the $\vec{A}$-$V$ formulation. What this means is that the magnetic and electric fields are expressed as functions of an electric scalar potential ($V$) and a magnetic vector potential $\vec{A}$ as

$$\vec{B} = \nabla \times \vec{A} \tag{3.6}$$

$$\vec{E} = -\vec{\nabla} V + \frac{d\vec{A}}{dt}. \tag{3.7}$$

Thus, the dependent variables for which the Maxwell equations are solved are the magnetic vector potential $\vec{A}$ and the electric scalar potential, i.e. the voltage $V$. The choice of $\vec{A}$-$V$ formulation over other formulations such as $\vec{T}$-$\Omega$ formulation (where $\nabla \times \vec{T} = \vec{J}$ and $\Omega$ is a scalar potential associated with magnetic surface poles) or $\vec{H}$ formulation, that have other dependent variables is that it is relatively simple to implement the Maxwell and London equations in terms of $\vec{A}$ [103].

The equation we used to implement superconductivity is based on a simplification of Eq. (2.18) for the supercurrent in which the phase of the wave function $\theta$ is neglected, which results in

$$\vec{J}_s = -\frac{1}{\mu_0 \lambda_{\mathrm{L}}^2} \vec{A}, \tag{3.8}$$

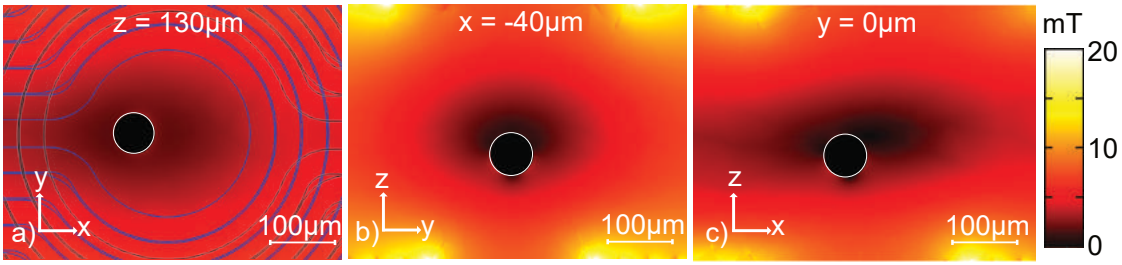


**Figure 3.2:** Cut planes of the magnetic field distribution of a superconducting sphere levitated inside a magnetic chip trap with 0.5 A running in the coils. The zero of the coordinate system is the center of the bottom coil.

where $\lambda_{\mathrm{L}} = \sqrt{\frac{m_e}{\mu_0 n_s e^2}}$ is the London penetration depth, $n_s$ is the supercarrier density, and $e$ and $m_e$ are the electron charge and mass, respectively.

Implementing Eq. (3.8) in the FEM software as an external contribution to the current density in the superconducting domains allows to model said domains as superconductors in the Meissner state. What this means is that the models will compute a magnetic field distribution within the superconductor that will account for finite $\lambda_{\mathrm{L}}$ and will also calculate the current density distribution within the superconductor. A typical simulation of the magnetic trap and the levitated particle is shown in Fig. 3.2.

In our simulations, the Maxwell equations are solved in the quasi-static regime, so all time derivatives equal zero and thus play no role. That said, it is possible to model superconductors in the frequency regime using the same approach, which we demonstrated by simulating superconducting co-planar waveguides in the microwave regime in Ref. [79].

We must also point out that this implementation of the Maxwell-London equations provides accurate results only for type I superconductors in the Meissner state and for type II superconductors in magnetic fields $B < B_{\mathrm{c1}}$. For $B > B_{\mathrm{c1}}$ magnetic flux vortices will start nucleating in the superconductor and Eq. (3.8) is insufficient to capture the physics of the system.

Additionally, because our model does not account for the contributions of the wave function's phase [right-hand side of Eq. (2.19)], the implementation

of Eq. (2.18) doesn't account for fluxoid quantization.

However, we can account for flux quantization ad hoc by neglecting the magnetic flux threading the superconducting material at the edge of a hole in a superconductor, i.e., the magnetic flux threading the outermost part of the superconductor, where the magnetic field penetration depth allows part of the external magnetic field in the volume. This approximation is valid provided that the dimensions of the superconductor with the hole are much larger than $\lambda_L$ [104].

We implement flux quantization in our FEM models in an ad hoc manner by defining the area of a hole in the superconductor over which Eq. (2.18) is integrated. We impose an arbitrary amount of trapped flux ($N\Phi_0$) and an additional contribution to the current density in the ring such that the constraint

$$N\Phi_0 - \Phi_{\text{hole}} = 0 \tag{3.9}$$

is fulfilled within the area of the hole in the superconductor. In this way, quantized flux in a hole inside a superconductor can be modeled, which is essential to understanding the behavior of levitated superconducting rings [37].

The output of the FEM simulations are the electric field ($\vec{E}$), magnetic field ($\vec{B}$), and current density ($\vec{J}$) distributions within the simulation box. Knowing the magnetic field distribution inside and outside the particle (see Fig. 3.2), allows us to calculate the magnetic force acting on the particle by means of the Maxwell stress tensor $T$, as described in Section 2.5.

## 3.2 Fabrication

In the following, we will describe the fabrication process of superconducting particles, as well as the fabrication and assembly of the magnetic traps produced during this thesis.

Note that for all microfabrication processes, we have used undoped silicon wafers with [100] crystallographic orientation. This was done because all superconducting materials we can deposit in our clean room facilities are compatible with silicon substrates and because there is a wealth of knowledge and expertise on silicon microfabrication.

We have used niobium as the superconducting material of choice for microfabrication. The reasons for this are that niobium has a critical temperature (of 9 K) well above 4 K, which was the base temperature of the first cryostat used for levitation experiments. Further, niobium has one of the largest critical current densities among superconductors (we have measured up to $50\,\mathrm{GA\,m^{-2}}$ for niobium wire-bonds compared to $1\,\mathrm{GA\,m^{-2}}$ for aluminium) [105], [106], and it also has a very large first critical field ($B_{c1}$ =170 mT) which means it can be considered to be in the Meissner state up to rather large fields [107].

## Particles

Even though only near-spherical particles have been levitated in the experiments shown in this thesis, two types of superconducting microparticles have been produced. Flat rings and discs made of niobium via microfabrication, and spherical lead particles via ultrasonic cavitation. Tin-lead spheres have also been levitated, but they were purchased, not manufactured. In the following, we will explain the fabrication processes for each type of particle.

### Microfabrication of disks and rings

The fabrication of flat microparticles starts with spin-coating a layer of photosensitive resist on top of a Silicon substrate. The resist is heated up to 180 °C for 5 min in order to remove all remaining solvents in the resist. This is known as "hard-baking" and it is done so that when the niobium is sputtered on the resist, the solvent doesn't produce bubbles under the deposited layer. Then we sputter a niobium layer on top of the resist, see Fig. 3.3. After that, another layer of resist is spin coated and patterned with a laser-writer lithog-

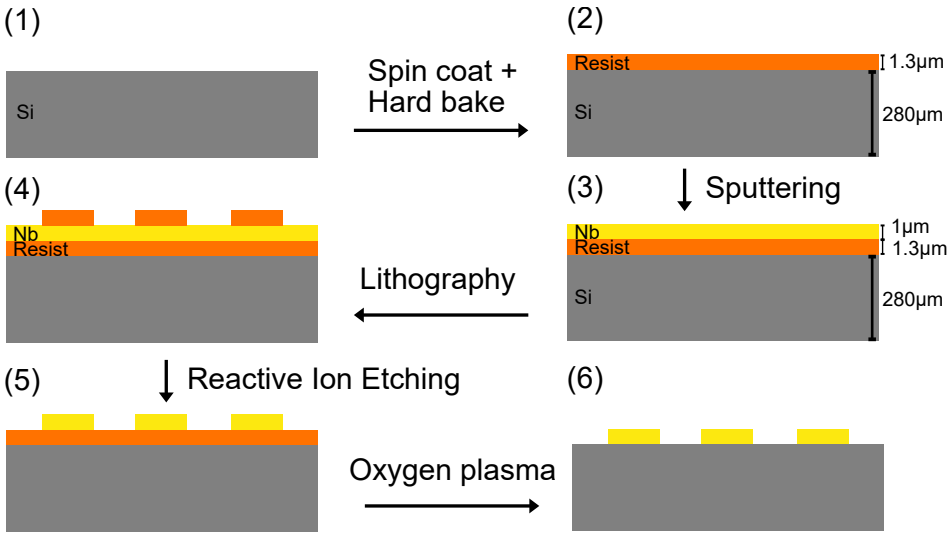


**Figure 3.3:** Process flow for the fabrication of planar niobium particles.

raphy machine. The resist is developed, and the exposed niobium is removed by reactive ion etching (RIE). At this point, the particles are standing on top of a support made of resist, which is then removed by oxygen plasma. This drops the particles on the Silicon substrate with no attachment other than the surface interaction (see Section 2.4).

This process has the key advantage of being able to fabricate the particles in situ, i.e., inside the magnetic traps, and leaving them detached from the substrate for further manipulation (Fig. 3.5). Furthermore, one can fabricate particles of arbitrary shapes, as long as they are planar, see Fig. 3.4. The drawback is that due to their planarity, the contact surface between the particle and the substrate is much larger than that of a sphere with a plane, and so the adhesion force is also much larger, which makes lifting them off the substrate, and thus levitating them, harder.

### Ultrasonic cavitation of microspheres

We produced lead microspheres through the process known as ultrasonic cavitation [108]. In this method, a pellet of lead is placed inside a borax vial filled with silicone oil, which has a boiling point of 390 °C. This implies that this

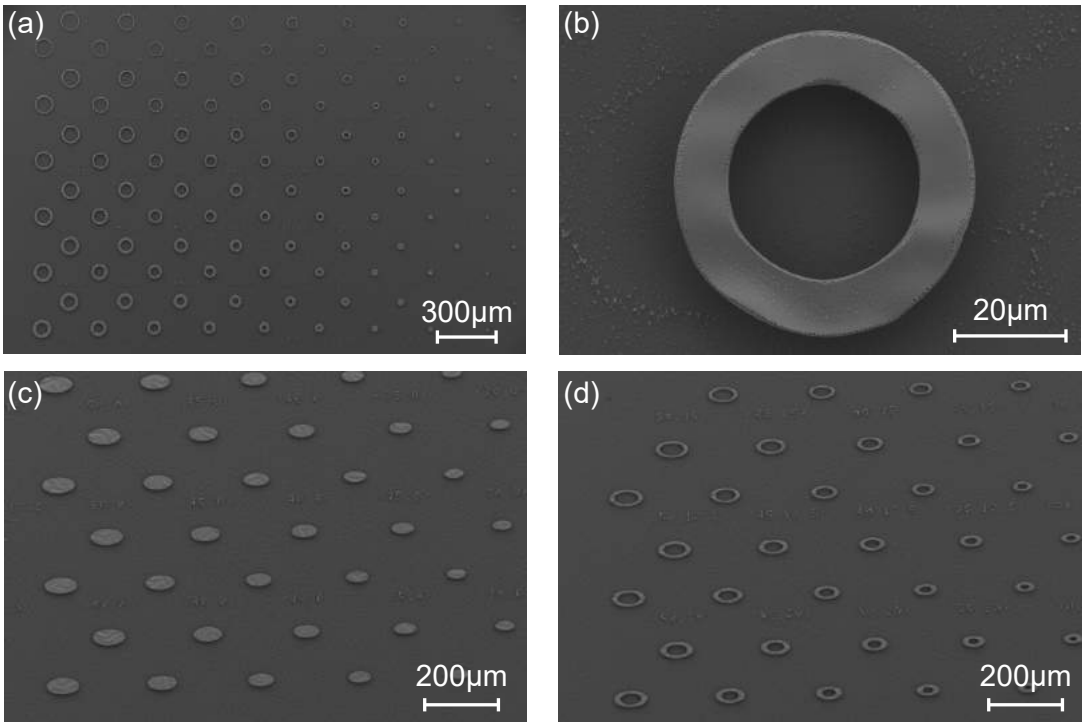


**Figure 3.4:** Scanning electron microscope (SEM) pictures of arrays of planar niobium particles of different sizes with the shape of (a) circular rings, (c) ellipses, and (d) elliptical rings. (b) Magnified view of a circular niobium ring. All the particles are 1 µm thick. All pictures have been taken using a top view detector, that is to say, pictures (c) and (d) do not show circular particles viewed at an angle, but actually elliptically shaped particles.

process only works for materials with a melting temperature lower than this boiling point. A flame is used to heat up the contents of the vial up to the melting temperature of lead 330 °C, which makes the liquid lead precipitate to the bottom of the vial. Then, the ultrasonic transducer is turned on for 10 s, which makes the steel rod shake the liquids and disperses the liquid lead into micro droplets that float in the silicone oil. After that, the flame is extinguished and the sudden drop in temperature causes the droplets to freeze. This results in the vial being filled with lead micro powder, with particles of many sizes and shapes, some of them almost completely spherical.

In order to separate the particles from the silicone oil, the dispersion is diluted with hexane, centrifuged at 6000 rpm for 1 minute, and then further

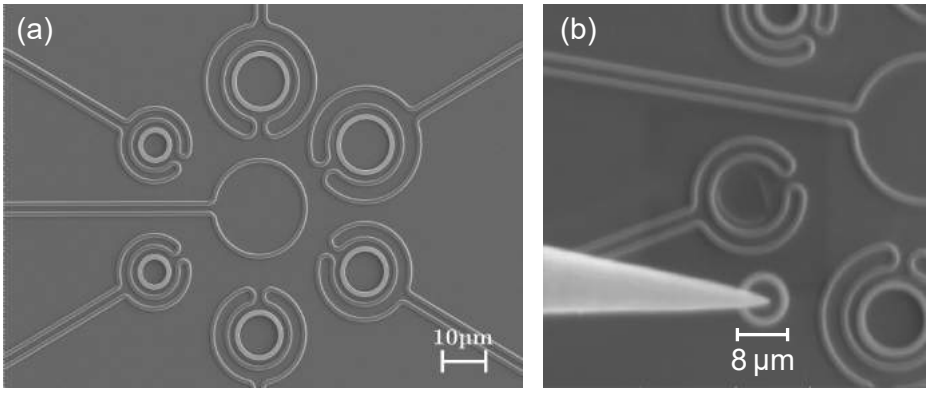


**Figure 3.5:** SEM pictures of (a) niobium rings fabricated within planar magnetic traps and (b) the same rings being picked and placed with a micromanipulator inside the SEM.

diluted with acetone and iso-propanol. The particles after rinsing are shown in Fig. 3.6(b). Once the particles are clean, we cast some droplets of the clean dispersion on a chip, and we can pick out individual spheres with a micromanipulator under an optical microscope.

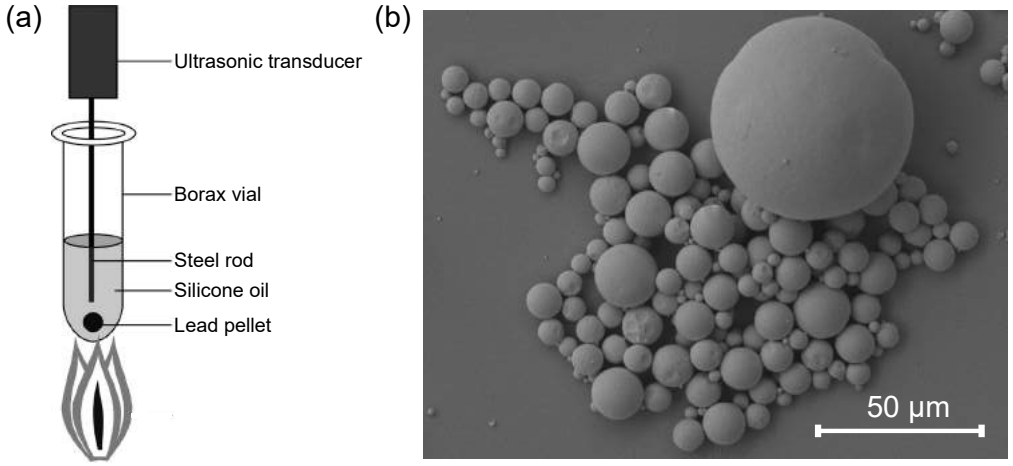


**Figure 3.6:** (a) Schematic representation of the ultrasonic cavitation setup used to produce lead microspheres (adapted from [108]) and (b) scanning electron microscope picture of the resulting lead microspheres.

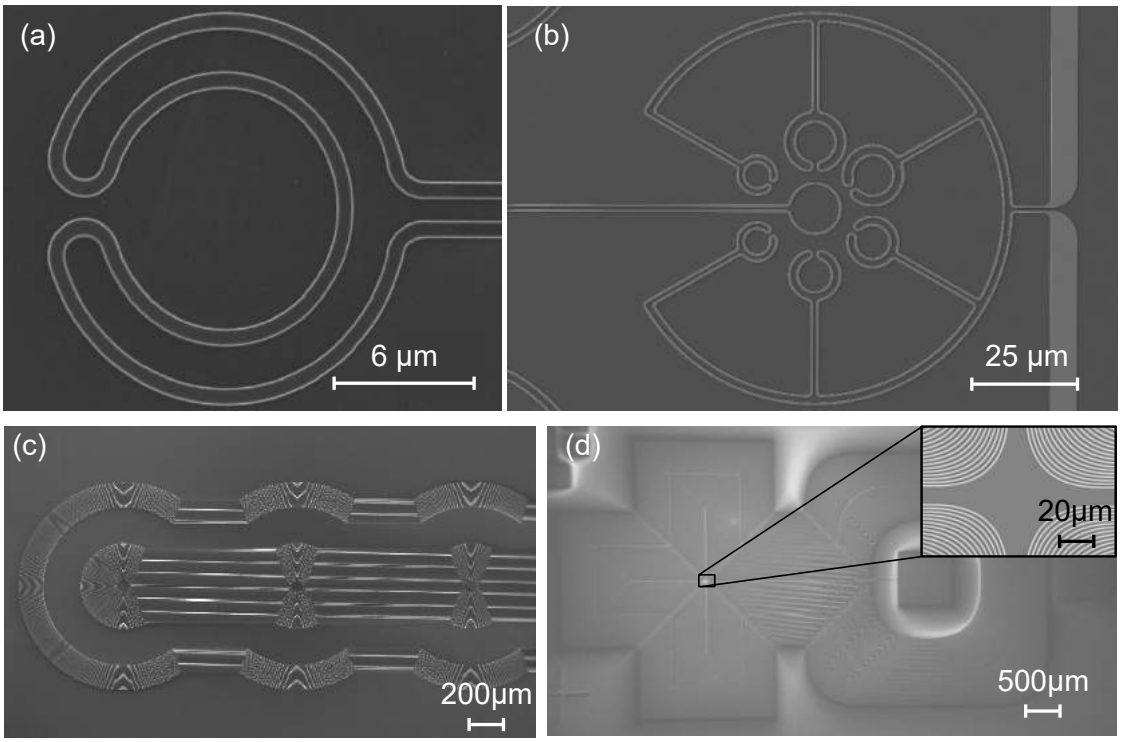


**Figure 3.7:** SEM pictures of several generations of planar traps in chronological order. The cross-like trap structure in (d) has 500 windings in total.

## Planar traps

The first generation of chip-based magnetic traps was based on planar coils. This was done because the modeling of such structures predicted stable trapping of superconducting particles [37]. While that was correct, we failed to account for the strength of the Van der Waals interactions between the particle and substrate (Section 2.4). The planar traps were able to move the particles, but despite the number of windings [up to several hundred Fig. 3.7 (d)], they were never capable of levitating them because they could not generate strong enough magnetic fields.

Despite this, we managed to develop a very robust fabrication process, which we later used for fabricating the two-chip traps and the niobium rings and discs (see the following Subsection). The process [illustrated in Fig. 3.8] starts with a 1 µm thick layer of niobium sputtered on a Silicon substrate. We

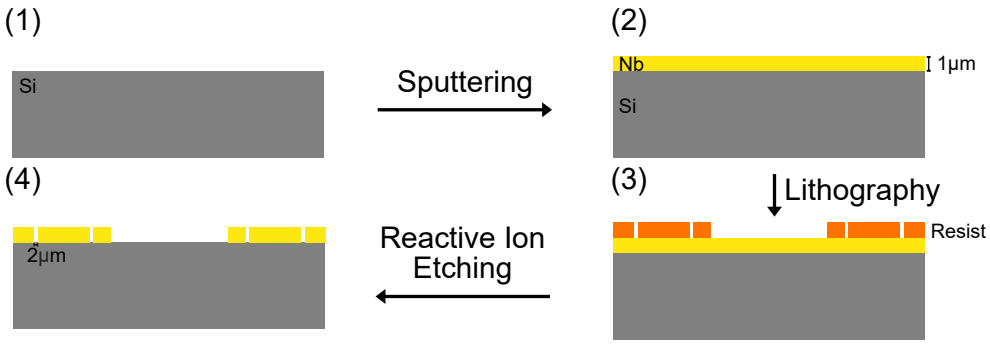


**Figure 3.8:** Process flow for the fabrication of planar traps. The superconducting coils of the two-chip traps are fabricated in the same way.

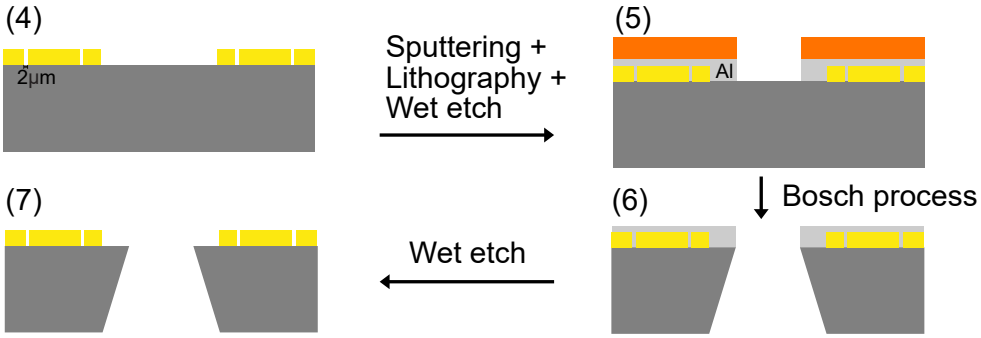


**Figure 3.9:** Process flow for the fabrication of the holes in the top chips of the magnetic two-chip traps. The fabrication starts from step (4) in Fig. 3.8.

would have preferred thicker layers of niobium to carry as much current as possible, but thicker niobium layers detached from the silicon substrate due to excessive amounts of stress in the deposited film.

The niobium layer is patterned by means of laser lithography and RIE. This will result in a silicon chip with several niobium coils, see Fig. 3.10(b).

## Two-chip traps

To levitate the superconducting particles, we have used two-chip stacks, each containing planar coils of their own. The fabrication of the bottom chip is the same as for the planar traps, shown in Fig. 3.8.

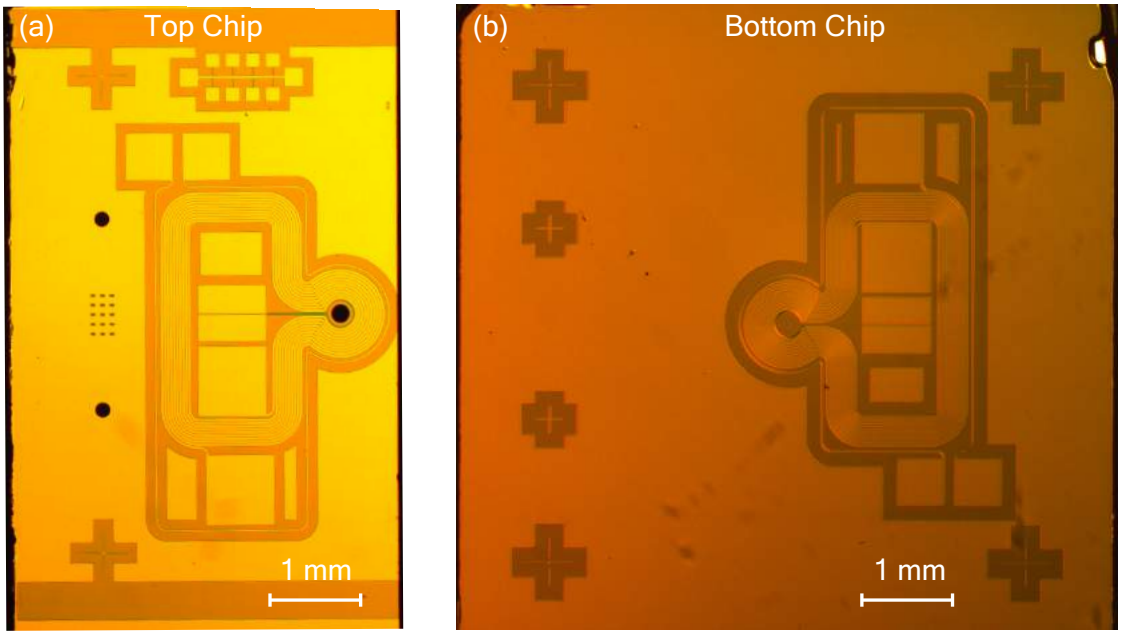


**Figure 3.10:** Top view of (a) the top chip and (b) the bottom chip of a two-chip trap.

To produce the top chips, we start with the same fabrication process as the bottom chip and the planar traps. After that, a hole must be etched within the inner radius of the trap coil through the entire substrate, so that there is a volume within which we can place and levitate a microparticle. The fabrication process for this is illustrated in Fig. 3.9. For this purpose, an aluminium layer is sputtered on the device, and an opening is created in the trap region via lithography and wet etching of the aluminium. Then the device is etched using the Bosch process, which etches silicon anisotropically, allowing us to etch a hole from top to bottom of the Silicon substrate. The remaining aluminium is etched away, and the top chip is finished. A top view of the resulting chip is shown in Fig. 3.10(a), where the black regions are holes in the silicon substrate.

## Vias

One of the limiting factors in how strong a magnetic field can be generated by a planar coil is how many windings the coil can have. A planar coil configuration

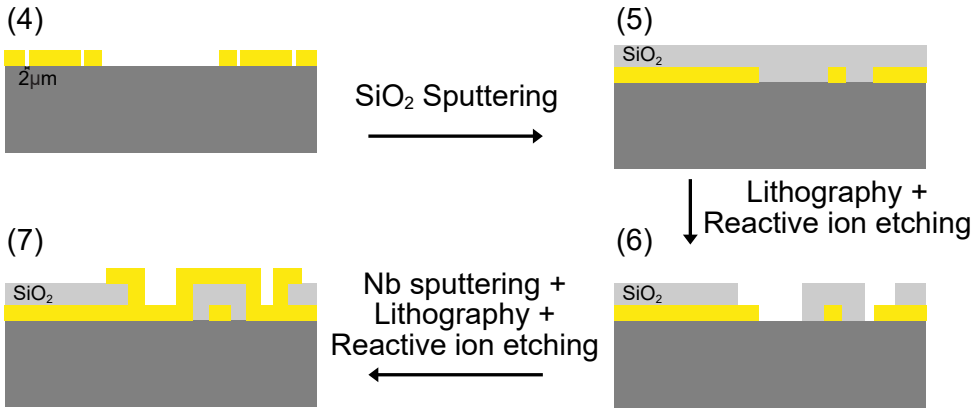


**Figure 3.11:** Process flow for the fabrication of vias on a planar coil. The process starts after step (4) in Fig. 3.8.

without crossings implies that (i) there must be an opening in the coil and (ii) that each new winding has to go around the first contact pad (see Fig. 3.10).

One way to avoid these issues is to introduce crossings in the form of vias, which are interconnects going either above or below other structures on the same chip. The fabrication process is shown in Fig. 3.11. Once a planar coil has been fabricated, it is covered under a layer of silicon dioxide grown via Atomic Layer Deposition (ALD). The silicon dioxide acts as an insulating layer between the coil at the bottom and the interconnect at the top. It is important that the layer is chemically grown with ALD because chemical deposition (as opposed to physical deposition, such as sputtering) of materials is conformal. This means that the layer grows on the top surfaces as well as on the sidewalls, which will fully insulate the coil underneath.

If this insulating layer were sputtered, the top layers would be covered, but not the entirety of the sidewalls due to the niobium structure being rather tall (1 µm), which would lead to undesired electrical contacts.

Then the silicon dioxide layer is etched at the areas where the coil underneath has to be electrically connected. A new niobium layer is sputtered and patterned to leave only a wire connecting those two areas, closing the circuit of the coil. An actual via is shown in Fig. 3.12.

Despite the fact that the fabrication process worked, no vias have been

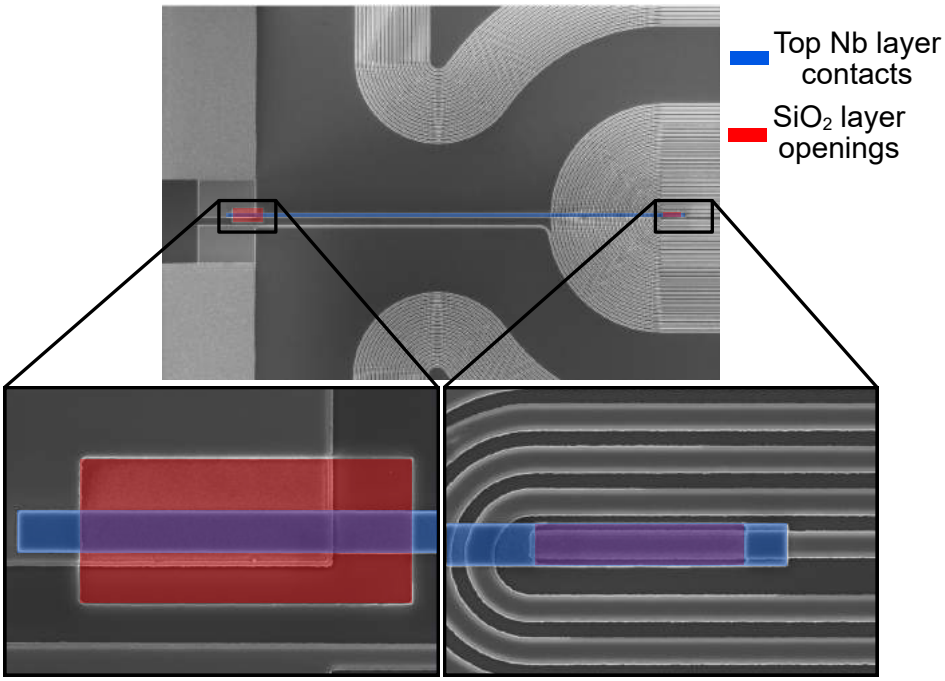


**Figure 3.12:** SEM pictures of a planar multiwinding coil. The entirety of the chip is covered in silicon dioxide, except the areas marked in red and blue. The red area indicates where the silicon dioxide has been etched away, and the blue area indicates the second layer of niobium, which has been patterned into a wire that connects the wire-bonding pad (big square on the left) and the contact inside the multiwinding coil (inset on the right). The insets show larger magnification pictures of the vias.

used in the devices shown to levitate particles in this thesis. The reasons are twofold. First, while the designs could benefit from having vias in that they would generate stronger magnetic field gradients, the benefit would be marginal. Second, the ALD machine has proved unreliable in that it has been idle in need of servicing for a longer time than it has been functional. Thus, it was decided to not continue with this kind of trap.

## Trap assembly

The magnetic trap is composed of two chips, each with several micro-fabricated sets of niobium superconducting coils, see Fig. 3.10. The chips are manually stacked on top of each other and aligned under an optical microscope. Once a satisfactory alignment has been achieved, minute droplets of BF-6 glue are applied with a micro-pipette to the corners of the bottom chip, and the sample is left to dry.

After the two-chip trap is assembled it is glued to a sample holder that carries niobium bonding pads, and the chip coils are wire-bonded to the contact pads on the sample holder with 25 µm diameter niobium and aluminium wire with a wedge-bonder (Fig. 3.13). In order to wire-bond with niobium wire, the wire must first be softened by heating. This is done by applying 150 mA of current to a 17 cm long piece of wire inside a vacuum chamber for five minutes [109]. This temporarily softens the wire, such that wire bonding with it is possible up to a week after softening. Niobium is preferred for wire bonding because it has both a larger critical current density and critical temperature than aluminium (the material used by default), which allows us to operate the trap without heat dissipation below the critical temperature of niobium (9 K).

Thus, the primary function of the niobium wire bonds is to carry the trap current without heat dissipation, whereas the aluminium bonds serve as a fail-safe in case the critical current of the niobium bonds is reached.

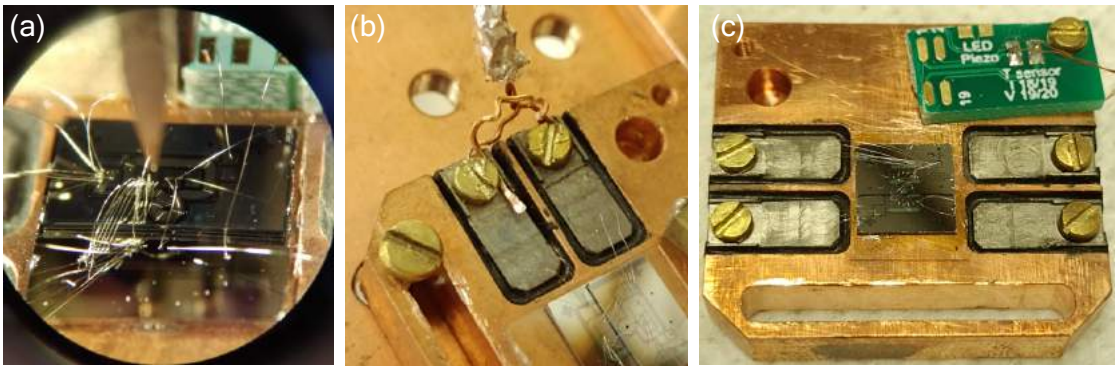


**Figure 3.13:** Optical microscope pictures of an assembled two-chip trap with the wire bonds between the two chips and the sample holder. (b) Picture of the connections between a two-chip trap and a twisted pair of superconducting wires used to provide electrical current to the coils in the trap. (c) Picture of the copper sample holder with a wire-bonded two-chip trap.

## 3.3 Setup and measurement techniques

### Cryogenics

All the experiments presented in this thesis have been performed at cryogenic temperatures. Two dry (i.e., liquid helium-free) cryostats were used during this thesis. The first experiments were performed in a AttoDRY800 cryostat, which uses a Gifford-Mac Mahon (GM) cooler, and can cool the experiment down to 4.5 K. The later experiments were performed in a BlueFors LD250 dilution refrigerator, which uses a pulse tube cooler and a dilution refrigeration unit, and can cool down the experiment down to 50 mK. The following sections explain the working principle behind each cryostat.

#### Gifford-Mac Mahon cooler

A GM cooler is a cooling machine based on the Gifford-MacMahon cycle. This cycle is based on isobaric compression and expansion of Helium gas at the cold side of a container, represented in Fig. 3.14. In the first step of the cycle, high-pressure Helium is pushed into the volume of the cooler. In the second

step, the regenerator, which is a solid piece of porous material with a large heat capacity, is displaced towards the hot side of the container, isobarically expanding the gas near the cold end. Then, in the third step, a valve switches the high-pressure helium for lower-pressure helium, isochorically reducing the pressure, which causes the volume to cool. Finally, in the fourth step, the regenerator is pushed back to the cold end, and the cycle repeats.

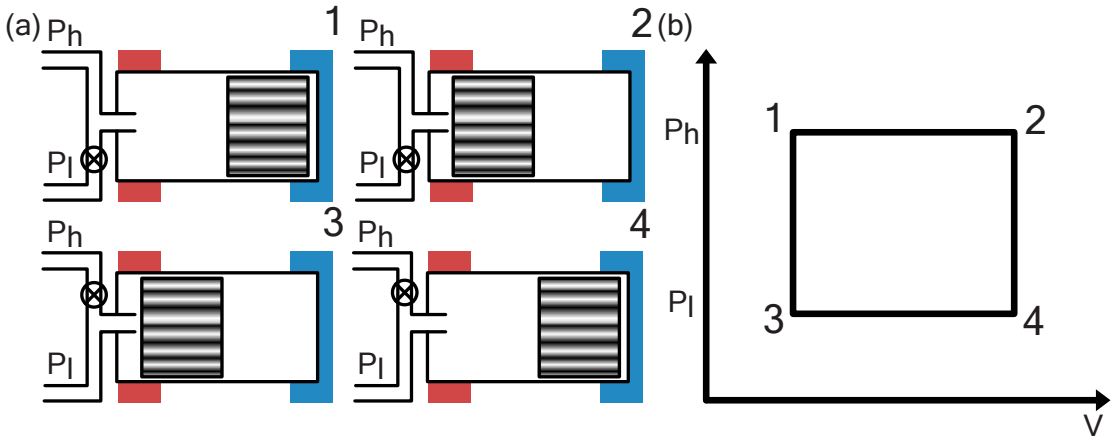


**Figure 3.14:** (a) Steps of the GM cycle illustrated in the GM cooler and (b) in a P-V diagram.

Current GM coolers can achieve temperatures as low as 2.5 K [110]. Compared to pulse tube coolers with the same cooling power, GM coolers are cheaper, and can operate with any orientation, but generate more vibrations, and require more frequent maintenance.

### Pulse tube cooler

A pulse tube cooler also provides cooling by using decompressing gas. A compressor pushes high-pressure gas (typically 19 bar Helium) through a regenerator. The regenerator is a piece of porous material within which the high-pressure gas is forced into a large volume through many small constrictions, causing the gas to expand and cool down. The gas then exchanges heat with the environment (the cryostat) and the now hotter gas is sent out, cooled with a heat exchanger, and re-compressed by the compressor to start the cycle anew.

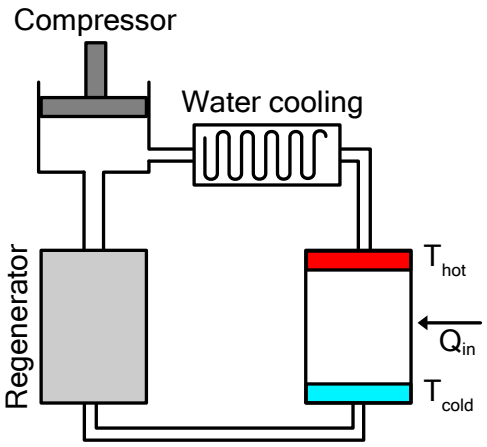


**Figure 3.15:** Schematic representation of a pulse tube cooler.

Pulse tube coolers have advantages over GM coolers; they can reach lower temperatures (down to 2.2 K [111]) and they produce fewer vibrations due to them having no moving parts near the cold head ($T_{\text{cold}}$). However, they still generate some vibrations due to the moving gas within the cold head. Further, they are more expensive than GM coolers of the same cooling power, and they can only operate vertically with the cold head facing downward when operated at low frequencies (1-3 Hz) [112].

### Dilution refrigeration

Dilution refrigerator (DR) systems are the only cooling machines that provide continuous cooling power at temperatures below 300 mK and can achieve temperatures <10 mK without moving parts. A DR uses the endothermic mixing of the two isotopes of helium, 3-He and 4-He, to provide cooling. To use the dilution refrigeration cooling cycle, one must first liquefy a 3-He and 4-He mixture, so a temperature below 4.2 K must be reached by some other means.

Below 2.7 K, pure 4-He undergoes a phase transition from a normal fluid to superfluid. Diluting the 4-He with 3-He decreases the superfluid transition temperature, see Fig. 3.16. At temperatures lower than 0.8 K the 3-He/4-He mixture will separate into two phases: a concentrated 3-He phase (with normal 4-He) and a dilute 3-He phase (with superfluid 4-He). Near absolute

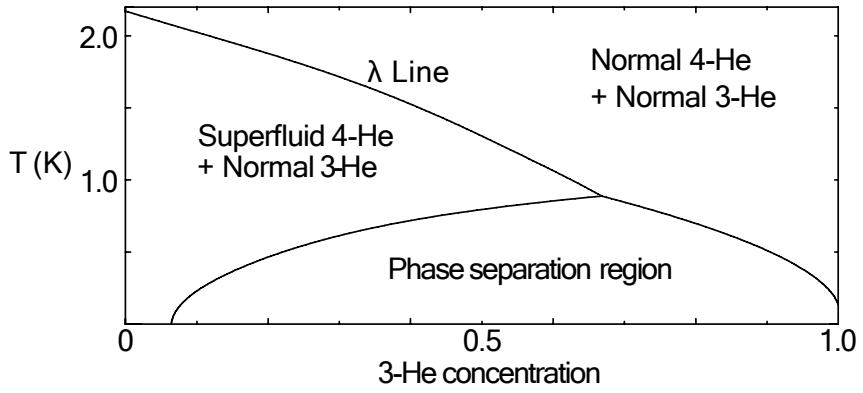


**Figure 3.16:** Phase diagram of 4-He/3-He mixture, adapted from [113].

zero temperatures, the concentrated phase becomes pure 3-He, while the dilute phase still contains 6.4% of 3-He. Because the energy of 3-He in the dilute phase is larger than in the concentrated phase, energy is required to move 3-He atoms from the concentrated to the dilute phase. This energy is taken from the environment in the vicinity of the helium mixture, which is where the experiment is fixed (mixing chamber).

The implementation of this process is shown in Fig. 3.17. On the mixing chamber of the dilution refrigerator sits a U-shape tube. One side of the tube is pumped. Because the vapor pressure of 3-He is larger than that of 4-He, the mixture on this side of the tube continuously loses 3-He. The evaporated 3-He is pumped to the other side of the tube (concentrated phase) and dissolves in the 4-He, absorbing heat.

## Magnetic shielding

Because the particle motion is measured via the magnetic flux perturbations it produces as it moves, the reduction of background magnetic fields and magnetic noise is of great importance.

In order to reduce magnetic noise in the experiment, a multilayered combination of high permeability and superconducting shielding is employed. High permeability materials (such as mu-metal and cryoperm) are materials with very large relative magnetic permeability ($\mu_r$). They can be used as mag-

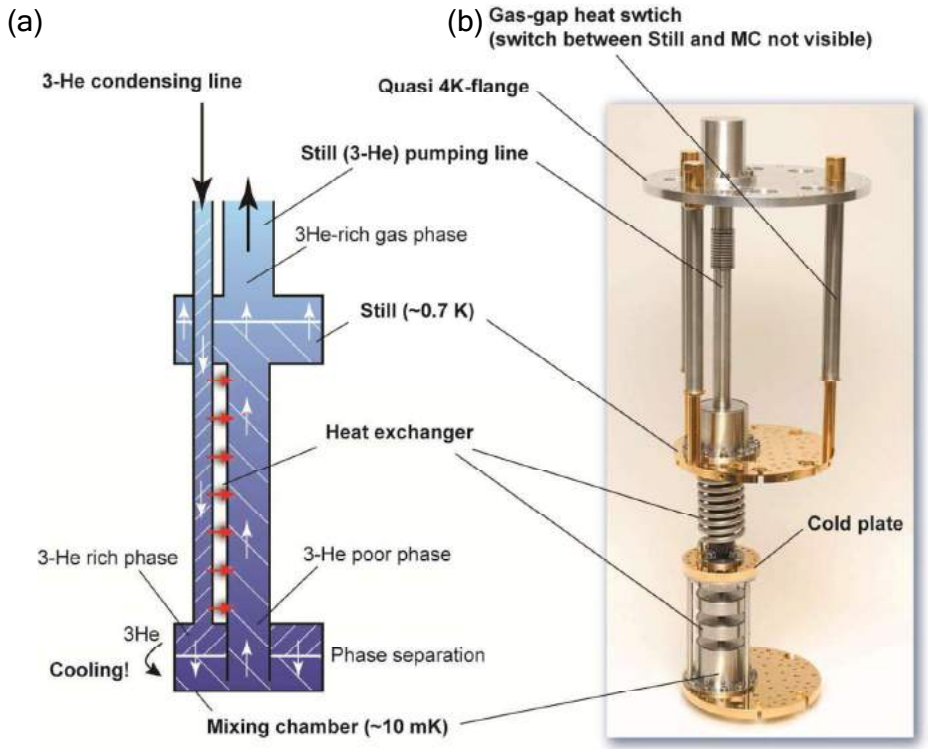


**Figure 3.17:** (a) Schematic view of a dilution unit and (b) a picture of a dilution unit of a Bluefors dilution refrigerator (figure from Bluefors User Manual).

netic shields because they draw magnetic field lines inward to their volume [Fig. 3.18(a)]. Superconducting materials also provide magnetic shielding due to the fact that they expel magnetic fields from within their volume [Fig. 3.18(b)]. If a basket is made from either of these materials, and a magnetic field is applied to them, the magnetic field within the basket $B_{\text{in}}$ will be lower than the field outside $B_{\text{out}}$.

Note that mu-metal shields provide magnetic shielding from room temperature, whereas superconducting shields provide magnetic shielding only below their critical temperature.

The magnetic trap is placed within two baskets, the innermost made of niobium and the outermost made of mu-metal Fig. 3.19 (a). These baskets are wrapped with a lead basket with a lead cover, both of which are coated with aluminium and mu-metal foil (Fig. 3.19 (b)). The mu-metal shields

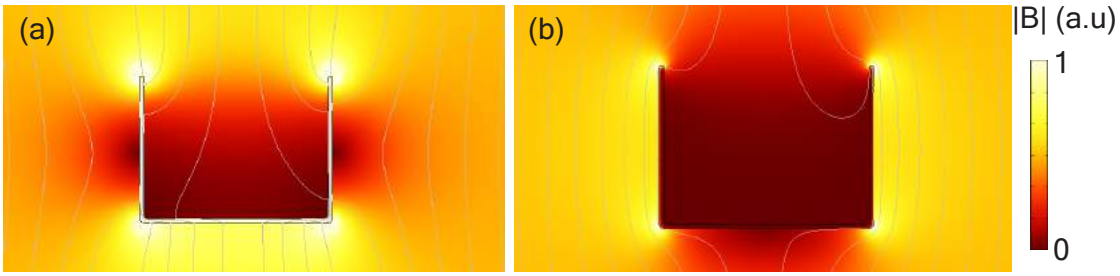


**Figure 3.18:** Cross-sections of FEM simulations of the magnetic field distribution around (a) a mu-metal basket and (b) a superconducting basket under a vertical homogeneous magnetic field.

the superconducting shields within it during cooldown. Once the niobium, lead, and aluminium become superconducting, they provide further magnetic shielding.

We note that our samples are not shielded by the superconducting shields during cooldown, only the mu-metal tape. This is because the samples are made of niobium, which has a larger $T_c$ (9.1 K) than both aluminium and lead (1.1 K and 7.2 K, respectively). That is to say, there is no superconducting shielding of the magnetic traps until below 9.1 K.

In our experiments, we found that the basket arrangement [Fig. 3.19 (a,b)], despite having a lid, shields the external magnetic field less than the aluminium cover around the still can [Fig. 3.19(c)]. This was tested by waving a magnet outside the cryostat and checking whether the SQUID magnetometer could detect the changing external magnetic field. Doing this test at 4 K allows us to test the magnetic shielding of the niobium and lead baskets together, and by doing the test at 50 mK we test the magnetic shielding of all magnetic shields, aluminium included.

How much magnetic insulation a magnetic shield provides is quantified with the shielding factor ($B_{\text{out}}/B_{\text{in}}$). The shielding factor of a magnetic shield shaped as an open-ended box is larger for boxes with a larger aspect ratio, regardless of the size of the opening of the box [114]. The shielding factor achieved in the experiment is hard to assess because we do not know the magnetic field strength of the noise outside the magnetic shielding (unless we run the experiment with no shielding). FEM simulations of the shields

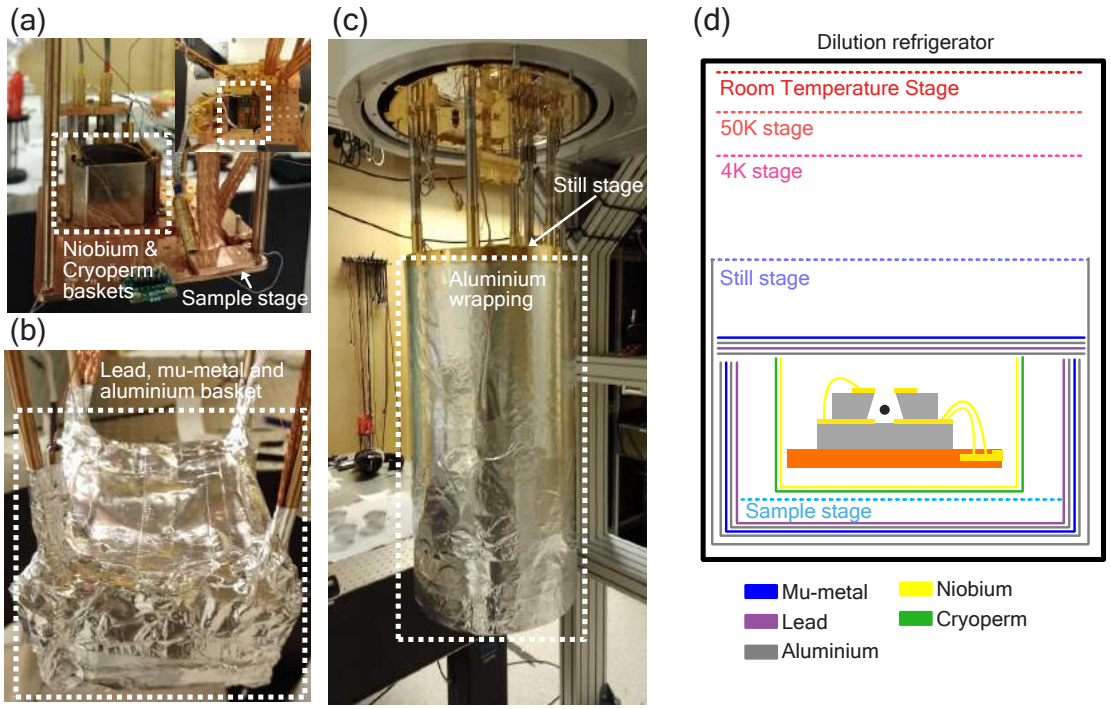


**Figure 3.19:** Magnetic shields shown from innermost to outermost, highlighted within the white dashed lines. (a) The innermost magnetic shield made of a Niobium basket inside a cryoperm basket on the sample stage of the dilution refrigerator. The inset on the top right shows a top view of the sample stage with a sample inside the magnetic shield basket. (b) Intermediate magnetic shield made of layers of lead, mu-metal, and aluminium that wraps around the entire sample stage. (c) Outermost magnetic shield made of aluminium foil wrapping the entire still can. (d) Schematic representation of all the magnetic shielding in the dilution refrigerator, not to scale.

predict shielding factors of the order of $10^3$ for vertical magnetic fields and $10^1$ for horizontal magnetic fields. In order to improve these factors, we must either use more layers of magnetic shielding or, preferably, use deeper magnetic shields with no openings except on the top.

Ideally speaking, we require a shielding factor such that any external magnetic fields generate flux signals lower than the noise floor of the SQUID ($S_{\phi\phi}$) (see Section 4.3).

## Particle motion detection

In the following, we describe the methods by which the motion of the levitated particle has been measured, that is, optically and via inductive coupling to a DC-SQUID magnetometer.

Optical detection was used initially as an unequivocal way to prove that the particle levitates. However, optical detection of a levitated superconducting particle has two considerable drawbacks. First, the spatial resolution is limited to that of the microscope used for imaging which will be diffraction limited at best, with an ultimate resolution of half the wavelength of the light used for imaging. One can use interferometric schemes to detect the particle displacements to achieve much better spatial resolutions, but then we run into the second drawback.

The superconducting particle will absorb any light with photon energy larger than the superconducting gap, which is in the frequency range between microwaves and infrared ($1 \times 10^{12}$ Hz). Any light more energetic than that will break Cooper pairs in the particle, which will slowly become normal conducting and fall down.

Thus, optical detection with a microscope is not well suited for precise particle displacement detection, and interferometric measurements are well suited only for fast measurements because of the properties of the particle changing during the measurement.

Inductive coupling of the particle to a DC-SQUID magnetometer is a non-destructive way to measure the particle position. Because the particle motion disturbs the magnetic field of the trap, it generates changes in the magnetic flux around it. Coupling this magnetic flux to a DC-SQUID magnetometer allows for the detection of displacements that generate flux changes as low as the noise floor of the magnetometer, provided no other sources of magnetic flux are present.

### Optical detection

To detect the particle motion via optical means, we made use of a lens and a mirror which were held on top of the magnetic trap inside the cryostat. The lens was used to collect the image of the surface of the bottom chip, where the particle is sitting during the cool-down. The collimated beam with the image of the particle inside the trap is reflected by a tilted mirror towards a set of windows on the vacuum cans of the cryostat.

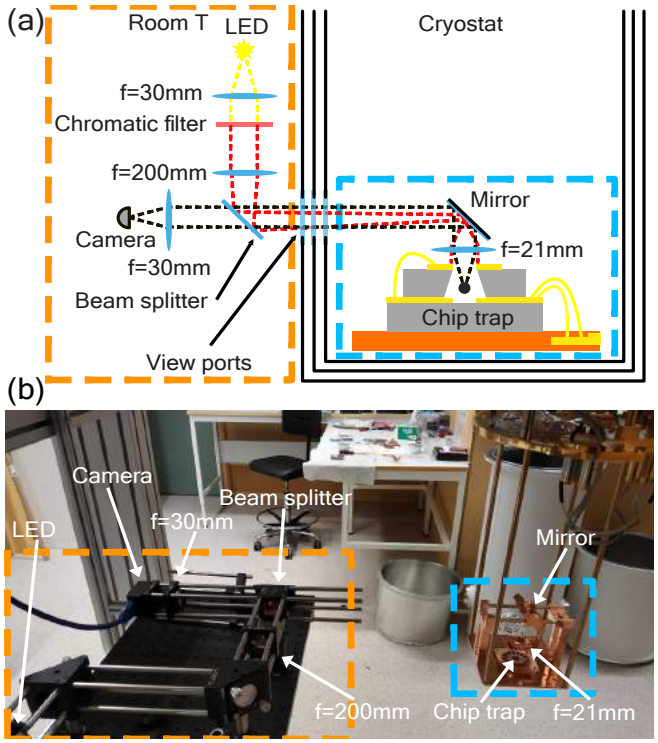


**Figure 3.20:** (a) Schematic of the optical detection setup, showing both the illumination and imaging paths of the light in red and black, respectively. Drawing not to scale. (b) Picture of the setup with the cryostat open.

Outside the cryostat, the collimated light is focused on a CMOS camera by an additional lens. To illuminate the particle, we used a white LED whose light is first collimated by a lens and then focused on the back focal plane of the lens inside the cryostat. This illumination scheme, known as Köhler illumination, creates a collimated light beam that illuminates the sample evenly over the field of view [115]. The complete setup is illustrated in Fig. 3.20. In this way,

we could record videos of the particle lifting off and levitating.

With a tracking algorithm, we could use the frames of the videos to track the center of the particle and study the particle motion, provided that the amplitude of the motion was large enough to be resolved by the microscope (our microscope's resolution was about 2 µm). This was done after recording the videos because the tracking algorithm was not fast enough to track the particle in real time.

### SQUID-based detection

When levitating, the particle oscillates around the levitation point, which is slightly below the point with the least magnetic field intensity due to gravity. As the particle moves, it perturbs the magnetic field distribution inside the trap due to magnetic field expulsion from within the particle. This field perturbation changes the magnetic flux through the pick-up loops inside the trap (Fig. 3.23(b)), which in turn will induce a current in the pick-up loops.

By connecting these pick-up loops to the input coil of a DC-SQUID magnetometer, we can transport the flux induced by the particle motion to the SQUID sensor. These loops are wire-bonded to niobium pads on the sample holder, and a twisted wire pair of enamel-coated 100 µm diameter Nb cables connects the sample holder pads to the SQUID input coil (Fig. 3.21). In this way, the voltage output of the SQUID sensor is directly proportional to the flux induced by the particle in the pick-up loops and is given by

$$V_{\text{out}}^{\text{FLL}} = \phi_{\text{Pick-up}} \frac{R_{\text{F}} M_{\text{input}}}{M_{\text{Finput}}(L_{\text{Pick-up}} + L_{\text{Parasitic}} + L_{\text{input}} + L_{\text{F}_{\text{in}}})}, \tag{3.10}$$

where $R_{\text{F}}$ and $L_{\text{F}}$ are the resistance and inductance of the feedback circuit, respectively, $M_{\text{input}}$ is the mutual inductance between the SQUID input inductance $L_{\text{input}}$ and the SQUID, $L_{\text{Pick-up}}$ is the inductance of the pick-up loop, $L_{\text{parasitic}}$ is the parasitic inductance of the wire-bonds and twisted cable pairs between the pick-up loop and the SQUID, $L_{\text{Finput}}$ is the inductance of the flux transfer circuit that is coupled to the feedback circuit, $M_{\text{Finput}}$ is the mutual

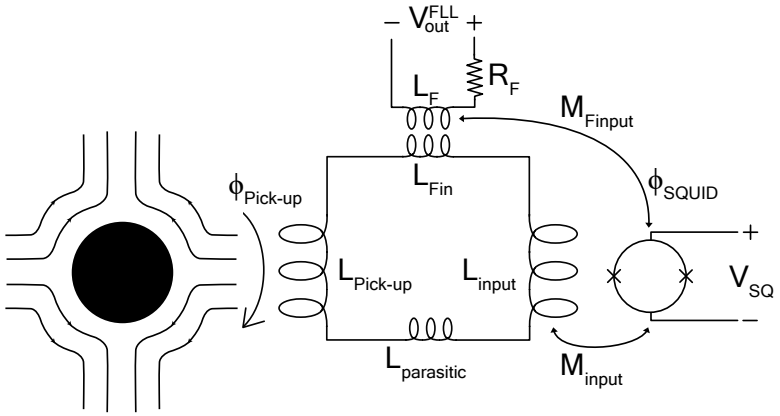


**Figure 3.21:** Circuit equivalent of the electronics used for the SQUID detection of the levitated particle.

inductance between the $L_{\mathrm{F}}$ and the SQUID, and $\phi_{\text{Pick-up}}$ is the magnetic flux threading the pick-up loop.

$L_{\text{Pick-up}}$ can either be simulated or calculated as [116]

$$L_{\text{Pick-up}} = \mu_0 R(\log(16R/w) - 2 + \log(4) + 2\pi\lambda^2/wt), \tag{3.11}$$

where $\mu_0$ is the magnetic permeability of the vacuum, $R$ is the inner radius of the loop, and $w$ and $t$ are its width and thickness.

$L_{\text{Parasitic}}$ of the twisted Nb wire can be calculated as [117]

$$L_{\text{Parasitic}} = \frac{\mu_0 l}{120} \ln\left(\frac{2s}{d}\right), \tag{3.12}$$

where $s$ is the separation between the center of the twisted wires, $d$ is the diameter of the wire conductor, and $l$ is the length of the twisted wire pair.

Another important magnitude is how much of $\phi_{\text{Pick}-\text{up}}$ is transported to the SQUID. This magnitude is called flux transfer efficiency $\eta_{\text{flux}}$ and is given by the ratio

$$\eta_{\text{flux}} = \frac{\phi_{\text{SQUID}}}{\phi_{\text{Pick-up}}} = \frac{M_{\text{input}}}{L_{\text{input}} + L_{\text{Parasitic}} + L_{\text{Pick-up}} + L_{\text{F}_{\text{in}}}}. \tag{3.13}$$

It is important to note that while the SQUID magnetometer is sensitive to particle displacements, it does not measure the displacement of the levitated particle, but rather, it measures the magnetic flux caused by the particle displacement.

Assuming that the smallest possible signal one can measure is twice as large as the noise floor of the sensor, then it is not possible to detect particle displacements that produce flux signals with an amplitude lower than twice the intrinsic noise floor of the SQUID, which is $S_{\phi\phi} \sim 1\,\mu\phi_0\text{Hz}^{-0.5}$ for the sensors in our setup. For the pick-up loops in our devices, the magnetic flux per unit of particle displacement is estimated to be $\eta = 10\,\text{m}\phi_0\mu\text{m}^{-1}$, and the flux transfer efficiency $\eta_{\text{flux}} = 3.1 \cdot 10^{-2}$ (see supplemental material in Paper C). If we were limited by the noise floor of the sensor, the smallest detectable particle displacement in our setup would be $2S_{\phi\phi}/(\eta\eta_{\text{flux}})$ =6.4 nm $\text{Hz}^{-0.5}$.

## Particle motion control via feedback

Feedback control is a widely used technique in the field of systems control. In a system controlled via feedback, the signal to control (the state of the system) is compared to the desired reference signal (the desired state of the signal) and the discrepancy is used to compute a corrective action (feedback) that will bring the system to the desired state.

Typically, the output of a sensor measuring the state of an oscillator (what we want to control) is fed to a device that computes a feedback signal. The feedback signal is then fed to an actuator that will influence the state of the resonator. The equation of motion of an oscillator under feedback is

$$m\left(\ddot{x} + \gamma_0\dot{x} + \omega_0^2 x\right) = F_{\text{fl}} + F_{\text{fb}} + F_{\text{ba}}, \tag{3.14}$$

where $m$ is the mass of the oscillator, $\gamma_0$ is the damping, $\omega_0$ is the resonance

frequency, $F_{\mathrm{fl}}$ is the fluctuation force driving the oscillator, $F_{\mathrm{fb}}$ is the feedback force and $F_{\mathrm{ba}}$ is the back-action force coming from the coupling between the oscillator and the measurement device. In the following, we will neglect $F_{\mathrm{ba}}$ due to it being negligible compared to $F_{\mathrm{fb}}$ and $F_{\mathrm{fl}}$ in our experiments.

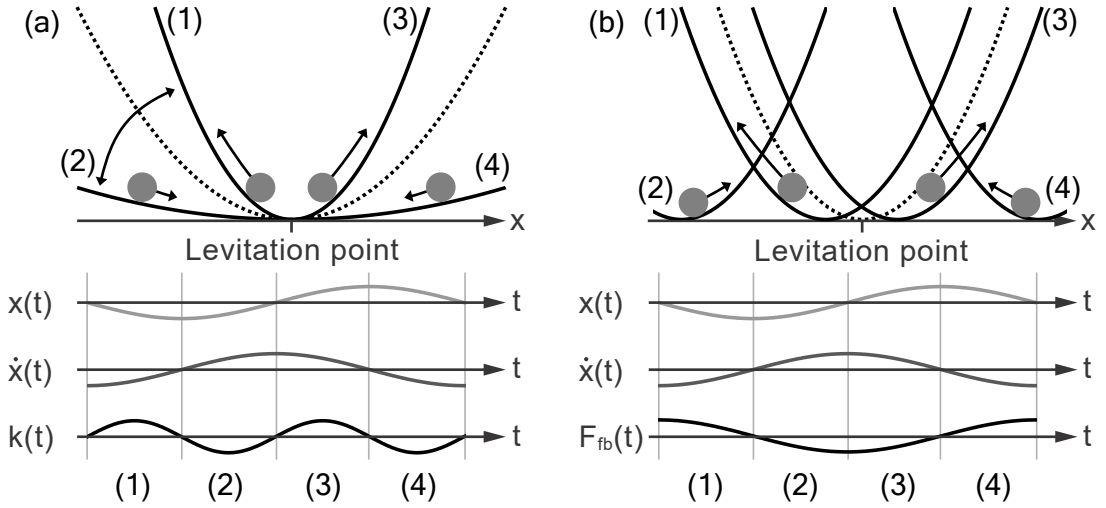


**Figure 3.22:** Schematic representations of (a) parametric and (b) direct feedback cooling of a levitated particle for a single oscillation cycle. Figures adapted from [118]. The figures show how the potential landscape of the particle in the trap changes over time. The oscillation cycle is divided into four parts, the particle moving away and toward the levitation point from the left (1,2) and from the right (3,4). The dashed line shows the potential well when there is no feedback.

In general terms, the feedback applied to a system can be classified into two categories, depending on how the corrective action is applied. If the stiffness of the potential well is modulated with a frequency $2\omega_0$ the feedback is called parametric [Fig. 3.22(a)], and the motion of the oscillator is given by

$$m\left\{\ddot{x} + \gamma_0\dot{x} + \omega_0^2 x\left[1 - G\sin 2(\omega_0 t + \theta_{\mathrm{fb}})\right]\right\} = F_{\mathrm{fl}}, \tag{3.15}$$

where $G$ is a constant, commonly referred to as gain, that determines the extent to which the potential is modulated, and $\theta_{\mathrm{fb}}$ is the phase difference between the feedback and the oscillator position $x$.

If a force directly proportional to the velocity $\dot{x}$ of the resonator is applied,

the feedback is called direct [Fig. 3.22(b)], and the equation of motion is given by

$$m\left(\ddot{x}+\gamma_0\dot{x}+\omega_0^2 x\right)=F_{\mathrm{fl}}+m\left\{\gamma_{\mathrm{fb}}\left[\dot{x}(\omega_0 t+\theta_{\mathrm{fb}})+\delta\dot{x}(\omega_0 t+\theta_{\mathrm{fb}})\right]\right\}, \quad (3.16)$$

where $\gamma_{\mathrm{fb}}$ is the damping due to feedback and $\delta\dot{x}$ is the noise in the feedback signal.

In either case, whether the feedback will heat or cool the motion of the oscillator depends on the phase $\theta_{\mathrm{fb}}$. A phase difference $\theta_{\mathrm{fb}}=-\frac{\pi}{2}$ will cool the motion [Fig. 3.22(b)], while $\theta_{\mathrm{fb}}=\frac{\pi}{2}$ will heat it. This is illustrated in Fig. 3.23.

For parametric feedback cooling [Fig. 3.23(a)], the potential well is stiffened when the particle is moving away from the levitation point and loosened when it is moving towards it. This will prevent the particle from building up momentum (velocity).

For direct feedback cooling [Fig. 3.23(b)], a force proportional to $-\dot{x}$ is applied to the particle, which effectively moves around the potential well by shifting the trap minimum without changing the stiffness of the trap. Similarly, this has the effect of preventing the particle from building up momentum (velocity).

In the following, we will restrict ourselves to direct feedback, which is the method used in the experiments in this thesis. Assuming that $F_{\mathrm{fl}}$ in the system under feedback is a thermal force $F_{\mathrm{th}}$ that is a normally distributed random force with mean zero and variance $\sqrt{2mk_BT\gamma_0^2}$, where $k_B$ is the Boltzmann constant, and that the feedback to the system is direct, the steady state temperature $T_s$ of the oscillator is given by [119]

$$T_s=T\frac{\gamma_0}{\gamma_0+\gamma_{\mathrm{fb}}}+\frac{m\omega_0^2}{4k_B}\frac{\gamma_{\mathrm{fb}}^2}{\gamma_0+\gamma_{\mathrm{fb}}}S_{x_nx_n}, \quad (3.17)$$

where $T$ is the temperature of the environment, $\gamma_{\mathrm{fb}}$ is the feedback rate, and $S_{x_nx_n}$ is the detection noise spectral density, that is, the noise floor of the

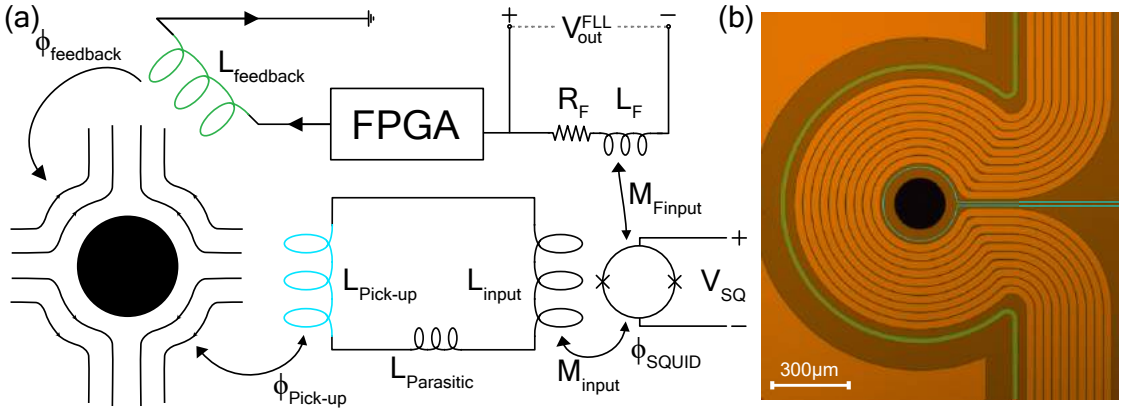


**Figure 3.23:** (a) Schematic representation of the feedback circuit used in the experiments. The SQUID is assumed to be operated in FLL. (b) Colored optical microscope picture of the top chip, showing the trap coil (orange), the pickup coil (cyan), and the feedback coil (green) as colored in (a).

detector used to measure $x$ in $\mathrm{m^2\,Hz^{-1}}$.

Minimizing $T_s$ with respect to $\gamma_{\mathrm{fb}}$ one obtains the optimal feedback rate

$$\gamma_{\mathrm{fb}}^{\mathrm{opt}} = \sqrt{\frac{4\gamma_0 k_B T}{m\omega_0^2 S_{x_n x_n}} + \gamma_0^2} - \gamma_0, \tag{3.18}$$

which for small $\gamma_0$ can be approximated to

$$\gamma_{\mathrm{fb}}^{\mathrm{opt}} = \sqrt{\frac{4\gamma_0 k_B T}{m\omega_0^2 S_{x_n x_n}}}. \tag{3.19}$$

Substituting Eq. (3.19) in Eq. (3.17) we obtain the minimum achievable temperature

$$T_{s_{\mathrm{min}}} = T\gamma_0 \frac{(1 + \omega_0^4 S_{x_n x_n}^2)}{\gamma_0 + 2\sqrt{\frac{k_B T \omega_0^2 S_{x_n x_n} \gamma_0}{m}}}. \tag{3.20}$$

Neglecting the second term of the numerator and the first term of the denominator, we obtain the more commonly used expression [120]

$$T_{s_{\min}} = \sqrt{\frac{4m\omega_0^2\gamma_0 S_{x_n x_n} T}{k_B}}. \tag{3.21}$$

In the experiments in this thesis, the signal to control is the measured particle displacement, the desired state is a particle displacement as small as possible (i.e., minimum motional amplitude), and the feedback is an additional magnetic force on the particle.

We have implemented a feedback circuit that allows us to control the motion of the particle via superconducting coils on the chip traps. A schematic of the implementation is shown in Fig. 3.23(a). The output of the locked SQUID magnetometer ($V_{\text{out}}^{\text{FLL}}$), which contains the information on the particle displacement, is sent to a Field Programmable Gate Array (FPGA, in our case a Red Pitaya). The FPGA filters the signal with a band-pass filter centered at the particle resonance $\omega_0$, shifts the phase of the filtered signal by $\theta_{\text{fb}}$, and sends the resulting signal as a current to the feedback coil on the chip. Depending on the value of $\theta_{\text{fb}}$ the feedback will either increase or decrease the amplitude of motion.

# CHAPTER 4

# Results

In this section, we summarize the main results of this thesis. The first levitation experiments were conducted at 4 K with planar superconducting coils as magnetic traps. Initially, we were under the impression that a planar coil should be able to trap a superconducting particle. While that is technically true, we failed to account for the effect of adhesion forces, which the magnetic forces generated by planar traps cannot overcome. The particles used for these experiments were made of niobium or YBCO (Yttrium Barium Copper Oxide). Their large critical temperatures and critical fields ensure that they remained superconducting no matter their location on the trap coil.

After failing to stably levitate particles with such devices, two-chip magnetic traps were devised and the first levitation of superconducting particles was observed. At this point in time, the experiments moved into a dilution refrigerator and a python program was developed to track the particle motion

with video recordings of the particle motion. This was definite proof of the viability of the chip-based approach to magnetically levitate superconducting microparticles.

The following experiments focused on detecting the particle motion via inductive coupling to a superconducting coil with a DC-SQUID magnetometer. The SQUID measurements gave a much more complete picture of the particle motion because (i) it could measure the motion in all directions, and (ii) it was much more sensitive than the microscope. The drawback was that we did not get a direct measurement of the particle displacement, but rather of the magnetic flux generated by the displacement. Furthermore, we observed clear signs of nonlinear particle motion. The nonlinear behavior originated from the large amplitudes of motion due to the mechanical coupling of the motion of the particle to the mechanical vibrations of the cryostat, generated by the pulse tube.

To convert the flux signal of the SQUID into particle displacement, we had to understand whether the particle motion was nonlinear or whether our detection scheme with inductively coupled superconducting loops was responsible for a nonlinear conversion of particle displacement to SQUID flux. It turned out to be both. Later experiments focused on mitigating the nonlinearities by reducing the amplitude of the particle motion, with the idea that for sufficiently low amplitudes the nonlinearities would become negligible. This has been done by decoupling the particle motion from vibrations in the cryostat using cryogenic vibration isolation. This has allowed us to measure the free evolution of the particle motion and perform ringdown measurements, which give mechanical quality factors of up to $10^5$. The quality factor is much lower than what would be expected for a levitated superconductor in the Meisser state. In order to find the origin behind the low $Q$ values, we make estimates of the dissipation in the system due to the expected loss mechanisms.

## 4.1 First attempts at magnetic levitation with planar traps

In the very first experiments, we used the planar traps shown in Fig. 3.7 to levitate superconducting microparticles. We used niobium or YBCO microparticles from powders, as they were the materials with the largest critical fields (0.4 T and exceeding 100 T, respectively [107], [121]). We obtained powders with particle sizes ranging from a few µm to several hundred µm.

We placed the particles on top of the planar coils and cooled them down to 4.5 K inside an attoDRY800 cryostat. During cooldown, we monitored the particle with a custom-made optical microscope through windows in the cryostat chamber and lenses and mirrors inside and outside the cryostat (see Section 3.3).

Despite the many iterations of planar trap designs, the particles could only be moved by turning on the current in the coil and applying a mechanical excitation with a piezoelectric transducer (see Fig. 4.1) glued to the sample holder with BF-6 glue. The coils alone were not able to move the particles.

After many attempts and almost as many planar trap designs, we concluded that the magnetic force generated by a planar coil on the particle (of the order of 100 pN) was not strong enough to overcome the adhesive forces between a microparticle and the substrate. The adhesive forces (see Section 2.4) are in fact dominant in such microscopic systems, being of the order of 100 nN, overcoming both the weight of the particle (around 10 pN) and the magnetic force of the trap by orders of magnitude.

Since this simple approach was not working, we had to take a step back to think about different trap architectures. We concluded that for the magnetic force of the trap to overcome the adhesive force between particle and substrate, we would have to make non-planar, i.e. three-dimensional devices.

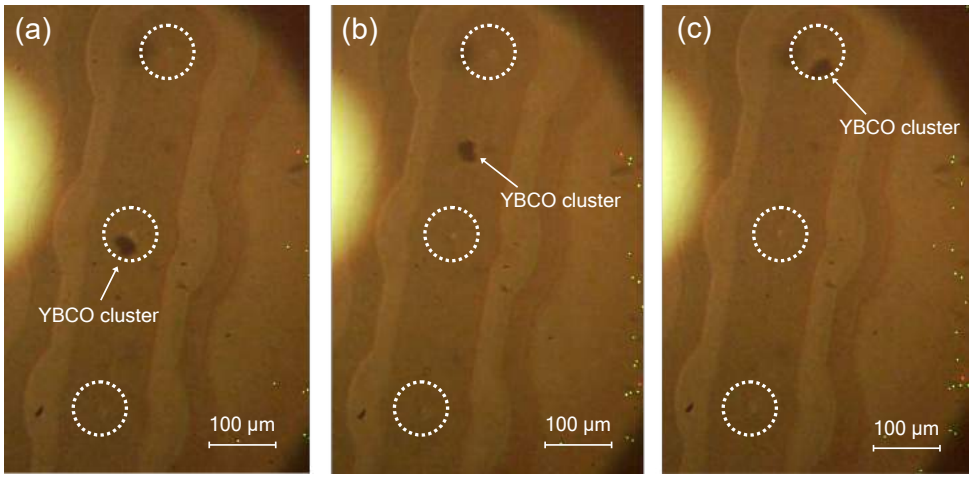


**Figure 4.1:** Microscope pictures of a planar trap with a YBCO cluster in one of the trap sites (circles). When the trap is on, and we shake the sample with a piezoelectric transducer, the particles slide from one trapping site to another, but they do not levitate. The trapping sites are the areas within the dashed lines.

## 4.2 Chip-based magnetic levitation of superconducting microspheres at mK temperatures

After a few iterations of design and simulation, we found that a two-chip stack architecture with planar superconducting coils on the top of both chips was capable of stable levitation while also being able to overcome the adhesion force between the particle and the substrate. We developed a fabrication process to be able to produce such traps, and then we put it to the test in the same way as we did for the planar traps.

To demonstrate beyond reasonable doubt that a superconducting microparticle was levitating inside our chip trap, we used direct optical detection by means of a microscope. The custom-made optical microscope allowed us to look at the chip trap inside the cryostat to observe the particle lifting off the ground and oscillating around the levitation point when the current in the chip trap is turned on. The first levitation events were recorded in the attoDRY800 cryostat, but the vast majority of the experiments were performed

in a BlueFors LD250 dilution refrigerator, which was installed in the laboratory by this point in time. Thus, levitation was first demonstrated at 4.5 K and then at 50 mK.

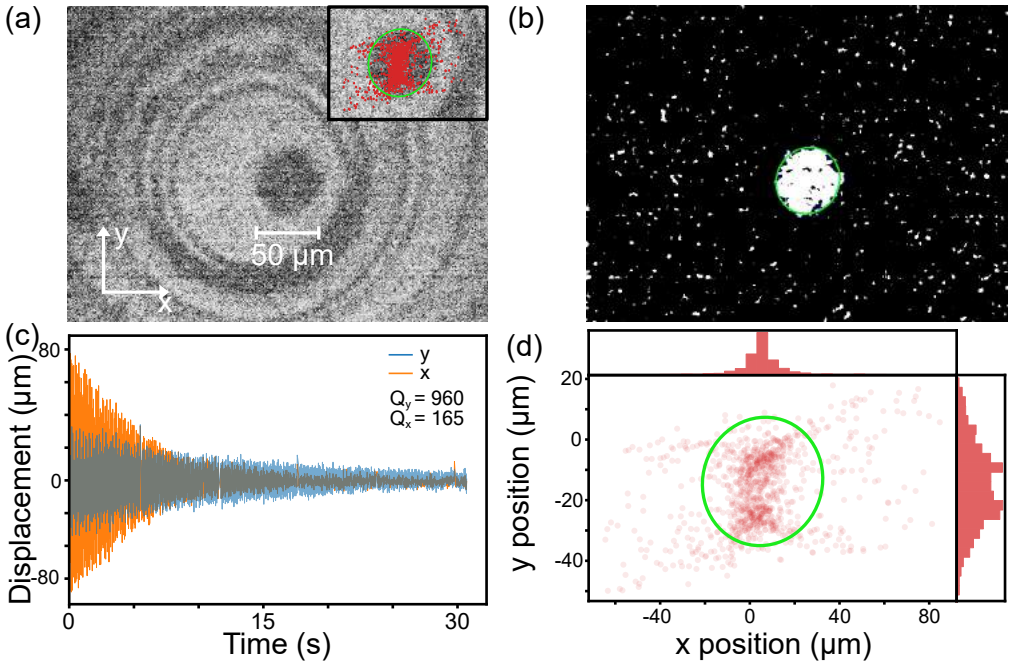


**Figure 4.2:** (a) Top view of the levitating particle (black circle) inside the magnetic trap. The concentric circles are the top and bottom coils and the hole in the top chip. The inset in the top right shows the fitted particle contour in green and the particle positions (red) measured over the duration of the video. (b) Particle contour (green) resulting from processing (a) with a particle tracking algorithm that fits an ellipse (green) to the perimeter of the particle. (c) Ringdown of the particle motion in the x and y directions. (d) Density plot of the measured particle positions in the trap, where the origin of the coordinate system is the center of the frame in (a) and the green contour is the one shown in (b).

To track the center-of-mass motion of the particle, we recorded videos of the levitating particle with a high-speed 600 Hz camera (see videos here [122]), which is more than twice as fast as the largest trap frequency expected from our FEM model. We processed the videos with a python program that fits the contour of the particle for each frame.

We should also mention that the vertical motion (which we call $z$) cannot be resolved by the microscope, which has a resolution of above 2 µm. The

particle moving in the vertical direction makes it go in and out of the focal plane, changing the observed particle radius. However, the depth of field of the microscope was significantly larger than the COM amplitude in the vertical direction, so the changes in radius could not be resolved.

We note that we never found higher harmonics of $\omega_x$ and $\omega_y$ in the optical tracking data, which we did find when detecting the particle motion with a SQUID. This is most likely due to the sensitivity of each detection method. Since the microscope is rather close to the amplitude of the fundamental modes in the steady state, we do not expect it to be able to resolve higher order modes because they are expected to have lower amplitudes (see Section 2.5).

An example of a recorded frame and a fitted particle contour is shown in Fig. 4.2(a) and (b). The center of the ellipse is taken as the center of the particle.

When we turn on the current in the trap, the particle jumps from the bottom chip to the levitation point (see the videos in [122]). For that to happen, enough energy (in the form of work done by the magnetic trap) must be provided to the particle to overcome the potential barrier of the adhesion force with the substrate (Section 2.4). This energy, plus the potential energy difference between the particle at the starting position and at the levitation point, is converted to mechanical energy. As a consequence, the oscillation amplitude of the particle when it starts levitating is large enough that it can be resolved by the microscope's camera.

This is shown in Fig. 4.2(c), where the particle displacement over 30 s is shown, and a typical ringdown curve is observed. At the end of the time trace, the particle falls because light absorption destroys superconductivity in the particle. This process can take between a few seconds and tens of seconds, depending on the illumination power. We think this is the case because if we do not use light, the particle levitates for days, and we can still see it when we turn the light back on. Also, the particle falls faster the more illumination power is used. However, we never tried to optimize this setup as it was a means to demonstrate levitation, but not the detection method we wanted to measure the particle motion.

The measured quality factors under illumination are of the order of $10^2$.

These values are rather low, and it is not clear why. A possible explanation is that the light absorbed by the particle creates large amounts of quasi-particles. As the particles move within the magnetic trap, the changing magnetic field generates a dissipative quasi-particle current in the particle, which would dampen the motion. But again, we never looked into this phenomenon in detail because it was unrelated to the aim of the project.

Fig. 4.2(d) shows a density plot of the measured particle positions within the frame over the same time trace. For early times i.e., large amplitudes, the plot is reminiscent of a Lissajous curve, which shows the motion of two harmonic oscillators in two dimensions. As time passes, the amplitude of motion decreases and the measured positions accumulate at the center of the trap.

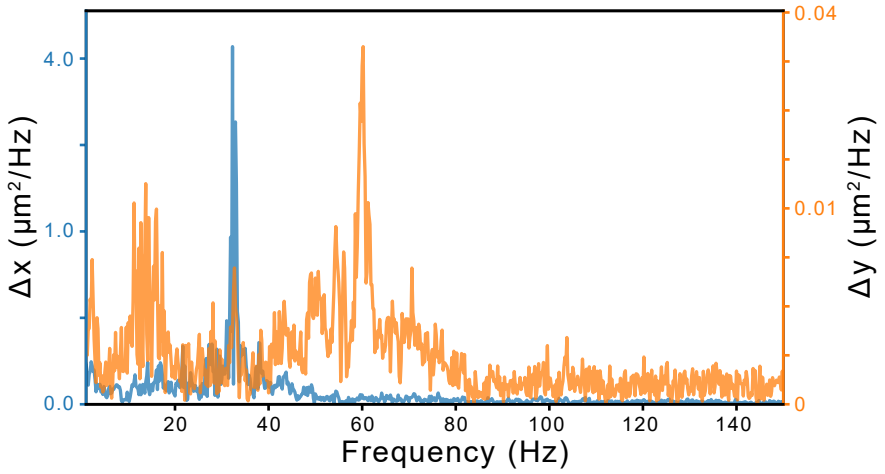


**Figure 4.3:** Power spectra of the x and y motion of the particle in blue and orange, respectively.

The power spectra of the particle motion in $x$ and $y$ are obtained from time traces of the COM motion of the particle, such as the ones shown in Fig. 4.2(c). In Fig. 4.3 we see the resonance peaks of the particle in $x$ and $y$ (not $z$). Note that the amplitude of the motion in $x$ is ten times larger than in $y$. This is because the coil openings, which are aligned with the $x$ direction, are the parts of the trap coil that provide the weakest magnetic field confinement. This makes the particle confinement in the direction of the openings weaker and the oscillation frequency lower.

Optically detecting the particle motion allowed us (i) to demonstrate that the two-chip magnetic traps were working, (ii) to confirm that the trap frequencies were in the expected range of 10 to 100 Hz for the in-plane frequencies, and it showed that (iii) the particle motion had to be measured without illumination if we wanted the particle to levitate for extended periods of time. These results have been published in Paper B.

## 4.3 Nonlinear motion of the levitated particle

In order to detect the particle motion without the illumination destroying superconductivity, we have used a superconducting coil within the magnetic trap [see Fig. 3.23(b)] to transport the magnetic flux generated by the particle motion to a DC-SQUID magnetometer. We use the knowledge of the geometry of the coils in the chip trap to calibrate the voltage output of the SQUID to magnetic flux, as described in Section 3.3.

A typical time trace of the SQUID signal is shown as the gray trace of Fig. 4.4(a). In order to identify the trap frequencies, we calculate the power spectrum of the SQUID time trace and analyze the peaks. We can check which of the peaks in the spectrum are trap frequencies by changing the current in the trap. The COM frequencies of a superconducting sphere levitated in an ideal magnetic quadrupole field are given by [102]

$$\omega_i = \zeta_i \frac{\mu_0 N I}{R^2} \sqrt{\frac{3}{2\mu_0 \rho}}, \tag{4.1}$$

where $\mu_0$ is the vacuum permeability, $I$ is the trap current, $N$ is the number of trap coil windings, $R$ is the trap coil inner radius, $\rho$ is the particle's density and $\zeta$ is a geometric factor. At the center of an ideal anti-Helmholtz configuration $2\zeta_x = 2\zeta_y = \zeta_z = 0.86$. In our chip trap, $\zeta_x = 0.04$, $\zeta_y = 0.06$ and $\zeta_z = 0.12$.

Thus, a change in the trap current should cause a proportional change in the trap frequencies, shown in Fig. 4.5.

Once the trap frequencies are identified, the recorded SQUID signal is post-

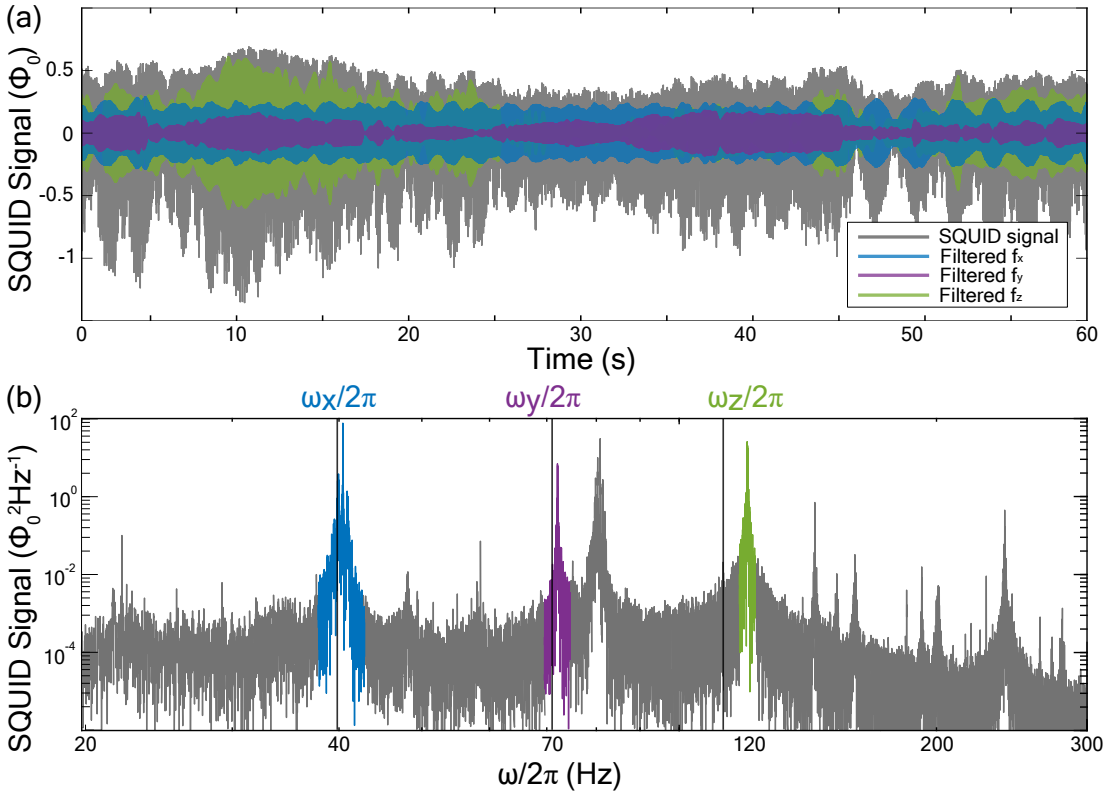


**Figure 4.4:** (a) Time trace of the SQUID magnetometer calibrated to flux quanta. The gray curve shows the output of the SQUID electronics, and the colored curves show the same data filtered around the particle trap frequencies. (b) Power spectrum of the curves in (a), where the vertical lines show the frequencies predicted by FEM simulations (taken from Paper C).

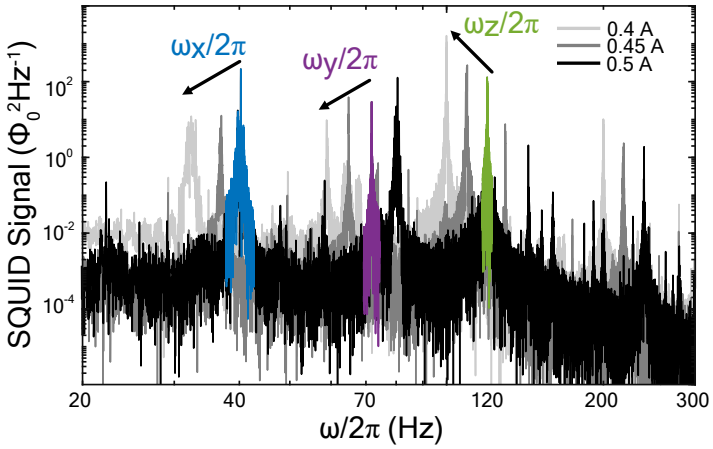


**Figure 4.5:** Spectra of three SQUID time traces for different currents running in the chip trap. The black curve shows the same power spectrum as Fig. 4.4(b) with the fundamental frequencies colored in the same way, and the lighter curves show the trap frequencies decreasing for descending trap currents.

processed with band-pass filters (one for each trap frequency) that allow us to see the translational modes of the particle. These filtered signals are shown as colored traces in Fig. 4.4(a).

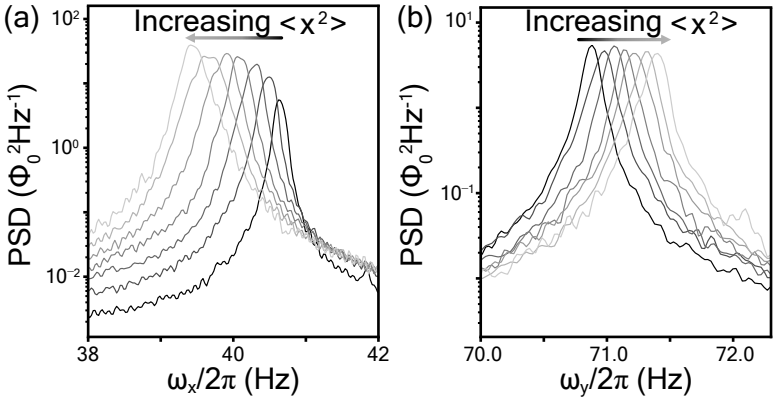


**Figure 4.6:** Frequency shift in (a) $\omega_x$ and (b) $\omega_y$ due to changes in the x-mode amplitude, exemplifying mode nonlinearities and mode coupling in the modes of the levitated particle, respectively (taken from Paper C).

Note that the amplitude of the motion in $x$, $y$, and $z$ (Fig. 4.4(a)) is changing randomly over time. These changes in amplitude are due to vibrations in the cryostat generated by the pulse tube propagating all the way to the

chip trap, which results in a non-thermal fluctuation force driving the motion of the particle. As a result, the amplitude of motion of the particle becomes quite large (several micrometers) relative to the thermally driven motion corresponding to the sample temperature (10 pm for 50 mK). Because our chip trap is asymmetric, it produces a potential landscape with anharmonicities that contribute to the potential energy up to a few percent for a 24 µm radius particle with amplitudes of µm (see Fig. 4.7). Therefore, the trap can only be considered to be harmonic for motional amplitudes such that the energy of the nonlinear terms in the mode $i$ is much smaller than that of the harmonic term ($\alpha r_i^3, \beta r_i^4 \ll \omega^2 r_i^2$, see Section 2.5). For the parameters of the $z$ motion in our system ($\alpha_z = 3.6 \times 10^{-2}$ µN kg$^{-1}$ µm$^{-2}$ and $\beta = 10$ µN kg$^{-1}$ µm$^{-3}$) the motional amplitudes below which the cubic and quartic nonlinearities negligible are 13.5 µm and 0.2 nm, respectively.

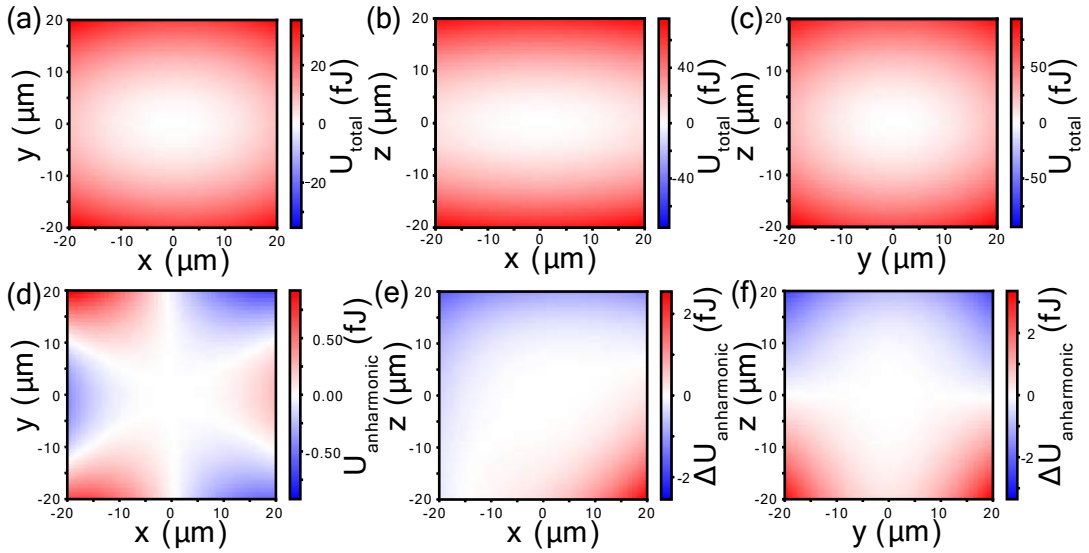


**Figure 4.7:** Model of the potential energy landscape of a 48 $\mu$m diameter particle in the chip trap. (a-c) 2D slices of the total potential energy landscape of the particle in the trap. (d-f) Anharmonic contributions to the potential energy landscape (adapted from Paper C).

Because the particle motion is large (several µm), it reaches the regions of the potential landscape where the anharmonic components are not negligible, which causes it to display nonlinear behavior such as amplitude-dependent frequency shifts and mode coupling (see Section 2.5 and Section 2.5). Both phenomena are discussed in detail and shown to be well described by our

model of the trap in Paper C. Examples of both nonlinear motion and mode coupling are shown in Fig. 4.6 (a) and (b) respectively. In these measurements, the amplitudes of the $y$ and $z$ motion are small and $\omega_x$ and $\omega_y$ are measured for increasing $x$ amplitude. The frequencies are being pulled for larger $x$ amplitudes in accordance to the theory in Section 2.5 and Section 2.5.

## 4.4 Nonlinear detection of the levitated particle

We have seen that the magnetic trap stiffness is nonlinear for large particle amplitudes. Similarly, the amount of magnetic flux induced in the pick-up loops has a nonlinear dependence on the particle position. In Fig. 4.8 (a) we show a COMSOL simulation of the back action field of the particle when levitated in a magnetic quadrupole field. We integrate the magnetic flux in the pick-up loops to find the pick-up efficiency $\eta$ as a function of the particle position. Because the pick-up loops in our chip trap are connected in series, the flux induced in the two pick-up loops adds up.

The flux response has a linear and a quadratic component with respect to particle displacements in all directions, but only the response to displacement along $z$ is predominantly linear. The nonlinearity in the detection doesn't cause any issues beyond giving many peaks for higher harmonics of the modes, especially for $x$, which is shown in detail in Paper C. Similarly to the anharmonicities in the trap potential, motional amplitudes of sub-µm would make the quadratic nonlinearity in the pick-up efficiency negligible as well, provided that the equilibrium point for $x$ and $y$ is shifted away from the regions with high curvature, which is the case in our system ($x_{\mathrm{eq}} = -21\,\mu\mathrm{m}$ and $y_{\mathrm{eq}} = 3.3\,\mu\mathrm{m}$).

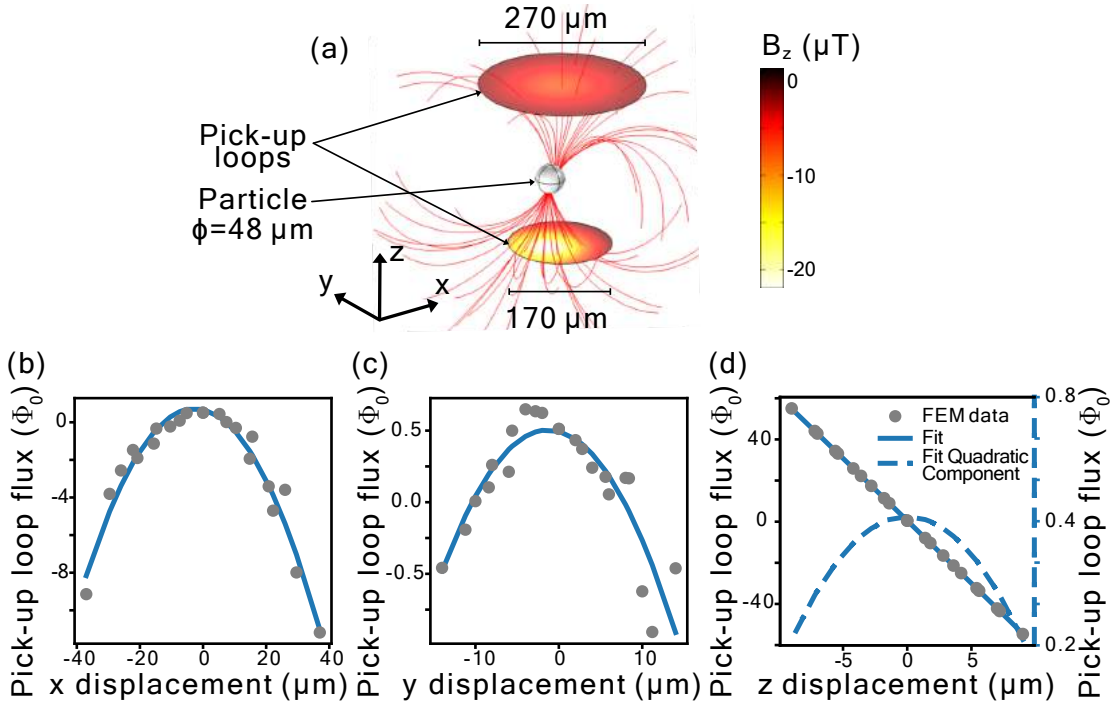


**Figure 4.8:** (a) FEM simulation of the back action field of a superconducting sphere inside a magnetic quadrupole trap between two pick-up loops. The field lines are shown as red lines, and the vertical component of the magnetic field is potted in the areas contained within the pick-up loops. Magnetic flux in the top and bottom loops induced by the particle displacement in the (b) $x$, (c) $y$, and (d) $z$ directions (taken from Paper C).

## 4.5 Towards linear motion with cryogenic vibration isolation

Ultimately, we want to decrease the amplitude of the particle motion, and to do that we need to isolate the experiment from vibrations coming from the cryostat and the laboratory. To isolate the sample from vibrations, we have implemented a simple elastic pendulum setup in the dilution refrigerator, from which the experimental stage hangs (see Fig. 4.9). The sample stage is also attached to the mixing stage of the cryostat with un-braided copper strands to thermalize the sample to mK temperatures. The copper strands have been annealed at 800 °C in an argon atmosphere to soften the copper, which weakens the mechanical link between the sample and mixing stages while keeping the thermal link. Lead particles were levitated in the same chip trap, with the same amount of magnetic isolation. The only difference between the two measurements, other than the vibration isolation, is the radius of the particles (24 µm and 31 µm for rigid and isolated, respectively) and that a three times longer Nb twisted wire pair had to be used to connect the SQUID to the sample when using vibration isolation.

The vibration isolation has reduced the noise floor of the SQUID signal $S_{\phi_0\phi_0}$ from $54\mathrm{m}\phi_0\mathrm{Hz}^{-0.5}$ to $3.1\mathrm{m}\phi_0\mathrm{Hz}^{-0.5}$. In principle, there is no reason why reducing vibrations would reduce the magnetic noise. However, a coil moving within an inhomogeneous magnetic field will see an oscillating magnetic field. If this contributes to the magnetic noise, one should expect a reduction of the amplitude of the motion to decrease the magnetic flux noise as well. The decrease of the flux noise floor (24.6 dB) is rather similar to the decrease in the amplitude of the particle motion $z$ motion [37.5 dB, see Fig. 4.10(a)]. In this calculation, we have accounted for the larger parasitic inductance that comes from using longer twisted wire pairs to reach the sample from the SQUID sensor when using the vibration isolation stage. Both estimates are relatively close to both the expected and measured (at room temperature) mechanical attenuation of the vibration isolation stage(approximately 50 dB). The estimated attenuation for each case is rather close, which is a good indication that it originates from the vibration isolation.

Interestingly, the $\omega_x$ peak hasn't been found after the experiment has been

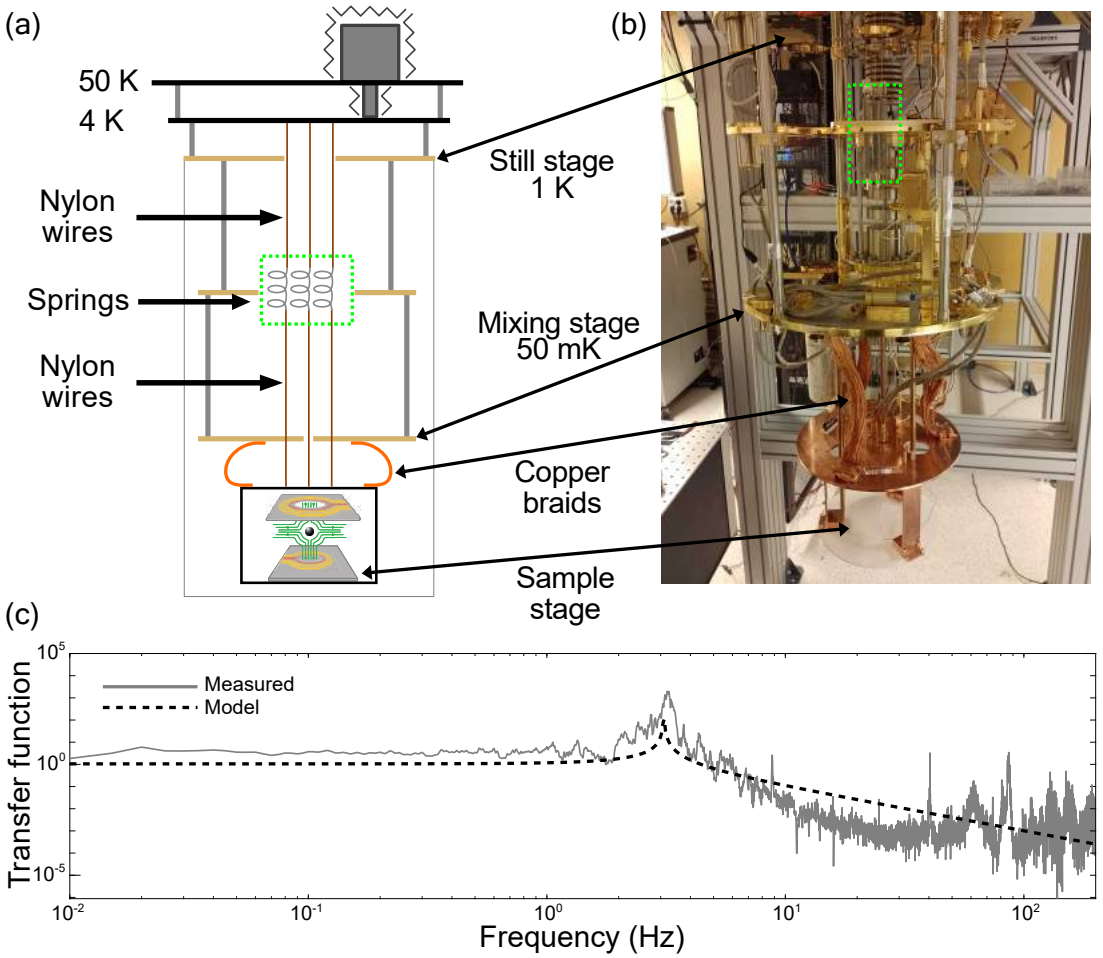


**Figure 4.9:** (a) Schematic representation and (b) picture of the sample stage with vibration isolation, which is hanging from three elastic pendula attached to the 4 K stage for mechanical isolation, as well as from unbraided copper braids attached to the mixing stage for thermalization. (c) The transfer function of the vertical displacement for the vibration isolation stage with respect to the 4 K stage is measured with a geophone in gray and predicted by the model in a dashed black line.

isolated from vibrations. We can calculate the smallest detectable amplitude for any given mode by multiplying the smallest detectable magnetic flux ($S_{\phi_n\phi_n}$ in $\phi_0 \mathrm{Hz}^{-0.5}$) (see Section 3.3) by the square toot of its linewidth $\gamma$ and dividing it by its pick-up efficiency $\eta$, which becomes

$$r_i = \frac{\sqrt{\gamma_i}}{\eta_i} S_{\phi_n\phi_n}. \tag{4.2}$$

Note that we do not account for $\eta_{\mathrm{flux}}$ here because the data we are using for this calculation is given in flux at the pick-up loop, not at the SQUID.

With the pick-up efficiency for the $x$ motion $\eta_x = 50\mathrm{m}\phi_0\mu\mathrm{m}^{-1}$ and assuming a similar quality factor to the $y$ mode of $5 \cdot 10^4$ we obtain the smallest detectable displacement in $x$ motion $r_x$ =4.5 µm. For the rigid stage, we can obtain the $x$ amplitude by integrating the peak area and converting it to meters dividing it by $\eta_x\eta_{\mathrm{flux}}$ to obtain an $x$ amplitude of 22.8 µm, which differs from $r_x$ by 14 dB. Thus, if we consider a similar decrease in amplitude for the $x$ motion as for the $z$ motion (37.5 dB), it is expected that the $x$ signal would be below the noise floor.

Similarly, we can calculate the amplitude of the $y$ mode for the rigid and isolated setups and obtain amplitudes of 12.6 µm and 0.1 µm, respectively, which give an attenuation of 41 dB, still within the expected range. We would expect the attenuation in $x$ and $y$ to be similar, because of the pendulum symmetry, which would suggest an $x$ amplitude of 0.2 µm, well below the noise floor for the $x$ motion ($r_x$ =4.5 µm).

Further evidence that the vibration isolation works as intended is that it has allowed us to observe ring-downs of the $\omega_z$ and $\omega_y$ modes for the first time, shown in Fig. 4.10(b). These measurements have given the most reliable estimate of the quality factor yet, and indicate that the role of the amplitude fluctuations on particle motion due to cryostat vibrations has decreased.

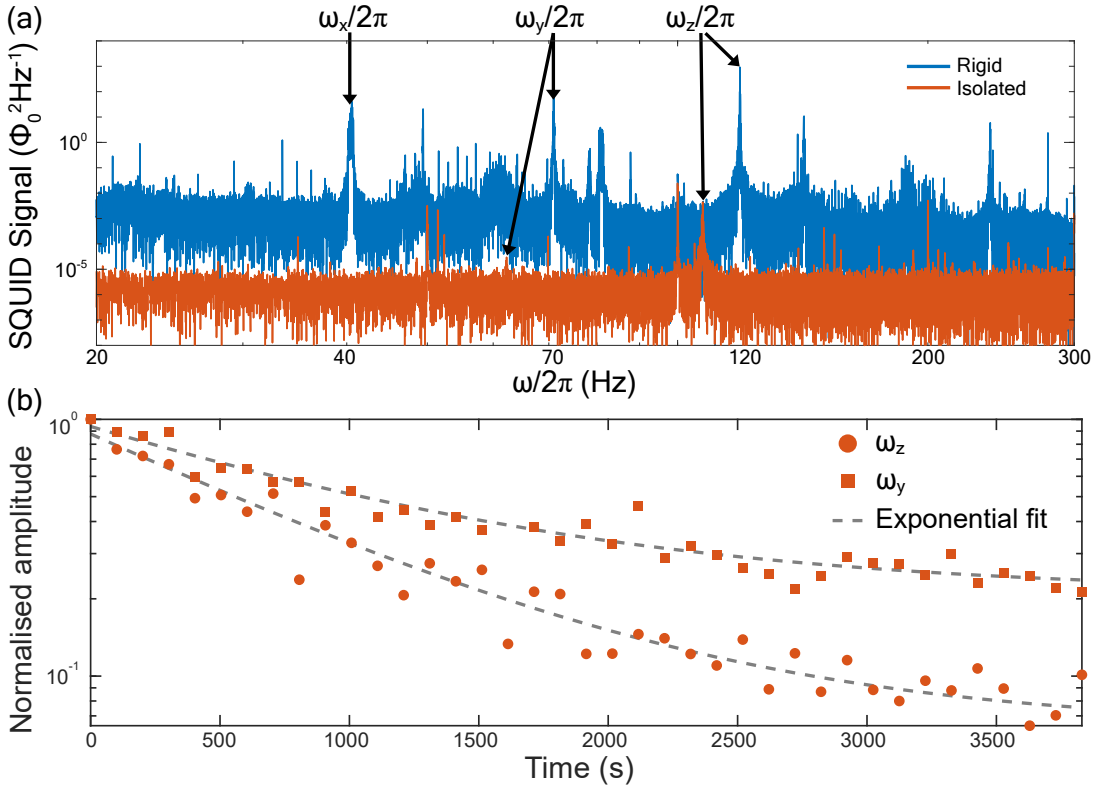


**Figure 4.10:** (a) Effect of vibration isolation in the SQUID signal, showing a decrease in the noise floor as well as in the particle motional amplitude when comparing a 24 µm radius sphere levitated on a setup rigidly attached to the mixing stage and a 31 µm radius sphere levitated on the vibration isolated stage, using the same magnetic trap. Note that the $\omega_x$ peak is not found in the measurement with a vibration-isolated stage. (b) Ring-down measurements of the $\omega_y$ and $\omega_z$ peaks of the 31 µm radius sphere levitated on the vibration isolated stage.

## 4.6 Feedback control of the COM motion

To further decrease the amplitude of motion of the particle, we intend to use feedback to cool the COM motion [36], [54], [68], [119], [120] with the aim of cooling the mechanical mode to the ground state in future experiments [28], [29], [32], [33]. Using the SQUID measurement of the particle displacement, feedback electronics, and further coils in our chip trap, we can demonstrate the feasibility of controlling the particle motion via feedback with superconducting coils on the chip (see Section 3.3). To provide feedback to the levitated particle, we send the SQUID signal to an FPGA (Red Pitaya) which filters it with a band-pass filter around the $\omega_z$ mode and generates a phase-shifted version of the filtered signal. The phase-shifted signal is attenuated by $-30\,\mathrm{dB}$ and sent back to one of the superconducting coils on the chip trap.

We have attempted both parametric and direct feedback. Unfortunately, in our attempts at parametric feedback, no significant heating or cooling was observed.

Direct feedback did prove effective, but with a considerable caveat. Because when we apply direct feedback in our setup, the SQUID sensor sees both the signal of the particle and that of the feedback (at the same frequency), the particle signal and feedback signal could not be separated. Thus, to identify the effect of the feedback, we had to send feedback for a few seconds and after that measure the amplitude of motion. We repeated this process for different phase shifts until the appropriate phase shifts for cooling and heating were found. Fig. 4.11 shows time traces of the SQUID signal after one minute of feedback heating (red) and cooling (blue) as well as when no feedback (yellow) has been applied. The amplitude of motion changed significantly for the heating, and slightly for cooling, as well as there being a frequency shift due to the nonlinearities in the trap [Fig. 4.11(b)]. Note that these experiments were performed before the installation of the vibration isolation.

Why the cooling wasn't very effective isn't clear, but a likely explanation is that the mechanical vibrations that randomly drive the particle and excite its motion also change its phase, which makes the feedback cooling more ineffective over time.

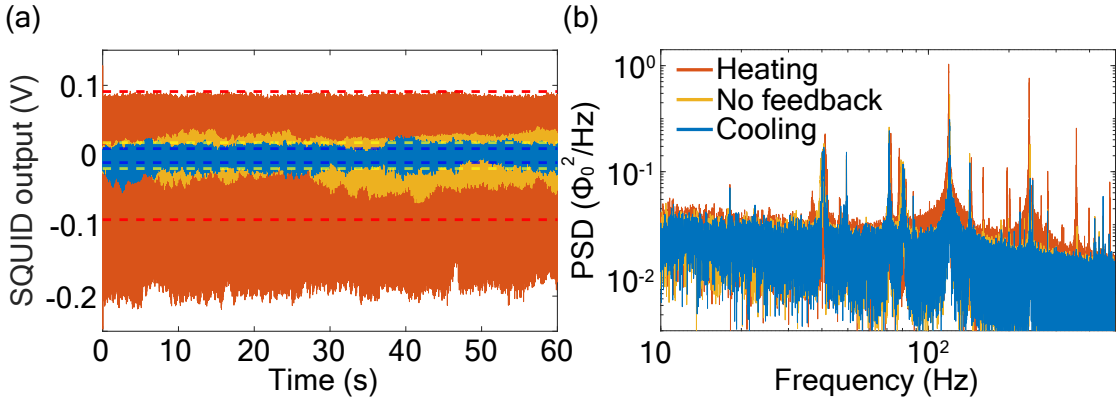


**Figure 4.11:** (a) Amplitude of the SQUID signal when the COM motion of the levitated particle in the z direction is heated, provided no feedback, and when it is cooled. (b) The corresponding power spectra of the time traces in (a), showing the difference in peak height and the frequency shifts, caused by nonlinearities of the magnetic trap and coupling between the modes.

Thus, we showed that we can control the particle motion with coils on the chips. However, in order to do so effectively, the particle needs to be decoupled from mechanical vibrations in the cryostat and the magnetic flux noise must be decreased to effectively cool the motion.

## 4.7 Dissipation mechanisms

The levitated particles in our experiments have shown mechanical quality factors between $10^3 - 10^5$. These values are far from the upper bound predicted for levitated superconductors, as they have been shown to have mechanical quality factors up to $10^7$ [71] and are expected to reach quality factors of the order of $10^8 - 10^9$ [34], [41]. In the following, we make estimates of the dissipation due to eddy current damping and gas collisions. We argue that these mechanisms do not explain the quality factors measured in our experiments, and we discuss the possibility of surface-induced dissipation.

## Eddy current dissipation

There are two ways in which a superconductor levitated in a magnetic field can generate eddy currents. First, simply by moving in the magnetic field, the magnetic field expulsion of the particle will generate an oscillating magnetic flux in the surrounding space that will induce eddy currents in any nearby conductors. Second, if the particle traps flux, the motion of the particle will be equivalent to a moving magnetic dipole moment, which will also induce eddy currents.

### Eddy currents due to field expulsion

We will start the estimation by assuming that a superconducting particle is levitating within a quadrupole magnetic field, and it is also levitating above a square block of copper of side $a = 1.4\,\mathrm{cm}$ and thickness $h = 5\,\mathrm{mm}$ (which is our sample holder, see Fig. 3.13), which is a distance $d = 414\,\mu\mathrm{m}$ away from the levitation point ($300\,\mu\mathrm{m}$ from the silicon substrate thickness and $114\,\mu\mathrm{m}$ from the levitation height). The motion of the magnetic particle perturbs the magnetic field of the trap due to field expulsion, and thus, generates an oscillating magnetic flux. We estimate the amplitude of this flux by using Equation 11 from [123]

$$\phi(z) = \frac{48 I \mu_0 \pi}{25\sqrt{5} R_{\mathrm{trap}}^2} \times \left[ \frac{d R_{\mathrm{p}}^5 R_{\mathrm{pu}}^2}{\left(d^2 + R_{\mathrm{pu}}^2\right)^{\frac{5}{2}}} + z \left( \frac{R_{\mathrm{p}}^5 R_{\mathrm{pu}}^2 \left(-4d^2 + R_{\mathrm{pu}}^2\right)}{\left(d^2 + R_{\mathrm{pu}}^2\right)^{\frac{7}{2}}} - \frac{R_{\mathrm{p}}^3 R_{\mathrm{pu}}^2}{\left(d^2 + R_{\mathrm{pu}}^2\right)^{\frac{3}{2}}} \right) \right], \tag{4.3}$$

where $I$ is the current in the magnetic trap (assuming that an anti-Helmholtz coil generates the quadrupole field that is the magnetic trap), $R_{\mathrm{trap}}$ is the inner radius of the trap coil, $R_{\mathrm{p}}$ is the radius of the levitated particle, and $R_{\mathrm{pu}}$ is the radius of the loop (which we call pickup loop) within which the magnetic flux is calculated. Henceforth, we will assume that the copper block is circular, with the radius of the block being the circumscribed circle within

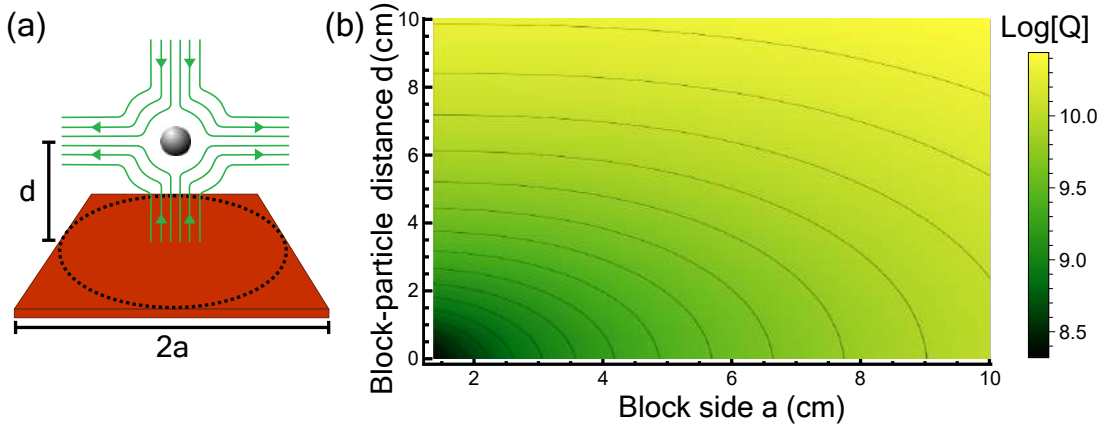


**Figure 4.12:** (a) Schematic representation of a particle levitated in a quadrupole field above a copper block, within which the oscillating magnetic flux is calculated. (b) Quality factor due to eddy current damping for a piece of copper with an increasingly large lateral dimension $l$ and distance $d$ for a given thickness $h = 5\,\mathrm{mm}$.

the square block $R_{\mathrm{pu}} = a$ [see Fig. 4.12(a)].

Eq. (4.3) gives the magnetic flux within a loop as a function of particle displacement assuming the loop is concentric with the levitating particle, and at a vertical distance $d$ from the same particle. Taking the derivative with respect to particle displacement from the trap center in the vertical direction $z$ gives

$$\delta\phi = \delta z \frac{48 I \mu_0 \pi}{25\sqrt{5} R_{\mathrm{trap}}^2} \left[ \frac{R_{\mathrm{p}}^5 a^2 \left(-4d^2 + a^2\right)}{\left(d^2 + a^2\right)^{\frac{7}{2}}} - \frac{R_{\mathrm{p}}^3 a^2}{\left(d^2 + a^2\right)^{\frac{3}{2}}} \right]. \tag{4.4}$$

This change of magnetic flux will induce eddy currents in the copper sample holder below the particle. These eddy currents will run around the center of the copper piece (assuming that's where the particle levitates). The induced voltage driving these currents can be calculated using the induction law (Eq. (4.5)), using $\delta t = 2\pi/\omega$

$$\Delta V = \frac{\delta\phi}{\delta t} = \delta\phi \frac{\omega}{2\pi} = \delta\phi f. \tag{4.5}$$

Then, the dissipated power is $P_{\text{diss}} = \Delta V^2/R$, with $R$ being the resistance experienced by the eddy current. The resistance of an infinitesimally thin disk (using cylindrical coordinates) is

$$R = \rho_{\text{Cu}} 2\pi a/(\delta a \delta h), \tag{4.6}$$

where $\rho_{Cu}$ is the resistivity of copper (at cryogenic temperatures), $a$ is the radius of the disk and $h$ is the thickness of the disk. Thus, the volume integral of $\Delta V^2/R$ in cylindrical coordinates can be calculated as a surface integral over the radius and thickness of an infinitesimally thin and narrow disk:

$$P_{\text{diss}} = \int_V \frac{(\delta\phi f)^2}{R} dV = \frac{1}{2\pi} \int_0^{l/2} da \int_d^{d+t} dh \frac{(\delta\phi f)^2}{\rho_{Cu} a}. \tag{4.7}$$

The mechanical energy of the levitated particle is $E_m = m\omega^2 \delta x^2$, and so the dissipation rate of the eddy currents becomes

$$\gamma = P_{\text{diss}}/E_m, \tag{4.8}$$

which for the values in our setup (Table 4.1) becomes $2\pi{\cdot}6 \times 10^{-7}\,\text{Hz}$. Note that both $P_{\text{diss}}$ and $E_m$ are proportional to $\delta x^2$, so the dissipation due to eddy currents is not amplitude dependent.

| Parameter | Value |
|---|---|
| $T$ | $50\,\text{mK}$ |
| $\omega$ | $2\pi{\cdot}119\,\text{Hz}$ |
| $\rho_{\text{particle}}$ | $11\,250\,\text{kg}\,\text{m}^{-3}$ |
| $\rho_{\text{Cu}}$ | $1 \times 10^{-8}\,\Omega\,\text{m}$ |
| $I$ | $1.06\,\text{A}$ |
| $R_{\text{trap}}$ | $150\,\mu\text{m}$ |
| $d$ | $414\,\mu\text{m}$ |
| $a$ | $14\,\text{mm}$ |
| $h$ | $5\,\text{mm}$ |

**Table 4.1:** Parameters used for the formulae of our estimates, extracted from our experimental setup.

Similarly, we get an amplitude-independent quality factor

$$Q = \frac{E_m}{E_{diss}} = \frac{E_m \omega}{P_{diss}}, \tag{4.9}$$

which equals $2 \cdot 10^8$ for the values in our experiment (Table 4.1).

The dependence of the eddy current damping on the lateral dimension of the block and the separation between the particle and the top of the copper block is shown in Fig. 4.12(b), where the dimensions of our experiment are in the bottom left corner.

These quality factors are much larger than the ones observed in our experiments. Thus, eddy current damping due to field expulsion does not seem to be the dominant dissipation mechanism.

### Eddy currents due to flux trapping

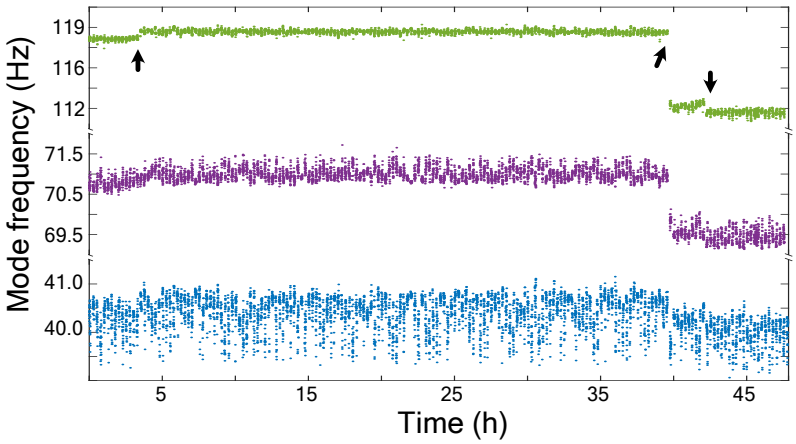


**Figure 4.13:** Particle frequencies measured of a 48 h time period. The arrows indicate the times when discrete frequency jumps occur (taken from paper C).

When measuring the particle motion over extended periods of time, we see discrete jumps in the frequencies of the particle (Fig. 4.13). All the frequencies change (either they all increase or decrease) simultaneously, and the changes seem to occur at random times. It is not clear what is causing these jumps,

but a likely cause would be changing amounts of flux trapped in the particle. The particle would then be able to exchange energy with the environment through the magnetic flux trapped inside it, inducing eddy currents in nearby metals as a moving magnet would, and thus cause dissipation. Assuming that the 24 µm lead spheres trap the entirety of the magnetic field of the earth in their cross-section (no magnetic shielding), the particle would trap

$$\phi_{\text{trapped}} = \vec{B}_{\text{earth}} \cdot \vec{A}_{\text{cross-section}} = N\phi_0, \tag{4.10}$$

where $N = 43$ and $\vec{A}_{\text{cross-section}} = \pi R_{\text{p}}$. We will now consider the levitated particle to have a magnetic moment of

$$\vec{m}_{\text{trapped}} = \{0, 0, \vec{B}_{\text{earth}}\}\frac{1}{\mu_0}\frac{4}{3}\pi R_{\text{p}}^3 = \{0, 0, N\phi_0\}\frac{1}{\mu_0}\frac{4}{3}R_{\text{p}}, \tag{4.11}$$

which we take to point vertically (in $z$) because that will cause the most magnetic flux perpendicular to the copper sample holder surface, and cause the most damping.

Then the magnetic vector potential of this magnetic moment is

$$\vec{A}_{\text{trapped}} = \frac{\mu_0}{4\pi}\frac{\vec{r} \times \vec{m}_{\text{trapped}}}{r^3} = \{y, -x, 0\}\frac{NR_{\text{p}}\phi_0}{3\pi r^3}, \tag{4.12}$$

where $\vec{r} = \{x, y, z\}$ is the position at which $\vec{A}_{\text{trapped}}$ is calculated, and $N$ is the amount of flux quanta. Integrating the magnetic flux in the circle inscribed in the square of the sample holder and taking the derivative with respect to the vertical displacement of the particle, we obtain an equation for the amount of magnetic flux per unit of particle displacement similar to Eq. (4.4),

$$\begin{aligned}\delta\phi_{\text{trapped}} = \frac{\delta}{\delta z}\iint \vec{B}_{\text{trapped}} \cdot d\vec{A}_{\text{sample-holder}} = \\ \frac{\delta}{\delta z}\oint \vec{A}_{\text{trapped}} \cdot d\vec{l}_{\text{sample-holder}} = -\delta z\frac{2N\phi_0 r^2 R_{\text{p}}}{(r^2+z^2)^{5/2}}.\end{aligned} \tag{4.13}$$

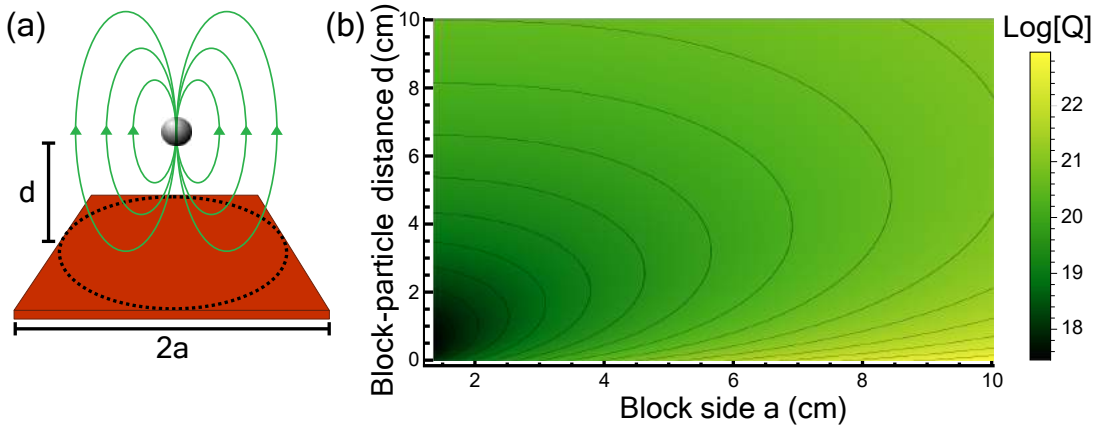


**Figure 4.14:** (a) Schematic representation of the magnetic moment in the levitated particle due to trapped magnetic flux generating an oscillating magnetic field on the sample holder. (b) Quality factor due to eddy current damping caused by the trapped flux in the copper sample holder with an increasingly large lateral dimension $l$ and distance $d$.

We can now perform the same calculation as in Section 4.7 and obtain the quality factor due to the eddy current losses caused by the moving trapped flux. The resulting quality factors for different sample holder shapes are shown in Fig. 4.14(b), for $N = 43$ and a sample holder thickness of 5 mm. The bottom-left corner of the plot shows the Q for the sample holder dimensions used in the experiments, for which we obtain $10^{19}$, which is certainly not a limiting mechanism for the quality factor.

## Gas collisions

Collisions between the levitating particle and the remaining gas molecules inside the cryostat will dampen the motion of the particle by [124]

$$\gamma_{\text{gas}} = \frac{4\pi R_{\text{particle}}^2 P}{m_{\text{particle}} \overline{v}_{\text{gas}}}, \tag{4.14}$$

where $R_{\text{particle}}$ and $m_{\text{particle}}$ are the radius and the mass of the levitated

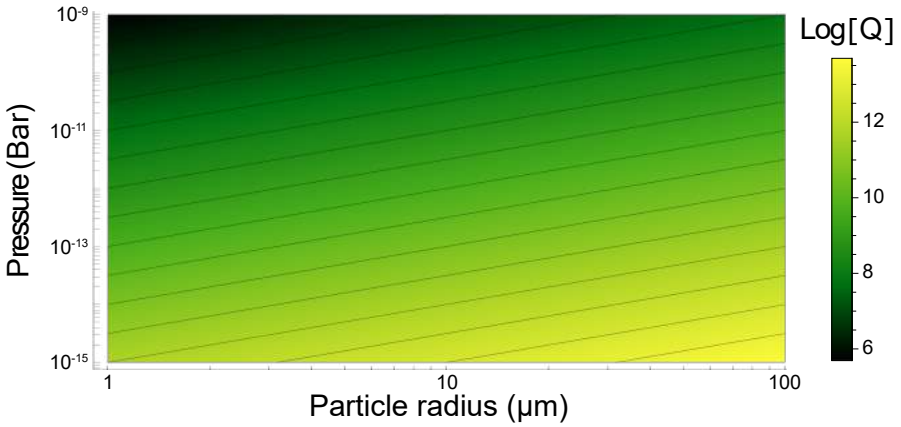


**Figure 4.15:** Quality factor due to gas collisions for a spherical particle at different pressures and particle radii.

particle, $P$ is the pressure in the vacuum chamber, and $\overline{v}_{\text{gas}} = \sqrt{3k_BT/m}$ is the mean velocity of the gas molecules, with $m$ being the mass of one molecule.

In our cryostat, the temperature near the sample ($T_{\text{cold}}$) is 50 mK and the pressure at the pressure gauge ($P_{\text{warm}}$) is $5 \times 10^{-6}$ mbar, which operates at room temperature ($T_{\text{warm}} = 300\,\text{K}$). We know that the pressure $P$ near the particle will be lower than this, because the temperature near the pressure gauge is significantly larger than near the sample, so according to the ideal gas law, the pressure near the sample must be lower as well. Additionally, at cryogenic temperatures gases condense and solidify, further reducing the pressure, which is known as cryopumping. Assuming that the gas near the sample is predominantly helium and that the pressure is very low, we can estimate the temperature near the sample using the Weber-Schmidt model for the thermomolecular effect [125]

$$P_{\text{cold}} = P_{\text{warm}} \sqrt{\frac{T_{\text{cold}}}{T_{\text{warm}}}}, \tag{4.15}$$

which relates the temperatures and pressures within a volume that has a hot and a cold region.

Using $P = P_{\text{cold}}$, and a 24 µm radius lead sphere, the damping rate becomes $\gamma_{\text{gas}} = 2\pi{\cdot}8 \times 10^{-7}$ Hz, which for our working frequency $\omega$ =119 Hz gives a

quality factor of $Q_{\mathrm{gas}} = 10^9$. Thus, the quality factor of the levitated particle is not limited by gas collisions in our system.

### Surface losses

It is necessary to mention that the idea of losses due to magnetic interactions between fluctuating surface magnetization and the levitated particle has recently been proposed [126], although, to my knowledge, there is no published work on tackling this calculation. Admittedly, the levitated particle is rather close to the chip surfaces, even while levitating. If surface defects such as magnetic two-level systems interacted with the particle or with the magnetic trap, it is conceivable that they might cause losses when present in large enough concentrations, even at frequencies of the order of 100 Hz.

## 4.8 Towards ground state cooling

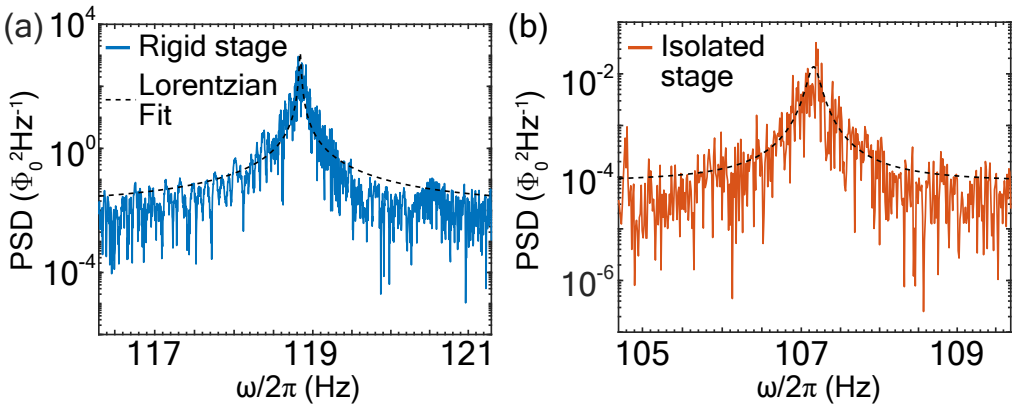


**Figure 4.16:** (a) SQUID signal of a 24 µm radius lead particle levitated on a sample stage that is rigidly fixed to the cryostat. (b) SQUID signal of a 31 µm radius lead particle levitated on a sample stage that is mechanically isolated from the cryostat by an elastic pendulum. The data is taken from Fig. 4.10(a).

Cooling the mechanical motion of the particle to the ground state implies that the root mean square (rms) amplitude of the particle ($x_{\mathrm{rms}} = \sqrt{\langle x^2 \rangle}$) is

similar to the amplitude of the mode when driven by zero-point fluctuations ($x_{\mathrm{zpf}}$). Assuming a harmonic potential for low amplitudes of motion, we can write the mechanical energy as $E_{\mathrm{m}} = (n + 1/2)\,\hbar\omega$, with $n$ being the phonon occupation of the mechanical mode. Thus, we can write the rms amplitude of the particle driven by zero-point fluctuations ($n = 0$) as

$$x_{\mathrm{zpf}} = \sqrt{\frac{\hbar}{m\omega}}, \tag{4.16}$$

where $m$ is the mass of the particle and $\omega$ is the frequency of the mode. For a particle such as the one used in Paper C (24 µm radius and $\rho$ =11 250 kg m$^{-3}$), $m = 6.5 \cdot 10^{-10}$ kg and $\omega = 2\pi{\cdot}119$ Hz in the vertical direction (z). This gives a $x_{\mathrm{zpf}} = 10^{-14}$ m, which has an effective temperature of

$$T_{\mathrm{zpf}} = \frac{\hbar\omega}{k_B} = 5 \cdot 10^{-9}\,\mathrm{K}, \tag{4.17}$$

where $k_B$ is the Boltzmann constant.

Similarly, we can calculate what the thermally driven amplitude of motion ($x_{\mathrm{th}}$) would be when working at $T = 50$ mK. We use the equipartition theorem to establish $E_{\mathrm{m}} = \frac{1}{2}k_B T$, so that we can write

$$x_{\mathrm{th}} = \sqrt{\frac{k_{\mathrm{B}} T}{m\omega^2}}, \tag{4.18}$$

where $k_{\mathrm{B}} = 1.38 \cdot 10^{-23}\,\mathrm{J\,K^{-1}}$, and we obtain $x_{\mathrm{th}} = 6.1 \cdot 10^{-11}$ m.

Using the pick-up efficiency ($\eta$), we can relate the SQUID signal to the particle displacement, and estimate what the $x_{\mathrm{rms}}$ of the particle is for the three translational modes. The average displacement in the $z$ motion for a 24 µm radius lead particle with no vibration isolation is $x_{\mathrm{rms}}^{\mathrm{rigid}} = 9.8 \cdot 10^{-6}$ m (or an effective temperature $T_{\mathrm{eff}} = 2.2 \cdot 10^{9}$K). This is obtained by integrating the area under the peak in Fig. 4.16(a) and using the pickup efficiency ($\eta = 0.6\,\phi_0\mu\mathrm{m}^{-1}$) to convert from flux to displacement (see Paper C).

Similarly, the amplitude for a 31 µm particle levitated using the very same magnetic trap on a vibration isolation system inside the fridge can be ex-

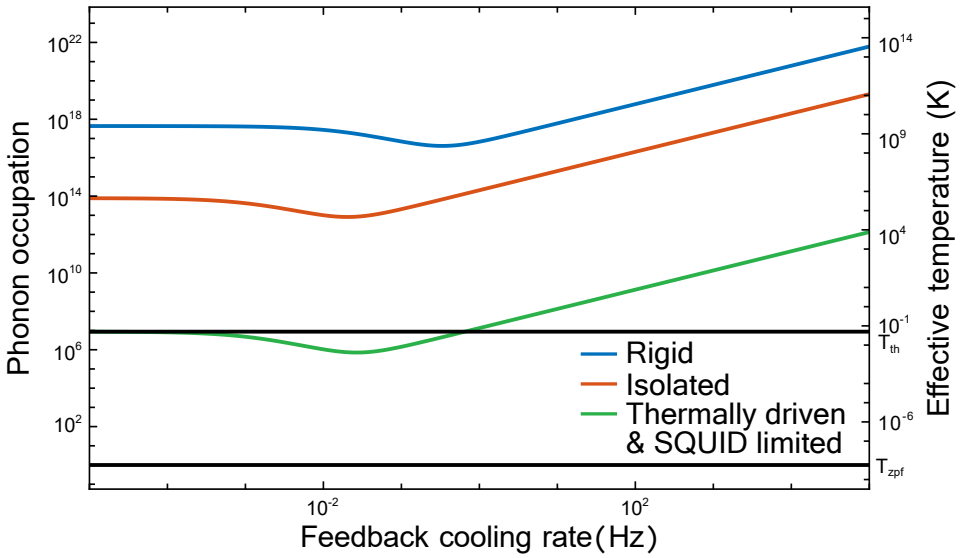


**Figure 4.17:** Phonon occupation and effective temperature of the $z$ COM mode as a function of the feedback cooling rate for the experiment when attached to the fridge rigidly (blue), with vibration isolation (red) and in the hypothetical case of thermally driven COM motion and sensitivity limited by the SQUID noise floor (green). The solid black lines indicate an effective temperature of 50 mK (top) and the effective temperature of the motion when driven by zero-point fluctuations (bottom). The quality factors used for each case are $10^3$ (blue), $10^5$ (red), and $10^7$ (green).

tracted from Fig. 4.16(b). We use this amplitude ($x_{\mathrm{rms}}^{\mathrm{isolated}} = 1.01 \cdot 10^{-7}\mathrm{m}$) to calculate the mechanical energy $E_{\mathrm{m}} = \frac{m}{2}\omega^2 \left(x_{\mathrm{rms}}^{\mathrm{isolated}}\right)^2$ and then calculate the corresponding amplitude for a 24 µm radius particle with the same mechanical energy ($x_{\mathrm{rms}}^{\mathrm{isolated}} = 1.30 \cdot 10^{-7}\mathrm{m}$ and $T_{\mathrm{eff}}^{\mathrm{isolated}} = 4.4 \cdot 10^5\mathrm{K}$). This is done to account for the differences in mass and frequency so that we can make a valid comparison between the two measurements.

To put these numbers into perspective, the ratio between $x_{\mathrm{rms}}^{\mathrm{rigid}}$ and $x_{\mathrm{rms}}^{\mathrm{isolated}}$ is 37.5 dB, and the ratios between $x_{\mathrm{rms}}^{\mathrm{rigid}}$, and $x_{\mathrm{th}}$ and $x_{\mathrm{zpf}}$ are 104 dB and 180 dB, respectively. These numbers indicate the amount of cooling required so that the amplitude of the COM motion of the levitated particle is below the thermally driven motional amplitude and the amplitude of the ground state of motion, respectively.

To find out whether feedback can be used to cool down the particle motion to the ground state, we need to estimate the signal strength of the particle motion and how that compares to the noise floor of the SQUID. We can calculate the signal strength of a certain amplitude of motion on the SQUID as

$$S_{\phi_0\phi_0} = \frac{x_{\mathrm{rms}}\eta\,\eta_{\mathrm{flux}}}{\sqrt{\gamma}}, \tag{4.19}$$

where $\gamma$ is the linewidth of the mode, which is in the order of $2\pi{\cdot}0.1\,\mathrm{Hz}$ for the rigidly attached setup, and $\eta_{\mathrm{flux}} = 3.1\cdot10^{-2}$ is the flux transfer efficiency from the pick-up loop to the SQUID. Thus, we obtain $S_{\phi_0\phi_{0_{\mathrm{th}}}} = 2.5\cdot10^{-6}\phi_0\mathrm{Hz}^{-0.5}$ and $S_{\phi_0\phi_{0_{\mathrm{zpf}}}} = 8.3\cdot10^{-10}\phi_0\mathrm{Hz}^{-0.5}$.

The noise floor of the SQUID in our experimental setup is $S_{\phi_0\phi_0} = 54\cdot10^{-3}\phi_0\mathrm{Hz}^{-0.5}$ and its ultimate limit is $S_{\phi_0\phi_0} = 0.9\cdot10^{-6}\phi_0\mathrm{Hz}^{-0.5}$ at 100 Hz. Neither thermally driven motion nor zero-point fluctuations are detectable via inductive coupling to a SQUID in the rigidly attached setup, and if we reached the noise floor of the SQUID only the thermally driven motion might be detected, but not zero-point fluctuations.

In Fig. 4.17 we show the attainable phonon occupation for the 24 µm lead sphere under direct feedback cooling as a function of the feedback cooling rate, calculated with Eq. (3.17). For these estimates, we used the noise floor and quality factors measured for the rigid and vibration-isolated setups, as well as for the ideal case in which we have thermally driven motion and our detection sensitivity is limited by the noise floor of the SQUID.

In order to reach the ground state, we would have to reduce the magnetic noise in the system by 90 dB to reach the noise floor of the SQUID, and then increase either the pickup efficiency or the quality factor of the mechanical mode to ensure that the signal of the zero-point fluctuations is larger than the noise floor. In the following, we show what steps can be taken in this direction.

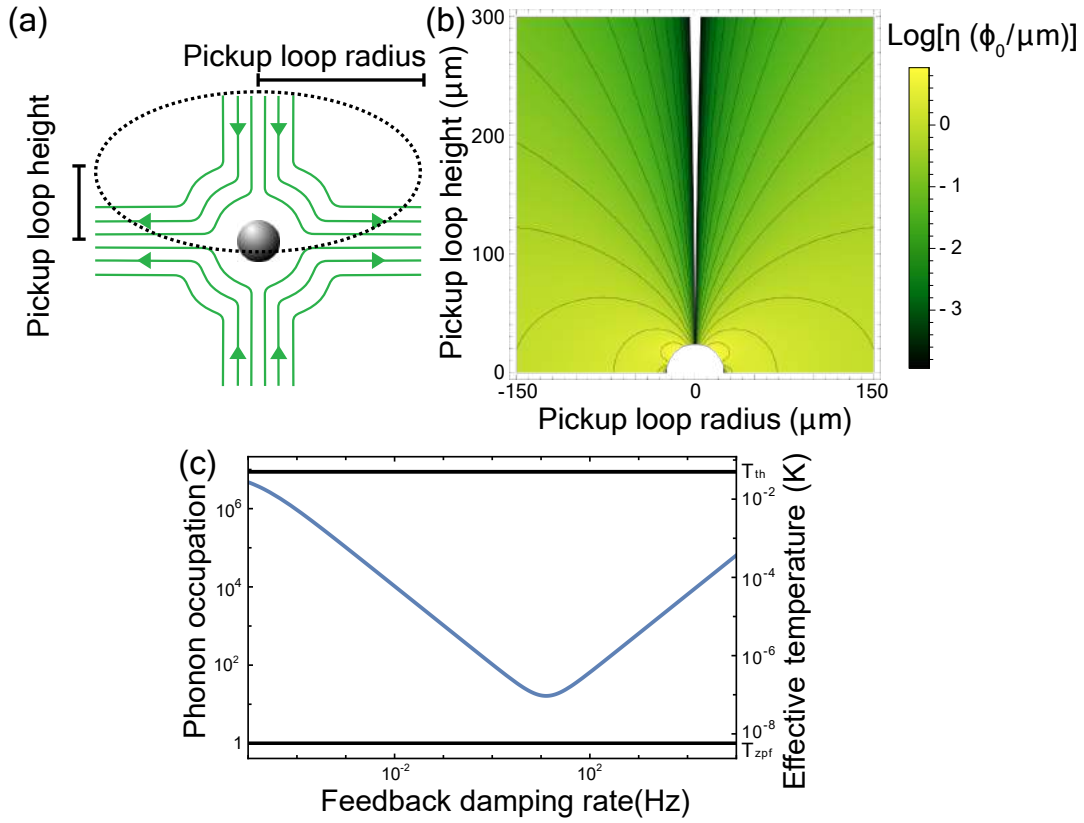


**Figure 4.18:** (a) Schematic representation of a levitated superconducting particle in a quadrupole field, with a pick-up coil concentric with the particle and the field. (b) Surface plot of the pickup efficiency $\eta$ for different pick-up loop radii and vertical separation with the particle. (c) Phonon occupation vs feedback rate using a pick-up coil with 100 windings, with a pitch of 1 µm and an inner radius of 50 µm, to cool down a levitated particle with Q= $10^7$ using a SQUID magnetometer with a sensitivity limited by its intrinsic noise and with the same input inductance as the pick-up loop.

## Increasing the inductive coupling

A possible route that can be taken to cool the particle motion further is to increase the pickup efficiency, $\eta$. The inductive coupling between the particle motion and the pickup loop changes by several orders of magnitude depending on how close the pickup loop is to the particle. If we take the dimensions of our experiments for this estimate (24 µm radius particle), for the case of a pickup loop concentric to the particle we can obtain $\eta$ from Eq. (4.4) as simply

$$\eta = \frac{\delta\phi}{\delta x} = \frac{48 I \mu_0 \pi}{25\sqrt{5} R_{\mathrm{trap}}^2} \left[ \frac{R_{\mathrm{p}}^5 R_{\mathrm{pu}}^2 \left(-4d^2 + R_{\mathrm{pu}}^2\right)}{\left(d^2 + R_{\mathrm{pu}}^2\right)^{\frac{7}{2}}} - \frac{R_{\mathrm{p}}^3 R_{\mathrm{pu}}^2}{\left(d^2 + R_{\mathrm{pu}}^2\right)^{\frac{3}{2}}} \right]. \tag{4.20}$$

Fig. 4.18 shows $\eta$ as a function of the radius of the pickup loop $R_{\mathrm{pu}}$ and the vertical separation between it and the particle $d$. If one could place a pickup loop near the levitation height $d = 0$, with an inner radius of 50 µm and e.g. 100 windings 0.5 µm wide, separated by 0.5 µm, the coil would extend until 150 µm away from the particle center, where $\eta$ is above $1\,\phi_0 \mu\mathrm{m}^{-1}$. This pick-up geometry would result in an effective coupling of $1.7 \cdot 10^2\,\phi_0 \mu\mathrm{m}^{-1}$, which is three orders of magnitude larger than in the current devices.

Such a coil would have a very large inductance, which would dramatically reduce the flux transfer efficiency from the pickup loop to the SQUID (see Eq. (3.13)). For this approach to be viable, we would require a mutual inductance between SQUID and the input circuit of the same order as this pickup loop. A spiral coil with the characteristics mentioned above would have an inductance of 2.1 µH, which could be very efficiently coupled to the commercially available SQUID sensor with the largest input inductance (1.8 µH).

Such a pick-up loop arrangement would be achieved by using a third chip in between the current top and bottom chips that make up the trap, or by fabricating the pick-up loop on top of a spacer layer on top of the bottom chip.

With such a coil arrangement, a SQUID sensor with a well-matched input

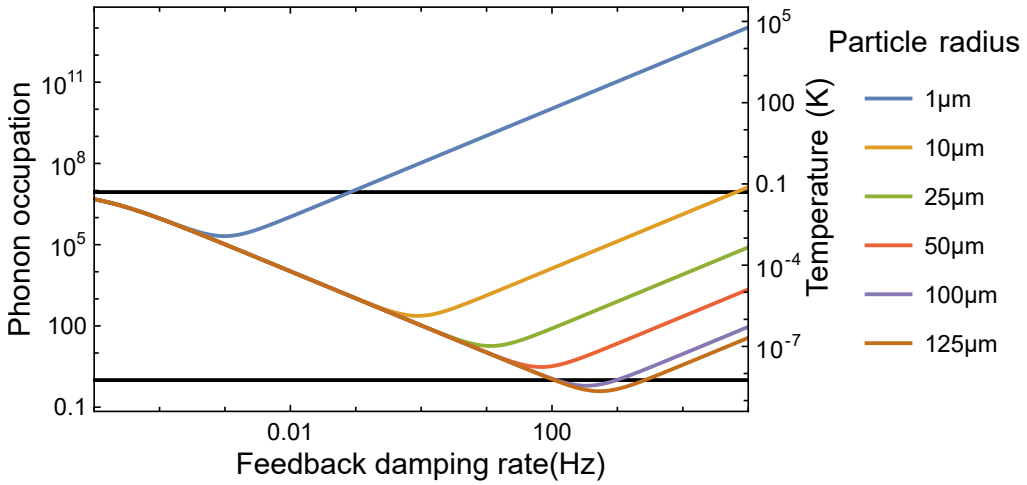


**Figure 4.19:** Effect of the particle size on the phonon occupation vs feedback cooling rate.

inductance, and a mechanical quality factor of $10^7$ such as the one obtained in Ref. [71] for a similar experiment, the COM motion cooled down to a phonon occupation of 16 via direct feedback cooling Fig. 4.18(c).

## The effect of particle size

Several important parameters depend on the particle size, which is a relatively simple parameter to change in the experiment by simply using different particles. If we take look at Eq. (3.21), we will see that the minimum achievable effective temperature for a mechanical mode under direct feedback cooling has the following dependence on the radius of the particle

$$T_{\mathrm{s}_{\mathrm{min}}} = \sqrt{\frac{4m\omega_0^2\gamma_0 S_{\phi_n\phi_n} T}{\eta^2\eta_{\mathrm{flux}}^2 k_B}}. \tag{4.21}$$

The parameters in Eq. (4.21) scale with the particle radius as: $m \propto R_{\mathrm{p}}^3$ and $\eta \propto -R_{\mathrm{p}}^3 + R_{\mathrm{p}}^5$ (see Eq. (4.20)). This dependence means that $T_{\mathrm{s}_{\mathrm{min}}} \propto R_{\mathrm{p}}^{-3/2} + R_{\mathrm{p}}^{-5/2}$, that is, we can reach lower temperatures with larger particles.

The signal-to-noise ratio also scales favorably for larger particle radii. We can take Eq. (4.19), which gives the flux signal of the particle on the SQUID for a given motional amplitude, and divide it by the noise floor of the SQUID

$$SNR = \frac{x_{\mathrm{rms}}\eta\,\eta_{\mathrm{flux}}}{\sqrt{\gamma}S_{\phi_n\phi_n}} = \sqrt{\frac{k_B T}{m\omega^2}}\frac{\eta\eta_{\mathrm{flux}}}{\sqrt{\gamma}}, \tag{4.22}$$

and because of the dependencies of $m$ and $\eta$ on particle radius we obtain $SNR \propto R_{\mathrm{p}}^{3/2} + R_{\mathrm{p}}^{5/2}$, meaning that the larger the radius of the particle the better the signal can be the detected.

However, we must keep in mind that these estimates assume that $Q$ and $\omega$ are unaffected by changes in $R_{\mathrm{p}}$. The latter is a reasonable assumption, since $\omega = \sqrt{k/m}$ and both the trap stiffness and the mass of the particle scale as $R_{\mathrm{p}}^3$. However, whether this holds for $Q$ is not known yet. It seems possible that the quality factor might decrease for larger objects because of a larger amount of interactions with the environment. That said, in Ref. [45] particles with up to 50 µm radius have been shown to have quality factors of $10^7$, so maybe the effect is small enough to be of no concern.

If we assume a pickup loop near the levitation height $d = 0$, with an inner radius of 150 µm and 100 windings each 0.5 µm wide, separated by 0.5 µm, a $Q = 10^7$, a detection noise limited by the SQUID, and that the particle motion is thermally driven we can calculate the achievable temperatures for particles with increasing radius (Fig. 4.19). We can show that, in principle, ground state cooling is achievable for particles of 200 µm diameter or larger with the current magnetic traps, provided that the aforementioned technical improvements can be made.

## Decreasing damping

Because we see evidence of flux trapping in our levitated particles, it is conceivable that the dissipation mechanism limiting the quality factor is trapped flux exchanging energy with the environment. However, this will only happen if (i) the particle is a type II superconductor or (ii) if there are defects in the particle where the flux can be trapped via flux quantization. This first pos-

sibility can be eliminated by levitating type I superconductors (which we do) and the second can be reduced by annealing the microparticles to eliminate crystal defects.

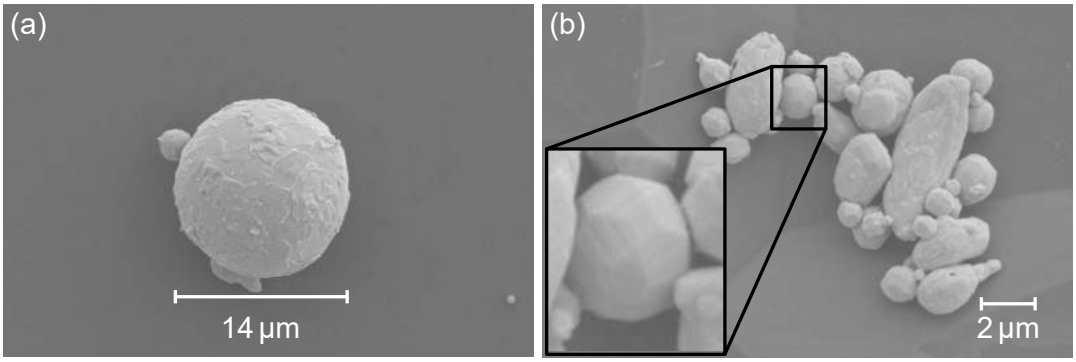


**Figure 4.20:** Scanning electron microscope pictures of lead microparticles (a) before and (b) after being heated at 300 °C in a nitrogen atmosphere. Note that the crystallographic facets are observable on the surface of the particles after heating, especially for the smaller particles (in the inset).

Fig. 4.20 shows evidence that monocrystalline lead microparticles could be produced by warming up the particles to near their melting temperature (330 °C) in an inert (nitrogen) atmosphere and letting them cool down slowly. This lets the atoms in the microparticle rearrange into more thermodynamically favorable configurations, where the most favorable is a monocrystal.

Another way to increase the quality factor of the mechanical modes is to completely remove any non-superconducting metallic parts from the vicinity of the particle, which has been shown to give quality factors of up to $10^7$ [42], [45]. In Fig. 4.9(b) a plastic sample stage (in white) with a sapphire piece on top is hanging at the bottom of the sample stage. Additionally, a new sample holder made of glass, STYCAST glue, and niobium and titanium pieces has been produced to levitate a particle with no non-superconducting metals in its immediate vicinity. Glass and the STYCAST are electrical insulators but good thermal conductors, and niobium and titanium are superconductors at mK temperatures. The assembly is shown in Fig. 4.21.

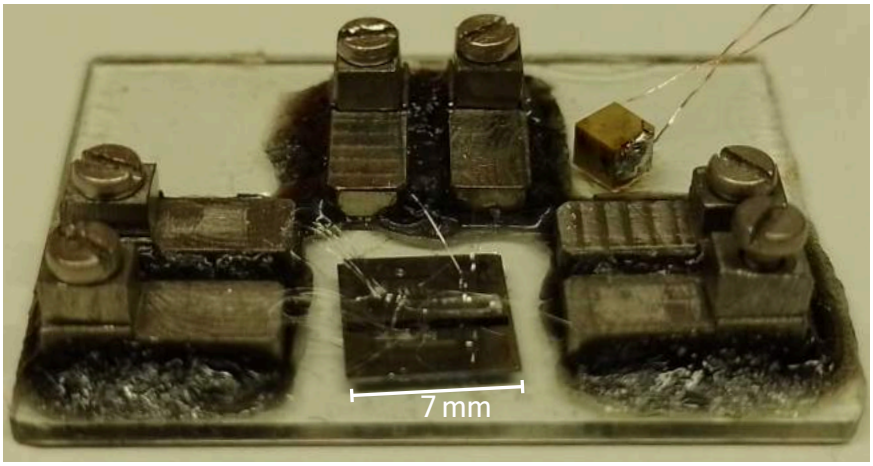


**Figure 4.21:** Picture of a glass sample holder with Niobium contact pads and titanium screws with a wire-bonded two-chip trap. The cube on the top right is a piezoelectric transducer used to shake the sample if the magnetic force is insufficient to lift the particle.

## Decreasing noise

To decrease the rather large noise floor in our SQUID spectra to the noise floor of the SQUID magnetometer, anything that could generate a change in magnetic flux on either the SQUID sensor or the pickup loops in the trap must be removed or its effect mitigated. Magnetic flux in a loop can be changed in many ways, but the three main contributors to the flux changes are (i) magnetic fields generated by electrical currents from the electrical grid in the laboratory or within the cryostat mainly but not limited to 50 Hz and multiples, (ii) current noise from the equipment used in the experiments such as the current source used to feed the magnetic trap, and (iii) mechanical vibrations because a loop moving in an inhomogeneous field will experience a changing magnetic flux.

The first contribution cannot be eliminated, but it can be mitigated using further magnetic shielding. We had a 12 cm deep and 18.5 cm diameter niobium cylinder with the bottom end closed built via spot welding to enclose the whole sample space, which should provide magnetic shielding of the sample from 9 K. The shield and its magnetic field distributions under a vertical and a horizontal field are shown in Fig. 4.22, which have shielding factors of

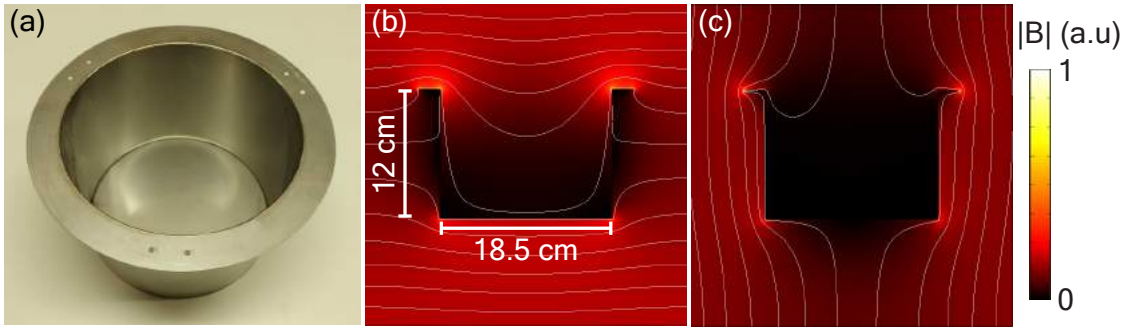


**Figure 4.22:** (a) Niobium cylinder with one end closed and one end open, meant to encase the whole sample stage. Magnetic field distributions around the cylinder when under (b) a horizontal and (c) a vertical magnetic field. The shielding factor is calculated 1 cm away from the bottom of the cylinder, where the sample would be.

$9.4 \cdot 10^2$ and 8.5, respectively. On top of this, another two magnetic shields will cover the sample. A tin-plated copper cylinder hanging from the mixing stage provides shielding below 3.4 K ($T_c$ of tin), and a mu-metal shield hanging from the room temperature vacuum can provides magnetic shielding from room temperature. The addition of these shields with significantly larger depths should increase the shielding factor by at least two orders of magnitude for lateral fields and five orders of magnitude for vertical fields.

The second contribution (current noise) can be eliminated by using persistent currents. A persistent current is a current trapped in a superconducting loop. They have no intrinsic noise, and they seem to have effectively infinite lifetimes [127]. In order to create a persistent current, one needs to be able to break the superconductivity somewhere in the superconducting loop. This is done with persistent current switches (PCS), which either heat the superconductor above the critical temperature, generate a magnetic field above the critical field of the superconductor, or even mechanically break contact [67], [128]. In our experiment, we have placed a superconducting short made of 190 µm diameter twisted NbTi wire in the superconducting cabling within the cryostat. When sending a current to the magnetic trap, and breaking superconductivity in the short by turning on the heater, the supercurrent flows through the magnetic trap alone. Then, the heater is turned off and the short is left to cool down. When the short becomes superconducting, it will trap the current running in the magnetic trap within the superconducting loop

formed by the trap and the short (see Fig. 4.23). The current supply to the trap can then be turned off and the superconducting loop will induce the same amount of current that was provided by the power source to maintain the same amount of magnetic flux threading the superconducting loop (of the trap plus the short).

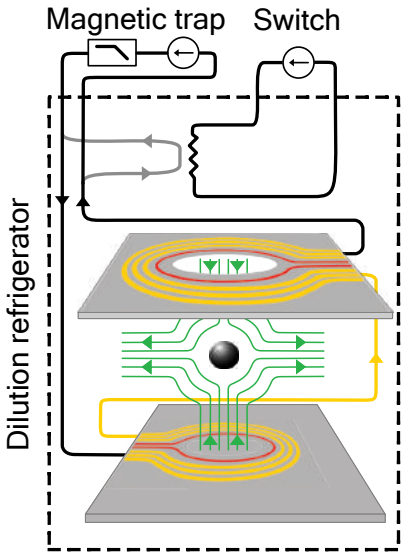


**Figure 4.23:** Schematic view of the persistent current switch, consisting of a resistor in thermal contact with the superconducting short (gray) in the high current line that feeds current to the magnetic trap, as implemented in our experimental setup. Current flows through the superconducting short only when it has been trapped by the persistent current switch.

The drawback with using a persistent current switch is that to make a superconducting short additional superconducting wiring must be introduced in the cryostat, which makes the magnetic trap more susceptible to magnetic noise via the additional wire length.

The third contribution (vibrations), can be mitigated via further vibration isolation stages. A two-stage (i.e. double elastic pendulum) system has been built and is to be tested in future experiments. We expect an improvement of three orders of magnitude in the mechanical attenuation of the cryostat vibrations (see Fig. 4.24).

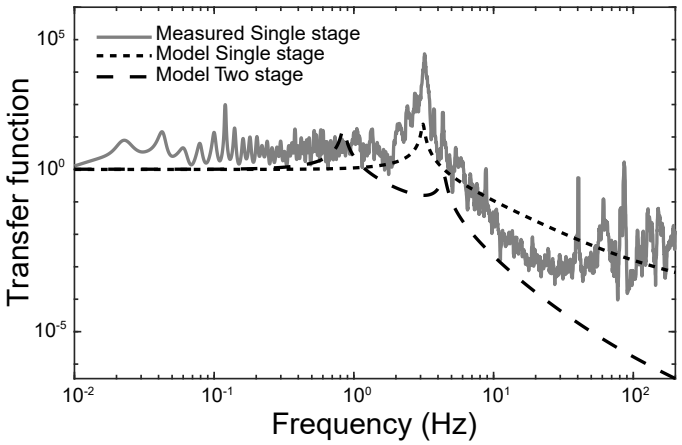


**Figure 4.24:** Transfer functions of the single-stage vibration isolation as measured and predicted by the model and of the two-stage system that will be employed in future experiments.

# CHAPTER 5

# Conclusions and outlook

This thesis was concerned with chip-based magnetic levitation of superconducting microparticles.

We have developed analytical and FEM models for chip-based magnetic traps. These models have been used to design magnetic traps based on microscale superconducting coils and accurately model the COM motion of levitated superconducting particles. Further, we have developed microfabrication processes to manufacture chip-based magnetic traps, as well as superconducting microparticles in the form of rings, discs, and spheres.

We have succeeded at magnetically levitating superconducting 50 µm spheres made of Pb and SnPb at 4 K and 50 mK, in magnetic traps based on two-chip stacks of superconducting planar coils. Furthermore, we have shown that the COM motion can be detected optically and via SQUID magnetometry. The levitation is stable over days when using magnetic means of detection. The

measured COM frequencies (between 30-150 Hz), as well as their dependence on trap current, temperature, and density of the particle material, are in good agreement with our model of the system. Further, our model explains the observed nonlinear particle motion due to the anharmonicity of the magnetic trap and nonlinear pick-up efficiencies.

We have demonstrated that the COM motion can be controlled via direct feedback, by applying a magnetic force on the particle through additional integrated coils on the chip trap. We have discussed the prospects of bringing the particle motion to the ground state using direct feedback cooling, and what steps should be taken to move in this direction. In principle, technical improvements to the current devices would allow ground-state cooling of the particle motion via direct feedback.

We have identified mechanical vibrations driving the particle motion and magnetic noise as the limiting factors of the experiment. Implementing a vibration isolation system in the form of an elastic pendulum has attenuated mechanical vibrations of the cryostat by approximately 40 dB. The vibration isolation has made ring-down measurements possible, which give quality factors as large as $10^5$. The limiting quality factors for several conceivable dissipation mechanisms have been estimated, but none seem to explain the quality factors measured in the experiments.

In future experiments, vibration isolation via multi-stage systems (i.e. several elastic pendula) will reduce random excitations of the particle motion by cryostat vibrations by up to 95 dB. The experimental setup will be placed within several layers of large magnetic shields, both mu-metal and superconducting. Additionally, a superconducting switch will be used to power the magnetic trap with a persistent current, which will eliminate the current noise in the trap.

Reducing the noise in the system will allow us to cool down the particle motion using feedback more effectively. In the future, the implementation of the feedback will change from direct feedback to optimal cooling with a Kalman filter [28].

A further improvement to the experimental setup is to exchange all non-superconducting metallic pieces within the magnetic shield with electrical in-

sulators with large thermal conductivity. This will remove the possibility of dissipating energy via eddy currents, which should increase the mechanical quality factor of the particle. We will use ceramic materials, such as aluminum nitride and sapphire, which are electrical insulators, and good thermal conductors, which can be machined on a computerized numerical control milling machine.

There is also room for improvement for both the magnetic trap and the superconducting particles. Further miniaturization of the magnetic traps is within reach by employing flip-chip technology and superconducting vias. In this way, the dimensions of the superconducting trap can be reduced by at least one order of magnitude, increasing the magnetic field gradient and, thus, bringing the trap frequencies up to the kHz regime. Furthermore, hollow particles with a superconducting shell can be employed to reduce the effective mass of the levitated object by two orders of magnitude, which would further increase the trap frequencies by another order of magnitude to tens of kHz.

Thermal annealing of the particles would reduce the crystallographic defects, and ideally create a monocrystal. This would eliminate flux trapping sites from the superconductor, eliminating flux-related dissipation mechanisms.

Sensing of minute forces could be performed in future experiments with smaller superconducting microparticles made of light materials such as aluminium. If a 1 µm diameter aluminium sphere was levitated in one of our current devices at 50 mK with a mechanical $Q = 10^7$ and thermally driven motion, the force noise of the mechanical motion would be $S_{\mathrm{FF}} = \sqrt{4k_{\mathrm{B}}Tm\gamma}$ =$5.4 \times 10^{-22}\,\mathrm{N\,Hz^{-0.5}}$, which is on par with the state-of-the-art ($1.2\times10^{-20}\,\mathrm{N\,Hz^{-0.5}}$) [61]–[64]. If the particle motion were cooled to the ground state, the sensitivity would become $S_{\mathrm{FF}} = \sqrt{4k_{\mathrm{B}}Tm\gamma}$ =$1.8 \times 10^{-25}\,\mathrm{N\,Hz^{-0.5}}$. Similarly, a 50 µm diameter lead sphere levitated in one of our current devices with a mechanical $Q = 10^7$ and thermally driven motion, the acceleration noise would be $S_{\mathrm{gg}} = S_{\mathrm{FF}}/m$ =$1.9 \times 10^{-10}\,\mathrm{g\,Hz^{-0.5}}$, and if it were cooled to the ground state $S_{\mathrm{gg}}$ =$5.8 \times 10^{-14}\,\mathrm{g\,Hz^{-0.5}}$, which is beyond the state-of-the-art ($1 \times 10^{-12}\,\mathrm{g\,Hz^{-0.5}}$) [15], [59], [60]. This latter value is the most significant because we have seen that ground-state cooling levitated particles of this size are in principle possible via technical improvements.

The COM motion of levitated particles can be coupled to superconducting quantum circuits other than SQUID magnetometers. Future experiments will have the pick-up loop transport the flux signal of the particle motion to a flux-tunable superconducting resonator, thus coupling the particle motion to a superconducting, flux-tunable, nonlinear microwave cavity. The advantage of such a system is that the coupling between the microwave cavity and the particle motion can be enhanced by increasing the number of microwave photons in the cavity, as well as by tuning its intrinsic flux non-linearity with external magnetic fields [72]–[76]. A strong coupling between the microwave cavity and the particle motion would enable the generation of squeezed mechanical states, which could be used for even more precise detection of forces and accelerations [35]. It would also allow for the generation of massive non-classical mechanical states, such as Fock states [17] or cat states [18], and even matter-wave interferometry experiments [46].

# CHAPTER 6

# Appendix

## 6.1 Fabrication recipes

### Substrate preparation

When starting fabrication with a new wafer or a sample that has a protective layer of resist on top.

- 1165 Remover bath 80 °C for 5 min
- IPA bath 2 min
- Rinse in water with a water gun and blow dry with $N_2$ gun

To avoid dielectric loss, the native oxide layer of the substrate must be

removed.

- Dip in 2% HF for 30 s
- Rinse in water in a Quick Dump Rinsing (QDR) bath and blow dry with $N_2$

## Nb deposition

With no heating or cooling, use the cold mount and sputter at room temperature. To sputter Nb, use the following parameters in the DCA metal cluster: 200 W source power, 12 µbar chamber pressure, 80 sccm of Argon flow.
The deposition rate (typically 0.7 nm/s) changes as the niobium target is consumed and should be measured after two months of regular use.

In the recipe file, modify the following as needed:

- Pre-sputter for 60 s to stabilize the flow of material.
- Sputter time for half of the desired thickness.

The wait for 1 min for the film stress to relax, and repeat the recipe to sputter the remaining half of the desired thickness.

## Electron Beam Lithography (EBL)

Exposing negative resist will give you a resist pattern with the same shape as the design file, since the electron beam will interlink the polymer and the developer will dissolve any resist not exposed.

Similarly, exposing positive resist will give you a resist pattern that is the complementary shape of the design file, since the electron beam will break down the polymer and the developer will dissolve resist that has been exposed.

### Positive Resist

#### Direct pattern transfer

- Dry on a hotplate 110 °C 1 min to remove water
- Chemical vapour deposition of HMDS (hexamethyldisilazane), used as a primer for resist adhesion
- Spin coat UV5 resist 3000 rpm, which gives a 800 nm thick resist layer
- Bake resist on hotplate 130 °C 2 min
- Expose the design with 35 µC/cm$^2$, 12 nA beam with 300 µm aperture at 1 kV acceleration voltage.
  These setting assume that Proximity Effect Correction (PEC) has been performed in the design using the BEAMER software.
- Post-bake resist on hotplate 130 °C 1.5 min
- Develop resist in MF-CD-26 developer bath for 1 min while stirring
- Etch in $O_2$ 50 W 50 mTorr 250 sccm 40 s to remove undeveloped resist (de-scumming)

#### Lift-off

- Dry on a hotplate 110 °C 1 min to remove water
- Chemical vapour deposition of HMDS (hexamethyldisilazane), used as a primer for resist adhesion
- Spin coat Copolymer EL10 resist 5000 rpm, which gives a 300 nm thick resist layer
- Bake resist on hotplate 130 °C 2 min
- Spin coat PMMA A4 resist 3000 rpm, which gives a 220 nm thick resist

layer

- Bake resist on hotplate 130 °C 5 min
- Expose the design with 372 µC/cm$^2$, 325 nA beam with 400 µm aperture at 1 kV acceleration voltage.
  These setting assume that Proximity Effect Correction (PEC) has been performed in the design using the BEAMER software.
- Develop in IPA:DI-water 93:7 for 5 min
- Etch in $O_2$ 50 W 50 mTorr 250 sccm 40 s to remove undeveloped resist (de-scumming)

### Negative Resist

- Dry on a hotplate 110 °C 1 min to remove water
- Chemical vapor deposition of HMDS (hexamethyldisilazane), used as a primer for resist adhesion
- Spin coat UVN2300-0.5 resist 3000 rpm, which gives a 700 nm thick resist layer
- Bake resist on hotplate 110 °C 1 min
- Expose the design with 22 µC/cm$^2$, 10 nA beam with 300 µm aperture at 1 kV acceleration voltage.
  These settings assume that Proximity Effect Correction (PEC) has been performed in the design using the BEAMER software.
- Post-bake resist on hotplate 110 °C 1 min
- Develop resist in MF-CD-26 developer bath for 1 min while stirring
- Etch in $O_2$ 50 W 50 mTorr 250 sccm 40 s to remove undeveloped resist (de-scumming)

## Laser lithography

### Positive resist

### Direct pattern transfer

- Dry on a hotplate 110 °C 1 min to remove water
- Spin coat S1813 resist 3000 rpm, which gives a 1.3 µm thick resist layer
- Bake resist on hotplate 110 °C 1 min
- Expose the design with focus/intensity/transmission settings of −40/90/100 These settings drift quite a lot in time and between designs. Hence a dose study should be performed before exposing a design for the first time.
- Develop resist in MF-CD-26 developer bath for 1 min while stirring
- Etch in $O_2$ 50 W 50 mTorr 250 sccm 40 s to remove undeveloped resist (de-scumming)

### Lift-off

- Dry on a hotplate 110 °C 1 min to remove water
- Spin coat LOR3A resist 4000 rpm, which gives a 300 nm thick resist layer
- Spin coat S1805 resist 3000 rpm, which gives a 500 nm thick resist layer

## Etching

### Reactive Ion Etching (RIE) of Nb

The etch rate is approx. 125 nm/min. However, it is dependent on the exposed area, so the larger the area of Nb that is exposed, the slower the etch rate and vice versa. Furthermore, the etch rate also changes as the process chamber is opened and exposed to the atmosphere. It will therefore change after any major tool maintenance has been performed.

For chips:

- 50 W platen power (also called CCP for Capacitive Couple Power), 50 W Inductively coupled plasma (ICP), 20 mTorr chamber pressure, 20:20 sccm Ar : $SiCl_4$ flow.

For wafers:

- 50 W platen power (also called CCP for Capacitive Couple Power), 50 W ICP, 20 mTorr chamber pressure, 20:20 sccm Ar : NF3 flow.

### RIE of Si and $SiO_2$

- 50 W platen power (also called CCP for Capacitive Couple Power), 20 mTorr chamber pressure, 20:40 sccm Ar : $NF_3$ flow.

### Deep Si etch (Bosch Process)

In order to etch through a silicon substrate, one can use the Bosch process, which is an etch process developed to etch through several hundreds of micrometers of silicon.

- Deposit a 25 nm thick Al2O3 layer with ALD at 125 °C to conformally coat the substrate

- Sputter a 300 nm thick Al layer on top of the Al2O3
- Spin coat S1813 at 3000rpm
- Bake resist at 110 °C on a hot plate for 1 min
- Expose in DWL laser writer with 15/85/100 focus/intensity/transmission, or in MLA laser writer with 130 mJ $cm^{-2}$
- Develop in MF-CD-26 for 1 min to develop S1813. Add at least 4 min to the development time to wet-etch the Al layer under the resist, to transfer the resist pattern to the aluminium layer.
- Etch in $O_2$ 50 W 50 mTorr 250 sccm 40 s to remove undeveloped resist (de-scumming)
- Use RIE etch of Si and $SiO_2$ for 30 s to remove native oxide from the substrate (optional)
- Use fast Bosch Process recipe (12:8 s etch:passivation per cycle) and apply 450 cycles to etch through 300 µm

## 6.2 Levitation with magnet traps

This device architecture was the result of lateral thinking and thus breaks with the theme of superconducting coils. However, they were the first devices to levitate superconducting particles and merit mention because of this.

## 6.3 Multiplex traps

Because the magnetic traps are small, many of them can be fabricated in the same chip using the same superconducting coils. In Fig. 6.2 we show a chip trap with two trap sites. The number of trap sites a chip can have is limited by the available area on the silicon chip.

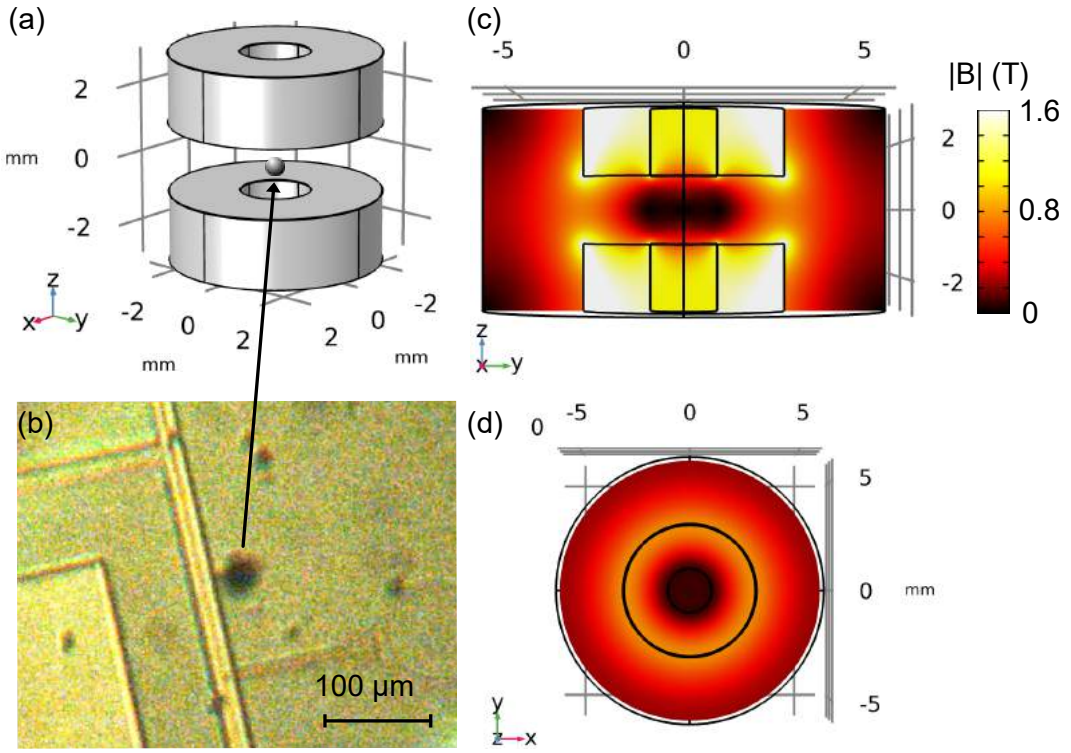


**Figure 6.1:** (a) Schematic representation of the magnet trap, showing two millimeter-sized ring magnets with opposing magnetization. (b) A YBCO cluster levitating inside a magnet trap, on top of a chip with niobium structures that acts only as a carrier for the particle. Magnetic field distributions of the (c) vertical and (d) horizontal cut planes at the levitation point between the magnets.

Furthermore, a dual trap can be used to implement a gradiometric pick-up. If two pick-up loops, one in each trap site, are connected gradiometrically the flux generated by the trap in the pick-up loops is subtracted. When a particle is levitated only on one site, the pick-up loop will see the entirety of the flux generated by the particle motion, whereas the magnetic flux of the trap is cancelled out. This cancellation will be total (i.e. no background) if the two trap sites and pick-up loops are identical. This will be true down to the precision of the fabrication process because both the trap and pick-up coils would be fabricated simultaneously.

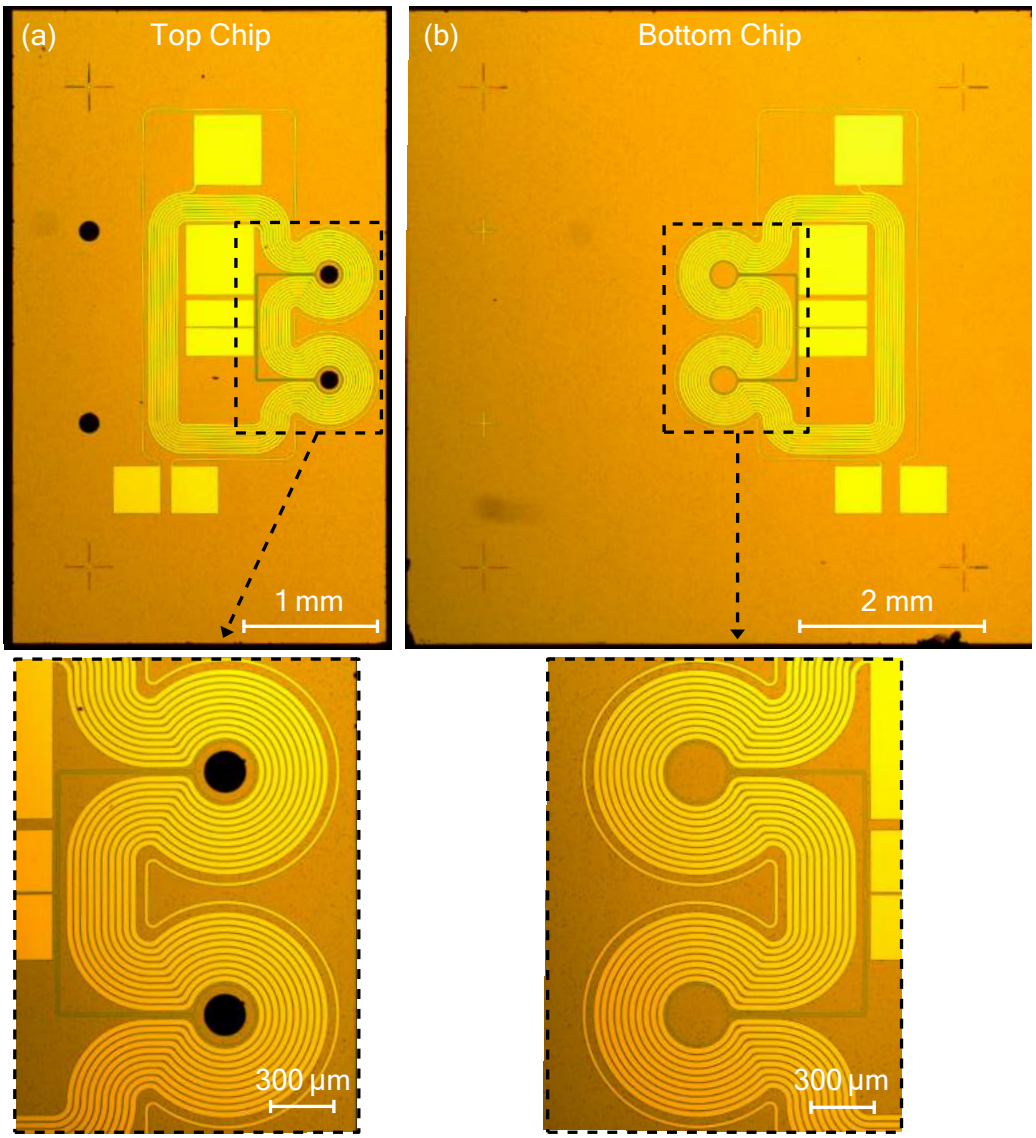


**Figure 6.2:** Two-chip trap with multiple trap sites. (a) Bottom and (b) top chips of a two-chip trap with two trap sites, the pictures below show the trap regions under larger magnification.

# CHAPTER 7

# Summary of included papers

This chapter provides a summary of the included papers.

## 7.1 Paper A

**Martí Gutierrez Latorre**, Joachim Hofer, Matthias Rudolph, Witlef Wieczorek
Chip-based superconducting traps for levitation of micrometer-sized particles in the Meissner state
*Superconducting Science and Technology*,
vol. 33, no. 10, pp. 105002-105017, Aug. 2020
DOI: 10.1088/1361-6668/aba6e1 .

We show the design and fabrication of different magnetic chip-trap architectures. We analyzed the trap properties in detail using analytical [100], [102], [129] and FEM modeling [103], [130]–[132]. The FEM modeling is based on the **A**-V formulation of the Maxwell-London equations and is applicable to superconductors in the Meissner state. We show that magnetic trap properties, like trap stability and frequency, can significantly differ from idealized, analytical models due to the breaking of symmetry by coil openings, demagnetizing effects, and flux quantization. We found that a chip-based Anti-Helmholtz Coil (AHC) trap is capable of levitating micrometer-sized particles of spherical, cylindrical, and ring shape with trap frequencies well above 10 kHz for a current density of $10^{11}\,\mathrm{A/m^2}$ in the trap wires. Further, we confirmed numerically that read-out of the motion of the levitated particle using a pick-up loop in its vicinity [34], [66] should lead to clearly detectable signals using presently available SQUID technology [133]–[135]. We concluded that the analyzed chip-based superconducting traps are a viable approach for future quantum experiments that aim at levitating superconducting particles in the Meissner state [34], [41], [46].

## 7.2 Paper B

**Martí Gutierrez Latorre**, Achintya Paradkar, David Hambraeus, Gerard Higgins, Witlef Wieczorek
A Chip-Based Superconducting Magnetic Trap for Levitating Superconducting Microparticles
*Published in Transactions on Applied Superconductivity*,
vol. 32, no. 4, pp. 1800305, Feb. 2022.
©DOI: 10.1109/TASC.2022.3147730 .

We present the design, simulation, and fabrication of a chip-based superconducting magnetic trap for levitating superconducting microparticles of diameters between 0.5 µm and 200 µm. We demonstrated stable levitation of 50 µm diameter superconducting particles in this trap at temperatures of 4 K and 40 mK via direct observation of the levitated particle inside a dilution refrigerator with an optical microscope.

## 7.3 Paper C

**Martí Gutierrez Latorre**, Gerard Higgins, Achintya Paradkar, Thilo Bauch, Witlef Wieczorek
Superconducting microsphere magnetically levitated in an anharmonic potential
*Publisehd in ArXiv*,
Oct. 2022.
©DOI: 10.48550/arXiv.2210.13451 .

Magnetically levitated superconducting microparticles offer a promising path to quantum experiments with picogram to microgram objects. In this work, we levitate a 700 ng $\sim 10^{17}$ amu superconducting microsphere in a magnetic chip trap in which detection is integrated. We measure the particle's center-of-mass motion using a DC-SQUID magnetometer. The trap frequencies are continuously tunable between 30 and 160 Hz and the particle remains stably trapped over days in a dilution refrigerator environment. We characterize motional-amplitude-dependent frequency shifts, which arise from trap anharmonicities, namely Duffing nonlinearities and mode couplings. We explain this nonlinear behavior using finite element modelling of the chip-based trap potential. This work constitutes a first step towards quantum experiments and ultrasensitive inertial sensors with magnetically levitated superconducting microparticles.

# References


[1] C. Davisson and L. H. Germer, "Diffraction of electrons by a crystal of nickel," *Phys. Rev.*, vol. 30, pp. 705–740, 6 Dec. 1927. DOI: 10.1103/PhysRev.30.705.

[2] C. Jönsson, "Elektroneninterferenzen an mehreren künstlich hergestellten feinspalten," *Zeitschrift für Physik 1961 161:4*, vol. 161, pp. 454–474, 4 Aug. 1961, ISSN: 14346001. DOI: 10.1007/BF01342460.

[3] A. Zeilinger, R. Gähler, C. G. Shull, W. Treimer, and W. Mampe, "Single- and double-slit diffraction of neutrons," *Rev. Mod. Phys.*, vol. 60, pp. 1067–1073, 4 Oct. 1988. DOI: 10.1103/RevModPhys.60.1067.

[4] D. W. Keith, M. L. Schattenburg, H. I. Smith, and D. E. Pritchard, "Diffraction of atoms by a transmission grating," *Phys. Rev. Lett.*, vol. 61, pp. 1580–1583, 14 Oct. 1988. DOI: 10.1103/PhysRevLett.61.1580.

[5] O. Carnal and J. Mlynek, "Young's double-slit experiment with atoms: A simple atom interferometer," *Phys. Rev. Lett.*, vol. 66, pp. 2689–2692, 21 May 1991. DOI: 10.1103/PhysRevLett.66.2689.

[6] M. Arndt, O. Nairz, J. Vos-Andreae, C. Keller, G. V. D. Zouw, and A. Zellinger, "Wave–particle duality of c60 molecules," *Nature 1999*

*401:6754*, vol. 401, pp. 680–682, 6754 Oct. 1999, ISSN: 1476-4687. DOI: 10.1038/44348.

[7] T. Juffmann, A. Milic, M. Müllneritsch, *et al.*, "Real-time single-molecule imaging of quantum interference," *Nature Nanotechnology 2012 7:5*, vol. 7, pp. 297–300, 5 Mar. 2012, ISSN: 1748-3395. DOI: 10.1038/nnano.2012.34.

[8] Y. Y. Fein, P. Geyer, P. Zwick, *et al.*, "Quantum superposition of molecules beyond 25 kda," *Nature Physics 2019 15:12*, vol. 15, pp. 1242–1245, 12 Sep. 2019, ISSN: 1745-2481. DOI: 10.1038/s41567-019-0663-9.

[9] M. Arndt and K. Hornberger, "Testing the limits of quantum mechanical superpositions," *Nature Physics*, vol. 10, pp. 271–277, 4 Apr. 2014, ISSN: 1745-2473. DOI: 10.1038/nphys2863.

[10] A. Bassi, K. Lochan, S. Satin, T. P. Singh, and H. Ulbricht, "Models of wave-function collapse, underlying theories, and experimental tests," *Rev. Mod. Phys.*, vol. 85, pp. 471–527, 2 Apr. 2013. DOI: 10.1103/RevModPhys.85.471.

[11] R. Penrose, "On the gravitization of quantum mechanics 1: Quantum state reduction," *Foundations of Physics*, vol. 44, pp. 557–575, 5 Jan. 2014, ISSN: 00159018. DOI: 10.1007/S10701-013-9770-0/FIGURES/14.

[12] R. Colella, A. W. Overhauser, and S. A. Werner, "Observation of gravitationally induced quantum interference," *Phys. Rev. Lett.*, vol. 34, pp. 1472–1474, 23 Jun. 1975. DOI: 10.1103/PhysRevLett.34.1472.

[13] A. Louchet-Chauvet, T. Farah, Q. Bodart, *et al.*, "The influence of transverse motion within an atomic gravimeter," *New Journal of Physics*, vol. 13, no. 6, p. 065 025, Jun. 2011. DOI: 10.1088/1367-2630/13/6/065025.

[14] V. Xu, M. Jaffe, C. D. Panda, S. L. Kristensen, L. W. Clark, and H. Müller, "Probing gravity by holding atoms for 20 seconds," *Science*, vol. 366, no. 6466, pp. 745–749, 2019. DOI: 10.1126/science.aay6428.

[15] *Absolute quantum gravimeter*, Jul. 2021.

[16] A. D. O'connell, M. Hofheinz, M. Ansmann, *et al.*, "Quantum ground state and single-phonon control of a mechanical resonator," 2010. DOI: 10.1038/nature08967.

[17] Y. Chu, P. Kharel, T. Yoon, L. Frunzio, P. T. Rakich, and R. J. Schoelkopf, "Creation and control of multi-phonon fock states in a bulk acoustic-wave resonator," *Nature 2018 563:7733*, vol. 563, pp. 666–670, 7733 Nov. 2018, ISSN: 1476-4687. DOI: 10.1038/s41586-018-0717-7.

[18] M. Bild, M. Fadel, Y. Yang, *et al.*, *Schrödinger cat states of a 16-microgram mechanical oscillator*, 2022. DOI: 10.48550/ARXIV.2211.00449.

[19] B. Schrinski, Y. Yang, U. von Lüpke, *et al.*, *Macroscopic quantum test with bulk acoustic wave resonators*, 2022. DOI: 10.48550/ARXIV.2209.06635.

[20] J. R. Friedman, V. Patel, W. Chen, S. K. Tolpygo, and J. E. Lukens, "Quantum superposition of distinct macroscopic states," *Nature 2000 406:6791*, vol. 406, pp. 43–46, 6791 Jul. 2000, ISSN: 1476-4687. DOI: 10.1038/35017505.

[21] M. Zawisky, M. Baron, R. Loidl, and H. Rauch, "Testing the world's largest monolithic perfect crystal neutron interferometer," *Nuclear Instruments and Methods in Physics Research Section A: Accelerators, Spectrometers, Detectors and Associated Equipment*, vol. 481, no. 1, pp. 406–413, 2002, ISSN: 0168-9002. DOI: https://doi.org/10.1016/S0168-9002(01)01253-0.

[22] S. M. Dickerson, J. M. Hogan, A. Sugarbaker, D. M. S. Johnson, and M. A. Kasevich, "Multiaxis inertial sensing with long-time point source atom interferometry," *Phys. Rev. Lett.*, vol. 111, p. 083 001, 8 Aug. 2013. DOI: 10.1103/PhysRevLett.111.083001.

[23] T. Kovachy, P. Asenbaum, C. Overstreet, *et al.*, "Quantum superposition at the half-metre scale," *Nature 2015 528:7583*, vol. 528, pp. 530–533, 7583 Dec. 2015, ISSN: 1476-4687. DOI: 10.1038/nature16155.

[24] C. Kohstall, S. Riedl, E. R. S. Guajardo, L. A. Sidorenkov, J. H. Denschlag, and R. Grimm, "Observation of interference between two molecular bose–einstein condensates," *New Journal of Physics*, vol. 13, no. 6, p. 065 027, Jun. 2011. DOI: 10.1088/1367-2630/13/6/065027.

[25] H. Müntinga, H. Ahlers, M. Krutzik, *et al.*, "Interferometry with bose-einstein condensates in microgravity," *Phys. Rev. Lett.*, vol. 110, p. 093 602, 9 Feb. 2013. DOI: 10.1103/PhysRevLett.110.093602.

[26] A. Ashkin, "Acceleration and trapping of particles by radiation pressure," *Phys. Rev. Lett.*, vol. 24, pp. 156–159, 4 Jan. 1970. DOI: 10.1103/PhysRevLett.24.156.

[27] V. Jain, J. Gieseler, C. Moritz, C. Dellago, R. Quidant, and L. Novotny, "Direct measurement of photon recoil from a levitated nanoparticle," *Phys. Rev. Lett.*, vol. 116, p. 243 601, 24 Jun. 2016. DOI: 10.1103/PhysRevLett.116.243601.

[28] L. Magrini, P. Rosenzweig, C. Bach, *et al.*, "Real-time optimal quantum control of mechanical motion at room temperature," *Nature*, vol. 595, no. 7867, pp. 373–377, 2021. DOI: 10.1038/s41586-021-03602-3.

[29] J. Piotrowski, D. Windey, J. Vijayan, *et al.*, *Simultaneous ground-state cooling of two mechanical modes of a levitated nanoparticle*, 2022. DOI: 10.48550/ARXIV.2209.15326.

[30] F. Monteiro, S. Ghosh, A. G. Fine, and D. C. Moore, "Optical levitation of 10-ng spheres with nano-$g$ acceleration sensitivity," *Phys. Rev. A*, vol. 96, p. 063 841, 6 Dec. 2017. DOI: 10.1103/PhysRevA.96.063841.

[31] U. Delić, M. Reisenbauer, K. Dare, *et al.*, "Cooling of a levitated nanoparticle to the motional quantum ground state," *Science*, vol. 367, no. 6480, pp. 892–895, 2020. DOI: 10.1126/science.aba3993.

[32] F. Tebbenjohanns, M. L. Mattana, M. Rossi, M. Frimmer, and L. Novotny, "Quantum control of a nanoparticle optically levitated in cryogenic free space," *Nature*, vol. 595, no. 7867, pp. 378–382, 2021. DOI: 10.1038/s41586-021-03617-w.

[33] A. Ranfagni, K. Børkje, F. Marino, and F. Marin, "Two-dimensional quantum motion of a levitated nanosphere," *Phys. Rev. Research*, vol. 4, p. 033 051, 3 Jul. 2022. DOI: 10.1103/PhysRevResearch.4.033051.

[34] O. Romero-Isart, L. Clemente, C. Navau, A. Sanchez, and J. I. Cirac, "Quantum magnetomechanics with levitating superconducting microspheres," *Phys. Rev. Lett.*, vol. 109, p. 147 205, 14 Oct. 2012. DOI: 10.1103/PhysRevLett.109.147205.

[35] T. Weiss, M. Roda-Llordes, E. Torrontegui, M. Aspelmeyer, and O. Romero-Isart, "Large quantum delocalization of a levitated nanoparticle using optimal control: Applications for force sensing and entangling via weak forces," *Phys. Rev. Lett.*, vol. 127, p. 023 601, 2 Jul. 2021, ISSN: 10797114. DOI: 10.1103/PHYSREVLETT.127.023601.

[36] J. Gieseler, L. Novotny, and R. Quidant, "Thermal nonlinearities in a nanomechanical oscillator," *Nat. Phys.*, vol. 9, no. 12, pp. 806–810, 2013. DOI: 10.1038/nphys2798.

[37] M. G. Latorre, J. Hofer, M. Rudolph, and W. Wieczorek, "Chip-based superconducting traps for levitation of micrometer-sized particles in the meissner state," *Superconductor Science and Technology*, vol. 33, no. 10, p. 105 002, Aug. 2020. DOI: 10.1088/1361-6668/aba6e1.

[38] C. Navau, S. Minniberger, M. Trupke, and A. Sanchez, "Levitation of superconducting microrings for quantum magnetomechanics," *Phys. Rev. B*, vol. 103, no. 17, p. 174 436, May 2021. DOI: 10.1103/PhysRevB.103.174436.

[39] F. Moon and P. Chang, *Superconducting Levitation: Applications to Bearings and Magnetic Transportation* (A Wiley interscience publication). Wiley, 1994, ISBN: 978-0-471-55925-2.

[40] Y. Takahashi, J. Suzuki, N. Yoneyama, *et al.*, "Magnetic trapping of superconducting submicron particles produced by laser ablation in superfluid helium," *Appl. Phys. Express*, vol. 10, p. 22 701, 2017. DOI: 10.7567/APEX.10.022701.

[41] M. Cirio, G. K. Brennen, and J. Twamley, "Quantum Magnetomechanics: Ultrahigh- Q -Levitated Mechanical Oscillators," *Physical Review Letters*, vol. 109, no. 14, 2012, ISSN: 0031-9007, 1079-7114. DOI: 10.1103/PhysRevLett.109.147206.

[42] A. Vinante, P. Falferi, G. Gasbarri, A. Setter, C. Timberlake, and H. Ulbricht, "Ultralow mechanical damping with meissner-levitated ferromagnetic microparticles," *Phys. Rev. Applied*, vol. 13, p. 064 027, 6 Jun. 2020. DOI: 10.1103/PhysRevApplied.13.064027.

[43] D. Zheng, Y. Leng, X. Kong, *et al.*, "Room temperature test of the continuous spontaneous localization model using a levitated microoscillator," *Phys. Rev. Research*, vol. 2, p. 013 057, 2020. DOI: 10.1103/PhysRevResearch.2.013057.

[44] Y. Leng, R. Li, X. Kong, *et al.*, "Mechanical dissipation below 1 muhz with a cryogenic diamagnetic levitated micro-oscillator," *Phys. Rev. Appl.*, vol. 15, no. 2, p. 024 061, Feb. 2021, ISSN: 2331-7019. DOI: 10.1103/PhysRevApplied.15.024061.

[45] J. Hofer, G. Higgins, H. Huebl, *et al.*, *High-q magnetic levitation and control of superconducting microspheres at millikelvin temperatures*, 2022. DOI: 10.48550/ARXIV.2211.06289.

[46] H. Pino, J. Prat-Camps, K. Sinha, B. P. Venkatesh, and O. Romero-Isart, "On-chip quantum interference of a superconducting microsphere," *Quantum Science and Technology*, vol. 3, no. 2, p. 025 001, Jan. 2018. DOI: 10.1088/2058-9565/aa9d15.

[47] E. E. Wollman, C. U. Lei, A. J. Weinstein, *et al.*, "Quantum squeezing of motion in a mechanical resonator," *Science*, vol. 349, no. 6251, pp. 952–955, 2015. DOI: 10.1126/science.aac5138.

[48] J.-M. Pirkkalainen, E. Damskägg, M. Brandt, F. Massel, and M. A. Sillanpää, "Squeezing of quantum noise of motion in a micromechanical resonator," *Phys. Rev. Lett.*, vol. 115, p. 243 601, 24 Dec. 2015. DOI: 10.1103/PhysRevLett.115.243601.

[49] C. Gonzalez-Ballestero, M. Aspelmeyer, L. Novotny, R. Quidant, and O. Romero-Isart, "Levitodynamics: Levitation and control of microscopic objects in vacuum," *Science*, vol. 374, no. 6564, p. 3027, 2021. DOI: 10.1126/science.abg3027.

[50] M. Niemetz, W. Schoepe, J. T. Simola, and J. T. Tuoriniemi, "The oscillating magnetic microsphere: A tool for investigating vorticity in superconductors and superfluids," *Phys. B: Condens. Matter*, vol. 280, pp. 559–560, 2000. DOI: http://dx.doi.org/10.1016/S0921-4526(99)01864-5.

[51] T. Wang, S. Lourette, S. R. O'Kelley, *et al.*, "Dynamics of a ferromagnetic particle levitated over a superconductor," *Phys. Rev. Applied*, vol. 11, p. 044 041, 4 Apr. 2019. DOI: 10.1103/PhysRevApplied.11.044041.

[52] C. Timberlake, G. Gasbarri, A. Vinante, A. Setter, and H. Ulbricht, "Acceleration sensing with magnetically levitated oscillators above a superconductor," *Applied Physics Letters*, vol. 115, no. 22, p. 224 101, 2019. DOI: 10.1063/1.5129145.

[53] J. Gieseler, A. Kabcenell, E. Rosenfeld, *et al.*, "Single-spin magnetomechanics with levitated micromagnets," *Phys. Rev. Lett.*, vol. 124, p. 163 604, 16 Apr. 2020. DOI: 10.1103/PhysRevLett.124.163604.

[54] B. R. Slezak, C. W. Lewandowski, J.-F. Hsu, and B. D'Urso, "Cooling the motion of a silica microsphere in a magneto-gravitational trap in ultra-high vacuum," *New Journal of Physics*, vol. 20, no. 6, p. 063 028, Jun. 2018, ISSN: 1367-2630. DOI: 10.1088/1367-2630/aacac1.

[55] C. D. Brown, Y. Wang, M. Namazi, G. I. Harris, M. T. Uysal, and J. G. E. Harris, *Characterization of levitated superfluid helium drops in high vacuum*, 2021. DOI: 10.48550/ARXIV.2109.05618.

[56] B. van Waarde, "The lead zeppelin - a force sensor without a handle," Ph.D. dissertation, Universiteit Leiden, The Netherlands, 2016.

[57] M. G. Latorre, G. Higgins, A. Paradkar, T. Bauch, and W. Wieczorek, *Superconducting microsphere magnetically levitated in an anharmonic potential*, 2022. DOI: 10.48550/ARXIV.2210.13451.

[58] J. Prat-Camps, C. Teo, C. C. Rusconi, W. Wieczorek, and O. Romero-Isart, "Ultrasensitive inertial and force sensors with diamagnetically levitated magnets," *Phys. Rev. Appl.*, vol. 8, p. 034 002, 3 Sep. 2017. DOI: 10.1103/PhysRevApplied.8.034002.

[59] J. M. Goodkind, "The superconducting gravimeter," *Review of Scientific Instruments*, vol. 70, no. 11, pp. 4131–4152, 1999. DOI: 10.1063/1.1150092.

[60] M. V. Moody, H. J. Paik, and E. R. Canavan, "Three-axis superconducting gravity gradiometer for sensitive gravity experiments," *Review of Scientific Instruments*, vol. 73, no. 11, pp. 3957–3974, 2002. DOI: 10.1063/1.1511798.

[61] J. D. Teufel, T. Donner, M. A. Castellanos-Beltran, J. W. Harlow, and K. W. Lehnert, "Nanomechanical motion measured with an imprecision below that at the standard quantum limit," *Nature Nanotechnology 2009 4:12*, vol. 4, pp. 820–823, 12 Nov. 2009, ISSN: 1748-3395. DOI: 10.1038/nnano.2009.343.

[62] E. Gavartin, P. Verlot, and T. J. Kippenberg, "A hybrid on-chip optomechanical transducer for ultrasensitive force measurements," *Nature Nanotechnology 2012 7:8*, vol. 7, pp. 509–514, 8 Jun. 2012, ISSN: 1748-3395. DOI: 10.1038/nnano.2012.97.

[63] J. Moser, J. Güttinger, A. Eichler, *et al.*, "Ultrasensitive force detection with a nanotube mechanical resonator," *Nature Nanotechnology 2013 8:7*, vol. 8, pp. 493–496, 7 Jun. 2013, ISSN: 1748-3395. DOI: 10.1038/nnano.2013.97.

[64] G. Ranjit, M. Cunningham, K. Casey, and A. A. Geraci, "Zeptonewton force sensing with nanospheres in an optical lattice," *Phys. Rev. A*, vol. 93, p. 053 801, 5 May 2016. DOI: 10.1103/PhysRevA.93.053801.

[65] A. Vinante, C. Timberlake, and H. Ulbricht, "Levitated micromagnets in superconducting traps: A new platform for tabletop fundamental physics experiments," *Entropy*, vol. 24, no. 11, 2022, ISSN: 1099-4300. DOI: 10.3390/e24111642.

[66] J. Prat-Camps, C. Teo, C. C. Rusconi, W. Wieczorek, and O. Romero-Isart, "Ultrasensitive inertial and force sensors with diamagnetically levitated magnets," *Physical Review Applied*, vol. 8, no. 3, p. 034 002, Sep. 2017. DOI: 10.1103/PhysRevApplied.8.034002.

[67] B. van Waarde, O. Benningshof, and T. Oosterkamp, "A magnetic persistent current switch at milliKelvin temperatures," *Cryogenics*, vol. 78, pp. 74–77, 2016. DOI: 10.1016/j.cryogenics.2016.06.014.

[68] J. F. Hsu, P. Ji, C. W. Lewandowski, and B. D'Urso, "Cooling the motion of diamond nanocrystals in a magneto-gravitational trap in high vacuum," *Scientific Reports 2016 6:1*, vol. 6, pp. 1–7, 1 Jul. 2016, ISSN: 2045-2322. DOI: 10.1038/srep30125.

[69] J. D. Weinstein and K. G. Libbrecht, "Microscopic magnetic traps for neutral atoms," *Phys. Rev. A*, vol. 52, p. 4004, 5 Nov. 1995, ISSN: 10502947. DOI: 10.1103/PhysRevA.52.4004.

[70] J. Reichel, W. Hänsel, and T. W. Hänsch, "Atomic micromanipulation with magnetic surface traps," *Phys. Rev. Lett.*, vol. 83, p. 3398, 17 Oct. 1999, ISSN: 10797114. DOI: 10.1103/PhysRevLett.83.3398.

[71] J. Hofer, G. Higgins, H. Huebl, *et al.*, *High-q magnetic levitation and control of superconducting microspheres at millikelvin temperatures*, 2022. DOI: 10.48550/ARXIV.2211.06289.

[72] I. C. Rodrigues, D. Bothner, and G. A. Steele, "Coupling microwave photons to a mechanical resonator using quantum interference," *Nat. Commun.*, vol. 10, pp. 1–7, 1 Nov. 2019, ISSN: 2041-1723. DOI: 10.1038/s41467-019-12964-2.

[73] D. Zoepfl, M. L. Juan, C. M. Schneider, and G. Kirchmair, "Single-photon cooling in microwave magnetomechanics," *Phys. Rev. Lett.*, vol. 125, p. 023 601, 2 Jul. 2020, ISSN: 10797114. DOI: 10.1103/PHYSREVLETT.125.023601.

[74] P. Schmidt, M. T. Amawi, S. Pogorzalek, *et al.*, "Sideband-resolved resonator electromechanics based on a nonlinear josephson inductance probed on the single-photon level," *Commun. Phys*, vol. 3, pp. 1–7, 1 Dec. 2020, ISSN: 2399-3650. DOI: 10.1038/s42005-020-00501-3.

[75] T. Luschmann, P. Schmidt, F. Deppe, *et al.*, "Mechanical frequency control in inductively coupled electromechanical systems," *Sci. Rep.*, vol. 12, pp. 1–7, 1 Jan. 2022, ISSN: 2045-2322. DOI: 10.1038/s41598-022-05438-x.

[76] D. Zoepfl, M. L. Juan, N. Diaz-Naufal, *et al.*, "Kerr enhanced backaction cooling in magnetomechanics," *ArXiv*, Feb. 2022. DOI: 10.48550/arxiv.2202.13228.

[77] T. Krisnanda, G. Y. Tham, M. Paternostro, and T. Paterek, "Observable quantum entanglement due to gravity," *npj Quantum Information 2020 6:1*, vol. 6, pp. 1–6, 1 Jan. 2020, ISSN: 2056-6387. DOI: 10.1038/s41534-020-0243-y.

[78] J. S. Pedernales, K. Streltsov, and M. B. Plenio, "Enhancing gravitational interaction between quantum systems by a massive mediator," *Phys. Rev. Lett.*, vol. 128, p. 110 401, 11 Mar. 2022. DOI: 10.1103/PhysRevLett.128.110401.

[79] D. Niepce, J. J. Burnett, M. G. Latorre, and J. Bylander, "Geometric scaling of two-level-system loss in superconducting resonators," *Supercond. Sci. Technol.*, vol. 33, no. 2, p. 025 013, 2020. DOI: 10.1088/1361-6668/ab6179.

[80] M. G. Latorre, A. Paradkar, D. Hambraeus, G. Higgins, and W. Wieczorek, "A chip-based superconducting magnetic trap for levitating superconducting microparticles," *IEEE Transactions on Applied Superconductivity*, vol. 32, no. 4, pp. 1–5, 2022. DOI: 10.1109/TASC.2022.3147730.

[81] H. K. Onnes, "Research notebooks 56, 57," *Kamerlingh Onnes Archive, Boerhaave Museum, Leiden, the Netherlands*, 1911.

[82] W. Meissner and R. Ochsenfeld, "Ein neuer effekt bei eintritt der supraleitfähigkeit," *Naturwissenschaften 1933 21:44*, vol. 21, pp. 787–788, 44 Nov. 1933, ISSN: 1432-1904. DOI: 10.1007/BF01504252.

[83] J. N. Rjabinin and L. W. Shubnikow, "Magnetic properties and critical currents of supra-conducting alloys," *Nature 1935 135:3415*, vol. 135, pp. 581–582, 3415 1935, ISSN: 1476-4687. DOI: 10.1038/135581a0.

[84] C. J. Gorter and H. Casimir, "On supraconductivity i," *Physica*, vol. 1, pp. 306–320, 1-6 Jan. 1934, ISSN: 0031-8914. DOI: 10.1016/S0031-8914(34)90037-9.

[85] P. Drude, "Zur elektronentheorie der metalle," *Annalen der Physik*, vol. 306, no. 3, pp. 566–613, 1900. DOI: https://doi.org/10.1002/andp.19003060312.

[86] P. Drude, "Zur elektronentheorie der metalle; ii. teil. galvanomagnetische und thermomagnetische effecte," *Annalen der Physik*, vol. 308, no. 11, pp. 369–402, 1900. DOI: https://doi.org/10.1002/andp.19003081102.

[87] A. Lindemann, *Proceedings of the Royal Society of London. Series A - Mathematical and Physical Sciences*, vol. 149, pp. 71–88, 866 Mar. 1935, ISSN: 0080-4630. DOI: 10.1098/RSPA.1935.0048.

[88] "On the theory of superconductivity," in *Collected Papers of L.D. Landau*, D. T. Haar, Ed., Pergamon, 1965, pp. 546–568, ISBN: 978-0-08-010586-4. DOI: https://doi.org/10.1016/B978-0-08-010586-4.50078-X.

[89] S. Earnshaw, "On the Nature of the Molecular Forces which Regulate the Constitution of the Luminiferous Ether," *Transactions of the Cambridge Philosophical Society*, vol. 7, p. 97, 1848.

[90] J. Prat-Camps, C. Navau, A. Sanchez, and D.-X. Chen, "Demagnetizing factors for a hollow sphere," *IEEE Magnetics Letters*, vol. 7, pp. 1–4, 2016. DOI: 10.1109/LMAG.2015.2501281.

[91] X. Chen, S. K. Ammu, K. Masania, P. G. Steeneken, and F. Alijani, "Diamagnetic composites for high-q levitating resonators," *Advanced Science*, p. 2 203 619, 2022. DOI: https://doi.org/10.1002/advs.202203619.

[92] B. Josephson, "Possible new effects in superconductive tunnelling," *Physics Letters*, vol. 1, no. 7, pp. 251–253, 1962, ISSN: 0031-9163. DOI: https://doi.org/10.1016/0031-9163(62)91369-0.

[93] D. Drung, "High-tc and low-tc dc squid electronics," *Superconductor Science and Technology*, vol. 16, no. 12, p. 1320, Oct. 2003. DOI: 10.1088/0953-2048/16/12/002.

[94] S. Alvo, P. Lambert, M. Gauthier, and S. Régnier, "A van der Waals force-based adhesion model for micromanipulation.," *Journal of Adhesion Science and Technology*, vol. 24, no. 15-16, pp. 2415–2428, 2010. DOI: 10.1163/0169942410X508334.

[95] F. L. Leite, C. C. Bueno, A. L. Da Róz, E. C. Ziemath, and O. N. Oliveira, "Theoretical models for surface forces and adhesion and their measurement using atomic force microscopy," *International Journal of Molecular Sciences*, vol. 13, no. 10, pp. 12 773–12 856, 2012, ISSN: 1422-0067.

[96] B. Stegemann, H. Backhaus, H. Kloss, and E. Santner, "Spherical afm probes for adhesion force measurements on metal single crystals," in *Modern Research and Educational Topics in Microscopy*, ser. Microscopy Book Series, J. D. A. Méndez-Vilas, Ed., 1st ed., vol. 1, Badajoz, Spain: Formatex, 2007, pp. 820–827, ISBN: 978-84-611-9419-3.

[97] D. Griffiths, *Introduction to Electrodynamics*. Pearson Education, 2014, ISBN: 9780321972101.

[98] A. Kovetz, *The principles of electromagnetic theory*. Cambridge: Cambridge university press, 1990, ISBN: 0521391067.

[99] R. Jackson, *Novel Sensors and Sensing* (Series in Sensors). CRC Press, 2019, ISBN: 9781420033809.

[100] J. C. Simpson, J. E. Lane, C. D. Immer, and R. C. Youngquist, "Simple analytic expressions for the magnetic field of a circular current loop," *NASA Technical Reports Server*, 2001.

[101] A. A. Kordyuk, "Magnetic levitation for hard superconductors," *Journal of Applied Physics*, vol. 83, no. 1, pp. 610–612, 1998. DOI: 10.1063/1.366648.

[102] J. Hofer and M. Aspelmeyer, "Analytic solutions to the maxwell-london equations and levitation force for a superconducting sphere in a quadrupole field," *Physica Scripta*, vol. 94, no. 12, p. 125 508, Sep. 2019. DOI: 10.1088/1402-4896/ab0c44.

[103] A. M. Campbell, "An Introduction to Numerical Methods in Superconductors," *Journal of Superconductivity and Novel Magnetism*, vol. 24, pp. 27–33, 2011. DOI: 10.1007/s10948-010-0895-5.

[104] E. H. Brandt and J. R. Clem, "Superconducting thin rings with finite penetration depth," *Phys. Rev. B*, vol. 69, p. 184 509, 18 2004. DOI: 10.1103/PhysRevB.69.184509.

[105] W. R. Hudson and R. J. Jirberg, "Critical currents as a function of magnetic field, film thickness," 1971.

[106] G. Deutscher and M. L. Rappaport, "Critical currents of superconducting aluminium - germanium and lead - germanium thin film alloys near the metal - insulator transition," *Journal de Physique Lettres*, vol. 40, pp. 219–221, 10 May 1979, ISSN: 0302-072X. DOI: 10.1051/JPHYSLET:019790040010021900.

[107] D. K. Finnemore, T. F. Stromberg, and C. A. Swenson, "Superconducting properties of high-purity niobium," *Phys. Rev.*, vol. 149, pp. 231–243, 1 Sep. 1966. DOI: 10.1103/PhysRev.149.231.

[108] H. Friedman, Z. Porat, I. Halevy, and S. Reich, "Formation of metal microspheres by ultrasonic cavitation," *Journal of Materials Research*, vol. 25, pp. 633–636, 4 Apr. 2010, ISSN: 08842914. DOI: 10.1557/JMR.2010.0083.

[109] W. Jaszczuk, H. J. T. Brake, J. Flokstra, D. Veldhuis, R. Stammis, and H. Rogalla, "Bonding of a niobium wire to a niobium thin film," *Measurement Science and Technology*, vol. 2, p. 1121, 11 Nov. 1991, ISSN: 0957-0233. DOI: 10.1088/0957-0233/2/11/023.

[110] R. Vikas and S. Kasthurirengan, "Recent advances in gifford-mcmahon cryocoolers," *Journal of Physics: Conference Series*, vol. 1473, no. 1, p. 012 052, Feb. 2020. DOI: 10.1088/1742-6596/1473/1/012052.

[111] P. Kittel, "Ultimate temperature of pulse tube cryocoolers," *AIP Conference Proceedings*, vol. 1218, no. 1, pp. 1601–1608, 2010. DOI: 10.1063/1.3422342.

[112] A. B. Berryhill and P. Spoor, "High-frequency pulse tubes can't always be tipped," *AIP Conference Proceedings*, vol. 1434, no. 1, pp. 1593–1599, 2012. DOI: 10.1063/1.4707090.

[113] H. Abe, M. Morikawa, T. Ueda, R. Nomura, Y. Okuda, and S. N. Burmistrov, "Visual observation of the bubble dynamics in normal 4he, superfluid 4he and superfluid 3he–4he mixtures," *Journal of Fluid Mechanics*, vol. 619, pp. 261–275, 2009. DOI: 10.1017/S0022112008004436.

[114] S. Dickerson, J. M. Hogan, D. M. S. Johnson, *et al.*, "A high-performance magnetic shield with large length-to-diameter ratio," *Review of Scientific Instruments*, vol. 83, no. 6, p. 065 108, 2012. DOI: 10.1063/1.4720943.

[115] S. Hirzel, *Zeitschrift für wissenschaftliche Mikroskopie und mikroskopische Technik*. 1884, p. 660.

[116] E. H. Brandt and J. R. Clem, "Superconducting thin rings with finite penetration depth," *Phys. Rev. B*, vol. 69, no. 18, p. 184 509, 2004. DOI: 10.1103/PhysRevB.69.184509.

[117] A. Sommerfeld, "Problems for part ii," in *Electrodynamics*, A. Sommerfeld, Ed., Academic Press, 1952, pp. 327–330, ISBN: 978-0-12-654664-4. DOI: https://doi.org/10.1016/B978-0-12-654664-4.50011-X.

[118] *Application note parametric feedback cooling.*

[119] M. Poggio, C. L. Degen, H. J. Mamin, and D. Rugar, "Feedback cooling of a cantilever's fundamental mode below 5 mk," *Phys. Rev. Lett.*, vol. 99, p. 017 201, 1 Jul. 2007. DOI: 10.1103/PhysRevLett.99.017201.

[120] T. W. Penny, A. Pontin, and P. F. Barker, "Performance and limits of feedback cooling methods for levitated oscillators: A direct comparison," *Phys. Rev. A*, vol. 104, p. 023 502, 2 Aug. 2021. DOI: 10.1103/PhysRevA.104.023502.

[121] G. Grissonnanche, O. Cyr-Choinière, F. Laliberté, *et al.*, "Direct measurement of the upper critical field in cuprate superconductors," *Nature Communications 2014 5:1*, vol. 5, pp. 1–8, 1 Feb. 2014, ISSN: 2041-1723. DOI: 10.1038/ncomms4280.

[122] M. Gutierrez Latorre, A. Paradkar, D. Hambraeus, G. Higgins, and W. Wieczorek, *A chip-based superconducting magnetic trap for levitating superconducting microparticles*, version 2, Jan. 2022. DOI: 10.5281/zenodo.5911190.

[123] O. Romero-Isart, L. Clemente, C. Navau, A. Sanchez, and J. I. Cirac, "Supplemental material: Quantum magnetomechanics with levitating superconducting microspheres."

[124] O. Romero-Isart, M. L. Juan, R. Quidant, and J. I. Cirac, "Toward quantum superposition of living organisms," *New Journal of Physics*, vol. 12, no. 3, p. 033 015, Mar. 2010. DOI: 10.1088/1367-2630/12/3/033015.

[125] T. R. Roberts and S. G. Sydoriak, "Thermomolecular pressure ratios for $He^3$ and $He^4$," *Phys. Rev.*, vol. 102, pp. 304–308, 2 Apr. 1956. DOI: 10.1103/PhysRev.102.304.

[126] L. Martinetz, K. Hornberger, and B. A. Stickler, "Surface-induced decoherence and heating of charged particles," *PRX Quantum*, vol. 3, p. 030 327, 3 Aug. 2022. DOI: 10.1103/PRXQuantum.3.030327.

[127] M. Tinkham, *Introduction to Superconductivity: Second Edition* (Dover Books on Physics). Dover Publications, 2004, ISBN: 9780486435039.

[128] G. Kim, I. Kim, and I. Choi, "Design and fabrication of a heat switch for a squid-based superconducting gravimeter," *Physica C: Superconductivity and its Applications*, vol. 598, p. 1 354 064, 2022, ISSN: 0921-4534. DOI: https://doi.org/10.1016/j.physc.2022.1354064.

[129] Q.-G. Lin, "Theoretical development of the image method for a general magnetic source in the presence of a superconducting sphere or a long superconducting cylinder," *Phys. Rev. B*, vol. 74, no. 2, p. 024 510, 2006. DOI: 10.1103/PhysRevB.74.024510.

[130] C. Cordier, S. Flament, and C. Dubuc, "A 3-D finite element formulation for calculating Meissner currents in superconductors," *IEEE Transactions on Applied Superconductivity*, vol. 9, no. 1, pp. 2–6, 1999. DOI: 10.1109/77.763249.

[131] C. Cordier and S. Flament, "Finite element calculation of meissner currents in multiply connected superconductors," *IEEE Transactions on Applied Superconductivity*, vol. 9, no. 4, pp. 4702–4707, 1999. DOI: 10.1109/77.819341.

[132] F. Grilli, S. Stavrev, Y. Le Floch, *et al.*, "Finite-element method modeling of superconductors: From 2-D to 3-D," *IEEE Transactions on Applied Superconductivity*, vol. 15, no. 1, pp. 17–25, 2005. DOI: 10.1109/TASC.2004.839774.

[133] J. Clarke and A. I. Braginski, *The SQUID Handbook Fundamentals and Technology of SQUIDs and SQUID Systems*. Weinheim: Wiley-VCH, 2006, vol. 1.

[134] T. Schurig, "Making SQUIDs a practical tool for quantum detection and material characterization in the micro- and nanoscale," *Journal of Physics: Conference Series*, vol. 568, no. 3, p. 032 015, 2014. DOI: 10.1088/1742-6596/568/3/032015.

[135] R. Wölbing, J. Nagel, T. Schwarz, *et al.*, "Nb nano superconducting quantum interference devices with high spin sensitivity for operation in magnetic fields up to 0.5 T," *Appl. Phys. Lett.*, vol. 102, no. 19, p. 192 601, 2013. DOI: 10.1063/1.4804673.